FINAL REPORT

SPRAY PROCESSING AND MECHANICAL BEHAVIOR OF γ-TiAl

Grant Number: F49620-94-0137
Period of Performance: 3/1/94 to 2/28/97

Submitted to:
Dr. Charles H. Ward
Air Force Office of Scientific Research
AFOSR/NC
110 DUNCAN AVENUE SUITE B115
BOLLING AFB DC. 20332-0001

Submitted by:
Enrique J. Lavernia, Professor
James C. Earthman, Associate Professor
Department of Chemical, Biochemical
Engineering and Materials Science
University of California, Irvine,
California, 92697-2575
May 20, 1997

19971006 135

REPORT DOCUMENTATION PAGE

Form Approved
OMB No. 0704-0188

1. AGENCY USE ONLY (Leave blank)	2. REPORT DATE May 20 th, 1997	3. REPORT TYPE AND DATES COVERED Final Report 3/1/94 to 2/28/97

4. TITLE AND SUBTITLE

Spray Processing and Mechanical Behavior of γ-TiAl

5. FUNDING NUMBERS

Grant no. F49620-94-0137

6. AUTHOR(S)

Enrique J. Lavernia and James C. Earthman

7. PERFORMING ORGANIZATION NAME(S) AND ADDRESS(ES)

Department of Chemical, Biochemical Engineering and
Materials Science University of California, Irvine, CA, 92697-2575

8. PERFORMING ORGANIZATION REPORT NUMBER

9. SPONSORING / MONITORING AGENCY NAME(S) AND ADDRESS(ES)

AFOSR/NC
110 DUNCAN AVENUE SUITE B115
BOLLING AFB DC. 20332-0001

10. SPONSORING / MONITORING AGENCY REPORT NUMBER

11. SUPPLEMENTARY NOTES

12a. DISTRIBUTION / AVAILABILITY STATEMENT

Approved for public release; distribution unlimited.

12b. DISTRIBUTION CODE

13. ABSTRACT (Maximum 200 words)

The principal developments during the three-year contract period may be described as follows: design and successful implementation of spray forming experiments using γ-TiAl alloys; microstructural characterization and mechanical testing on spray formed γ-TiAl alloys; two dimensional modeling of momentum and thermal behavior during spray atomization of γ-TiAl; investigation of thermal residual stresses in spray formed γ-TiAl using finite element methods; and finite element simulation of creep deformation and rupture of titanium aluminides.

14. SUBJECT TERMS

spray forming; γ-TiAl alloy; mechanical properties

15. NUMBER OF PAGES

105

16. PRICE CODE

17. SECURITY CLASSIFICATION OF REPORT UNCLASSIFIED	18. SECURITY CLASSIFICATION OF THIS PAGE UNCLASSIFIED	19. SECURITY CLASSIFICATION OF ABSTRACT UNCLASSIFIED	20. LIMITATION OF ABSTRACT UL

PREFACE

This final report covers the work accomplished during the period from March 1, 1994 to February 28, 1997 under the Air Force Office of Scientific Research (AFOSR) contract F49620-94-0137. The AFOSR technical monitor for this contract was Dr. Charles H. Ward.

Gamma titanium aluminide alloys are potential structural materials in the aerospace, power generation and automotive industry due to its superior mechanical properties over the conventional superalloys. However, wide spread application of these materials necessitate improvement of their overall mechanical properties and reduction of their cost by optimizing/exploring processing methods. To that effect, spray atomization and deposition of gamma titanium aluminide alloys were investigated in the present study, with the following specific objectives. First, to determine the feasibility of using a spray atomization and deposition approach to synthesize γ–TiAl with improved hot workability. Second, to develop a fundamental understanding of the influence of spray atomization and deposition processing on the microstructural characteristics (e.g., grain morphology, segregation, porosity) of γ–TiAl. Third, to elucidate the influence of these microstructural characteristics on the relevant deformation and fracture mechanisms that govern the behavior of γ–TiAl. In order to achieve the above mentioned objectives, both experimental and numerical methods were employed. Experimental approaches included:

1). spray atomization and deposition of γ-TiAl alloys, the prerequisite to the success of this program;

2). mechanical testing, such as tensile testing, compressive creep testing, and tensile creep testing on spray formed γ-TiAl alloys; and

3). characterization of microstructure and phase compositions of as-received, spray formed, and crept γ-TiAl alloys, using optical microscope, image analysis, density measurement, SEM, TEM, and X-ray diffraction analysis.

These three closely related aspects were aimed to experimentally establish the relationship between processing, microstructure and mechanical properties. Numerical analyses include:

1). Modeling of momentum and thermal behavior during spray atomization of γ-TiAl;

2). Investigation of thermal residual stresses in spray formed γ-TiAl using finite element method; and

3). Study on creep and boundary sliding mechanisms in single phase, dual phase and fully lamellar titanium aluminides using finite element analysis.

The aim of these numerical study efforts was to provide insight into the mechanisms governing spray processing and mechanical behavior; hence to optimize processing parameters, microstructures, and mechanical properties.

SUMMARY

The principal developments during the three-year contract period may be described as follows: design and successful implementation of spray forming experiments using γ-TiAl alloys; microstructural characterization and mechanical testing on spray formed γ-TiAl alloys; two dimensional modeling of momentum and thermal behavior during spray atomization of γ-TiAl; investigation of thermal residual stresses in spray formed γ-TiAl using finite element methods; and finite element simulation of creep deformation and rupture of titanium aluminides. These developments are summarized in the following paragraphs.

Gamma titanium aluminides with three different alloy compositions (Ti-37.4Al-1.5Nb-1.5Cr, Ti-42Al-2Nb-2Cr, Ti-47Al, all in atomic percent) were successfully spray formed. The spray formed γ–TiAl deposits generally exhibited a Gaussian profile. The spray formed Ti-47at.%Al alloys generally exhibited a fine, equiaxed fully lamellar $\alpha_2+\gamma$ structure (an average linear grain size of 60 μm and an average interlamellar spacing about 0.3 μm), in contrast with the coarse grains (typically 250 to 1800 μm) of γ-TiAl with fully lamellar microstructures that are produced from conventional cast or cast + heat treatment processes. This is significant, since it has been reported that a decrease in lamellar grain size increases both strength and ductility of γ-TiAl with fully lamellar microstructures. It is anticipated that a fully lamellar γ-TiAl with a fine grain size will lead to a good combination of ductility, strength, fracture toughness, and creep resistance. Similar to Ti-47Al, the grain refinement through spray forming processing was also significant for Ti-37.4Al-1.5Nb-1.5Cr and Ti-42Al-2Nb-2Cr. For Ti-37.4Al-1.5Nb-1.5Cr, the average linear size of prior β phase grains had been reduced from more than 1000 μm to approximate 146 μm, while that for Ti-42Al-2Nb-2Cr was reduced from 425 μm to 130 μm. Other microstructural details, however, were dramatically different than that in Ti-47Al. In contrast with the fully lamellar $\alpha_2+\gamma$ structure observed in Ti-47Al, no lamellar $\alpha_2+\gamma$ were detected in Ti-37.4Al-1.5Nb-1.5Cr. Rather, Ti-37.4Al-1.5Nb-1.5Cr consists of prior β grain boundaries, with α plates precipitated out of β phase in the grain along several preferred directions, forming Widmanstatten structures. The α plates

ordered into α_2 upon further cooling. The microstructure of Ti-42Al-2Nb-2Cr, on the other hand, is featured by equiaxed fully lamellar $\alpha_2+\gamma$ structure, with the $\alpha_2+\gamma$ lamellae being cross-cut by a series of nearly parallel lines in each grain.

The compressive creep behavior of spray formed γ–TiAl with a fine, equiaxed fully lamellar (FL) microstructure was studied in a temperature-stress regime of 780 to 850 °C and 180 to 320 MPa. An apparent stress exponent of 4.3 and an activation energy of 342 kJ/mol were observed in the high-temperature high-stress regime. Compared with the FL γ–TiAl which was obtained through conventional casting + heat treatment processes, the spray formed γ–TiAl exhibited higher creep resistance. The higher creep resistance observed in the present study was discussed in light of the interstitial level, the chemical composition, the grain size, and the interlocking of lamellae at the grain boundary which in turn may be a function of interlamellar spacing and the step height of the serrated grain boundaries. It was suggested that the small interlamellar spacing and possibly larger step height may contribute to the higher creep resistance observed in the present study.

A two-dimensional model was formulated in the study of the momentum and thermal behavior during spray atomization of γ-TiAl. The modeling results indicated that the velocity, temperature, cooling rate, flight time and solidification behavior of atomized droplets strongly depends on the initial position, r_0, and the diameter of the droplet, D. In addition, the velocity profiles, temperature histories, cooling rates, flight times and solidification behavior of droplets are also closely related to each other. Specifically, for identical r_0, i) fine droplets are more readily accelerated or decelerated relative to coarse droplets along both axial and radial directions, ii) fine droplets cool at a higher cooling rate than coarse ones, and iii) fine droplets also solidify at a faster rate relative to coarse ones. For identical D, i) the maximum value of the axial component of droplet velocity decreases with increasing r_0, while the maximum value of the radial component of droplet velocity initially increases and then decreases with increasing r_0, ii) flight time increases with increasing r_0 and iii) the solid fraction at any given axial distance increases with increasing r_0 resulting from the longer flight time for larger r_0. Moreover, the two dimensional droplet size distribution in the spray cone

was demonstrate to change from being heterogeneous to be almost homogeneous with increasing axial flight distance. When the axial distance is smaller than a critical value (approximately 0.75 m for the conditions used in present study), coarse droplets concentrate in the central region of the spray cone, whereas fine droplets populate the periphery. When the axial distance increases beyond this critical value, the spatial droplet size distribution in the spray cone becomes independent of the radial position. Finally, the two dimensional distribution of the fraction solidified in the spray cone was noted to be heterogeneous. The fraction solidified at any axial distance increases with increasing radial distance from the spray axis.

Thermo-elastoplastic finite element analysis was carried out to investigate the thermal residual stresses that may develop during the spray deposition processing of γ-TiAl. It was noted that thermal residual stresses were developed in the spray formed γ-TiAl during cooling from the deposition temperature to ambient temperature. The axial, hoop, and radial stresses were found to be mostly compressive for the lower center region of the preform. The magnitude of these compressive stresses increases for the region closer to the bottom of the preform. For the other region, the axial, hoop, and radial stresses become tensile. In addition, the residual stress distribution was found to be a strong function of cooling rate in the deposited preform, with the residual stresses decrease as the cooling rate decreases. When the substrate is insulated, the preform has the lowest residual stress distribution for the cases studied herein. Finally, the residual stress distribution was also demonstrated to be a strong function of deposit thickness. For the region closer to the outer edge of the preform, which experiences the most severe thermal gradient, has the highest residual stresses. The von Mises' equivalent stresses in this region were found to be greater than the yield stress of γ-TiAl. Therefore, it is anticipated that plastic deformation or cracks may be present in this region of the preform.

Creep deformation and cavitation damage in dual phase ($\alpha_2 + \gamma$) equiaxed and fully lamellar microstructures were simulated and analyzed in the present research program using finite element techniques. Different models of these microstructures were developed depending on the different deformation mechanisms active in the microstructures such as grain boundary sliding and

phase boundary sliding. Nonlinear viscous primary creep deformation was modeled in each phase based on published creep data. Overall strain rates are compared to gain an understanding of the relative influence each of these localized deformation mechanisms has on the creep strength of the microstructures considered. Facet stress enhancement factors were also determined for the transverse grain facets in each model to examine the relative susceptibility to creep damage. Creep constrained grain boundary cavitation was also analyzed for these microstructures. The cavitation in the models was based on the modified equations of Rice and Needleman. It was found that grain boundary sliding strongly enhances the cavity growth in all of the models analyzed. Comparisons of the results for different lath configurations suggest that lath width has little effect on the constraints that govern cavity growth. A study of effect of cavitating facet density on cavitation damage was completed for the fully lamellar microstructures. Approximate techniques of Hutchinson and Riedel and Eggeler for strain rate enhancement during creep cavitation due to increase in cavitating facet density were compared using the finite element results as the reference. Interaction between cavitating facets in the fully lamellar TiAl were been studied. It was found that when the cavitating facets are not on neighboring grain boundaries, a negative interaction effect takes place in the presence of grain boundary sliding. The present results suggest that the longer creep life observed experimentally for the fully lamellar structure is primarily due to inhibited former grain boundary sliding in this microstructure compared to relatively unimpeded grain boundary sliding in the equiaxed microstructures. The serrated nature of the former grain boundaries generally observed for lamellar TiAl alloys is consistent with this finding.

TABLE OF CONTENTS

LIST OF PUBLICATIONS
resulting from AFOSR Grant no. F49620-94-1-0137

L1. Journal Articles

1. "Finite Element Analysis of Cavitating Facet Interaction in a Fully Lamellar Titanium Aluminide Alloy Under Creep Conditions", A. Chakraborty and J.C. Earthman, *Metall. Trans. A.*, submitted for publication (1997).

2. "Compressive Creep Behavior of Spray Formed Gamma Titanium Aluminide", B. Li, J. Wolfenstine, J.C. Earthman and E.J. Lavernia, *Metall. Trans.*, in press, (1997).

3. "Numerical Models of Creep Cavitation in Single Phase, Dual Phase and Fully Lamellar Titanium Aluminide", A. Chakraborty and J.C. Earthman, *Acta Mater.*, in press (1997).

4. "Numerical Models of Creep and Boundary Sliding Mechanisms in Single Phase, Dual Phase and Fully Lamellar Titanium Aluminides", A. Chakraborty and J.C. Earthman, *Metall. Trans. A*, in press, (1997).

5. "Characterization of Low-Cycle Fatigue Damage in Inconel 718 by Laser Light Scattering", K. J. C. Chou and J. C. Earthman, *J. Mater. Res.*, in press, (1997)

6. "Two Dimensional Modeling of Momentum and Thermal Behavior During Spray Atomization of γ-TiAl", B. Li, X. Liang, J.C. Earthman and E.J. Lavernia, *Acta Mater.*, **44(6)**, 2409 (1996).

7. "Spray Forming of γ–Titanium Aluminide", B. Li, W. Cai and E.J. Lavernia, *J. Mater. Synth. Proc.*, **4(1)**, 35 (1996).

8. "Thermal Residual Stresses in Spray Atomized and Deposited Ni_3Al", S. Ho and E.J. Lavernia, *Scripta Metall. Mater.*, **34(4)**, 527 (1996).

9. "Investigation of Thermal Residual Stress in Spray Atomized and Deposited γ-TiAl using Finite Element Method", S. Ho and E.J. Lavernia, *J. Mater. Synth. Proc.*, **3(6)**, 403 (1995).

10. "Evolution of Interaction Domain Microstructure During Spray Deposition", X. Liang and E.J. Lavernia, *Metall. Trans.*, **25A**, 2341 (1994).

11. "Spray Atomization and Deposition Processing of Metal Matrix Composites: An Overview", E.J. Lavernia and X. Liang, *Reviews in Particulate Materials*, **2**, 3 (1994).

L2. Conference Papers

1. "Spray Processing and Mechanical Behavior of γ-TiAl", B. Li and E.J. Lavernia, in *the Proceedings of International Symposium on Structural Intermetallics-'97*, eds. M. Nathal, D. Miracle and R. Darolia, TMS, Warrendale, PA, 1997.

2. "Numerical Simulations of Cavitation Damage in TiAl Alloys", A. Chakraborty and J.C. Earthman, in *Mechanism of High Temperature Deformation*, eds. J.C. Earthman and F.A. Mohamed, TMS, Warrendale, PA, 1997.

3. "Spray Atomization and Deposition of Gamma Titanium Aluminide Alloys" B. Li and E.J. Lavernia, *J. Mater. Synth. Proc.*, in press, 1997.

4. "Spray Forming of Gamma Titanium Aluminide Alloys", B. Li and E.J. Lavernia, in *Spray Forming 3*, ed. J.V. Wood, Woodhead Publishing Limited, 1996.

5. "Investigation of Thermal Residual Stresses in Layered 2024Al/SiC Composite using Finite Element Method and X-Ray Diffraction", S. Ho and E.J. Lavernia, in *Processing and Fabrication of Advanced Materials V*, eds. T.S. Srivatsan and J.J. Moore, TMS Warrendale, PA, 1996.

6. "Two Dimensional Profile of Momentum and Thermal Behavior of Spray Atomized γ-TiAl Droplets", B. Li, X. Liang, J.C. Earthman and E.J. Lavernia, in *Powder Metallurgy in Aerospace, Defense and Demanding Applications*, ed. F.H. Froes, MPIF, Princeton, NJ, 1995.

7. "Microstructure and Fracture Behavior of a Spray Atomized and Deposited Nickel Aluminide Intermetallic", D. Lawrynowicz, X. Liang, T.S. Srivatsan and E.J. Lavernia, in *Fatigue and Fracture of Ordered Intermetallic Materials II*, eds. W.O. Soboyejo, T.S. Srivatsan and R.O. Ritchie , TMS, Warrendale, PA, USA, 1994.

CHAPTER 1.

BACKGROUND

The ordered γ-TiAl intermetallic is an attractive candidate material for applications that demand thermal stability, as a result of its attractive combinations of density (3.76 g/cm^3), creep/stress rupture and fatigue resistance, and elevated temperature strength [1-10]. Not surprisingly, the available literature reveals that both single phase and two phase γ-TiAl alloys have been studied extensively [11-14]. The physical and mechanical properties of multicomponent γ-TiAl alloys have been demonstrated to depend on chemistry, phase composition and geometry, thermomechanical processing, and the content of interstitial impurities (e.g., nitrogen, carbon, oxygen and boron) [12-17]. Extensive structural utilization of γ-TiAl, however, has been hindered by the poor low temperature ductility and less-than-optimum toughness that are characteristic of this material. In particular, the solute segregation (both macrosegregation and microsegregation) that is generally associated with cast γ-TiAl requires extensive post processing long term heat treatments, thereby leading to low material yields and high costs [2-4, 11, 18-20]. Furthermore, although macrosegregation may be eliminated subsequently by either hot working (e.g., extrusion, forging, hot isostatic pressing), heat treatment (typically in the alpha field for cast γ-TiAl) or both [11], the suppression of microsegregation requires an enhancement of solidification kinetics during processing. To that effect, it is possible to avoid macrosegregation and minimize microsegregation in γ-TiAl by using powder metallurgy techniques. Nonetheless, powder metallurgy technique inherently introduces surface contaminants (as a result of the large surface areas that are associated with fine powders), and leads to higher manufacturing costs. Inspection of the available scientific literature reveals that both intrinsic (e.g., manipulation of grain morphology, alloying additions and novel processing methods) and extrinsic (e.g., ductile phase toughening) approaches are actively being pursued in an effort to improve the properties of γ-TiAl [11, 13, 14, 17]. It is also evident, however, that existing processing methods should be optimized

1

and novel processing methods should be explored, before γ-TiAl can be successfully exploited as a structural material.

In view of the above findings, present research efforts are aimed at using a novel synthesis approach, namely spray atomization and deposition, to eliminate macrosegregation, minimize microsegregation, and achieve grain refinement and compositional homogeneity in γ-TiAl. In spray atomization and deposition, a molten stream of metal is disintegrated into a fine dispersion of droplets using high velocity inert gas jets. The resulting semi-solidified droplets are directed towards a substrate where they impinge and collect as fine grained, chemically homogeneous, thin splats. The first high velocity droplets impact directly against the substrate surface, and then themselves act as a quenching substrate for their successors. Relatively high rates of solidification are imposed during processing as a result of the thinness of the splats, the rapid heat extraction during flight, and an inert atmosphere. Spray atomization and deposition inherently avoids microstructural coarsening and extensive macrosegregation, which are normally associated with casting processes. To that effect it is well documented that spray atomization and deposition has been successfully applied to improve the physical and mechanical characteristics of: Al and Mg alloys [21-23]; Ni, Fe and Ni3Al intermetallics [24-27]; and discontinuous metal matrix composites (MMCs) [28-31]. More recently, encouraging preliminary results were reported on spray atomization and deposition processing of TiAl and Ti$_3$Al [32-35]. J.W. Sears [34], for example, notes that initial spray deposition experiments led to low interstitial levels, low porosity, and fine grained structures. The latter observation, namely, a fine grained structure, should lead to improvements in toughness. In other studies Sears et al. [35] were able to produce a totally dense material using Hot Isostatic Pressing (HIPing) following spray deposition. J.M. Young et al. [33] also report that the pores that were present in the as-sprayed Ti-52Al were removed by HIPing. None of these studies, however, reported any processing details. Moreover, evaluation of the microstructural characteristics/variations and mechanical properties are limited in these studies, not to mention correlation of processing parameter with microstructure/mechanical properties of spray formed γ-TiAl.

CHAPTER 2.

SPRAY FORMING OF γ-TiAl ALLOYS

2.1. Objective

The efforts in this aspect include the design, and the implementation, of spray forming experiments using γ-TiAl alloys; and characterization of the spray formed alloys.

2.2. Experimental

The induction skull melting/spray atomization and deposition facility utilized to spray process gamma TiAl alloys is schematically shown in Figure 2-1. The experimental procedure in spray forming may be described as follows. The skull crucible was charged with as-received γ-TiAl alloys. The cooling system in the skull crucible assured the formation of a γ-TiAl skull on the inside wall of the crucible when the molten Ti-Al alloys contact the cold crucible wall. The formation of
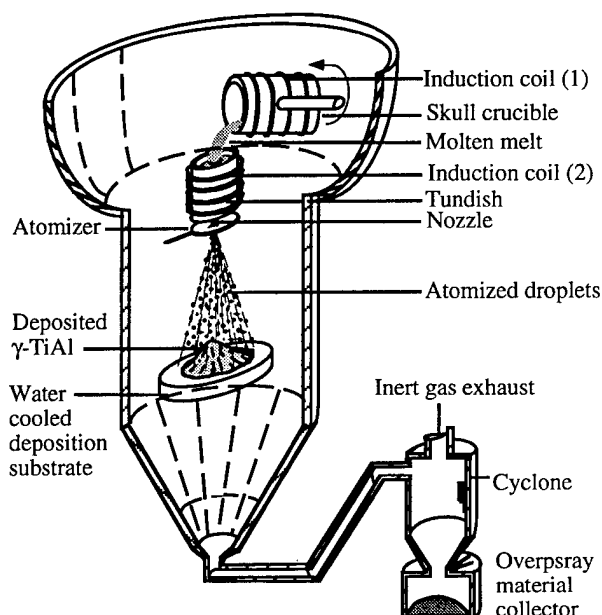
Figure 2-1. Schematic representation of the induction skull melting/spray atomization and deposition facility.

the γ-TiAl skull prevented the reaction between the chemically reactive molten Ti-Al alloys and the crucible. Once the central part of the charge was completely melted, the skull crucible was tilted down, and Ti-Al melt was poured into a synchronously heated tundish. The Ti-Al melt was then delivered through a nozzle to an 18-jets atomizer, where it was atomized by high pressure Argon gas (dynamic atomization pressure ranges from 1 to 2

MPa). The atomized micro-sized droplets were subsequently deposited on a water cooled stationary planar Cu substrate. Powders not incorporated into the deposit, which are generally referred to as oversprayed powders, were carried by the gas flow into the cyclone and collected in the container attached to the cyclone. To prevent extensive oxidation of the materials during processing, all experiments were conducted in an environmental chamber, which was generally evacuated to a pressure of 133 Pa (1 torr) or lower, and back
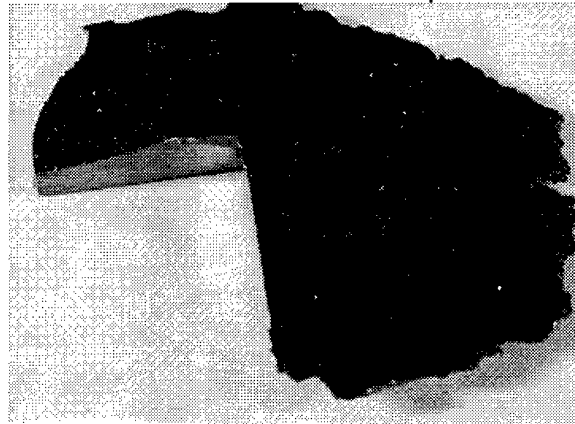
Figure 2-2. Gaussian profile of spray formed Ti-47at.%Al.

filled with argon gas to a pressure of 1×10^5 Pa prior to melting and atomization.

Gamma titanium aluminides with three different alloy compositions were successfully spray formed, as summarized in Table 2-1. The spray formed γ–TiAl deposits generally exhibited a Gaussian profile, as shown in Figure 2-2 for a spray formed Ti-47Al. The thickness of the central region ranges from 10 to 15 mm depending on processing parameters, while the diameter of the bottom ranges from 10 to 15 cm.

Table 2-1. Spray formed γ-TiAl alloys

Nominal composition (at.%)	Supplier
Ti-37.4Al-1.5Nb-1.5Cr	Supplied by Dr. Don Larsen, Howmet Corporation, Operhall Research Center, Whitehall, MI
Ti-42Al-2Nb-2Cr	Supplied by Dr. Shyh-Chin Huang, General Electric Research and Development Center, Schenectady, NY
Ti-47Al	Purchased from The Duriron Company, Inc., Titanium Casting Operations, Dayton, OH

2.3. Microstructures

The spray formed Ti-47at.%Al alloys generally exhibited a fine, equiaxed fully lamellar $\alpha_2+\gamma$ structure. Figure 2-3 shows the microstructure of one of the spray formed Ti-47at.%Al, with an average linear grain size of 60 μm and an

4

average interlamellar spacing about 0.3 μm, in contrast with the coarse grains (typically 250 to 1800 μm [5, 36]) of γ-TiAl with fully lamellar microstructures that are produced from conventional cast or cast + heat treatment processes. This is important, since it has been reported that a decrease in lamellar grain size increases both strength and ductility of γ-TiAl with fully lamellar microstructures [5]. It is anticipated that a fully lamellar γ-TiAl with a fine grain size will lead to a good combination of ductility, strength, fracture toughness, and creep resistance.

Figure 2-3. Optical microstructure of spray formed Ti-47at.%Al.

The spray formed Ti-37.4Al-1.5Nb-1.5Cr exhibits an equiaxed morphology, with an average linear grain size of approximately 146 μm, as shown in Figure 2-4. The acicular α phase precipitates from the elevated temperature β phase, forming a Widmanstätten structure. The grain refinement of Ti-37.4Al-1.5Nb-1.5Cr through spray forming processes is significant, since the grain size of the as-received material is larger than 1000 μm. In comparison, spray formed Ti-42Al-2Nb-2Cr exhibits a fully lamellar α2+γ microstructure, with an average grain size of approximately 130 μm (Figure 2-5), refined from an average grain size of 425 μm for the as-received materials. It is worth noting that, in each grain, there are several nearly parallel lines across the α2+γ lamellae, as marked in Figure 2-5 in one of the grains. Based on the results of heat treatment on as-received and spray formed Ti-37.4Al-1.5Nb-

5

1.5Cr (not Ti-42Al-2Nb-2Cr), it is believed that these lines are the traces of acicular α phase grain boundaries (αPGB), i.e., lamellar $\alpha_2+\gamma$ were precipitated from the prior acicular α grains.
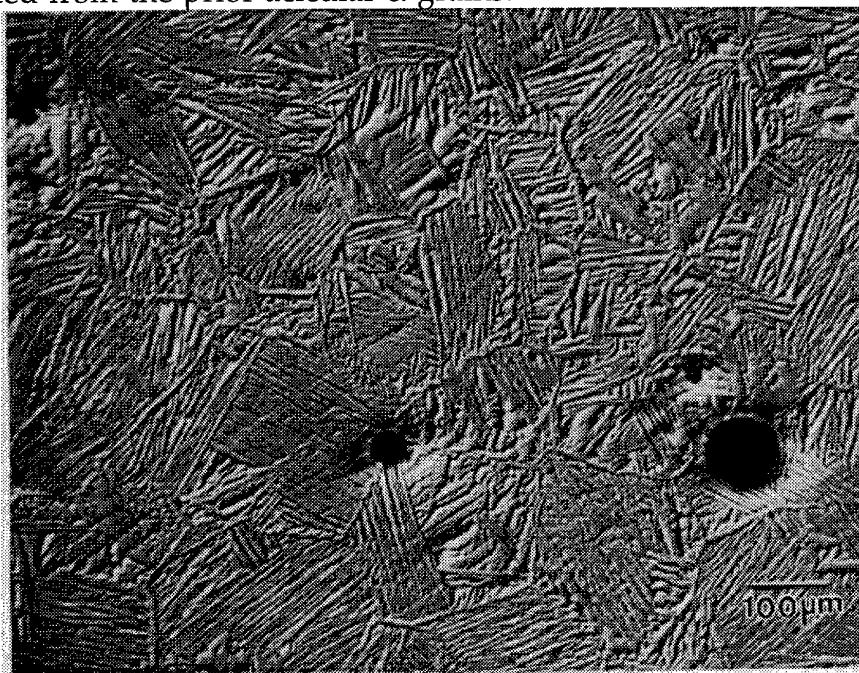
Figure 2-4. Optical microstructure of spray formed Ti-37.4Al-1.5Nb-1.5Cr.
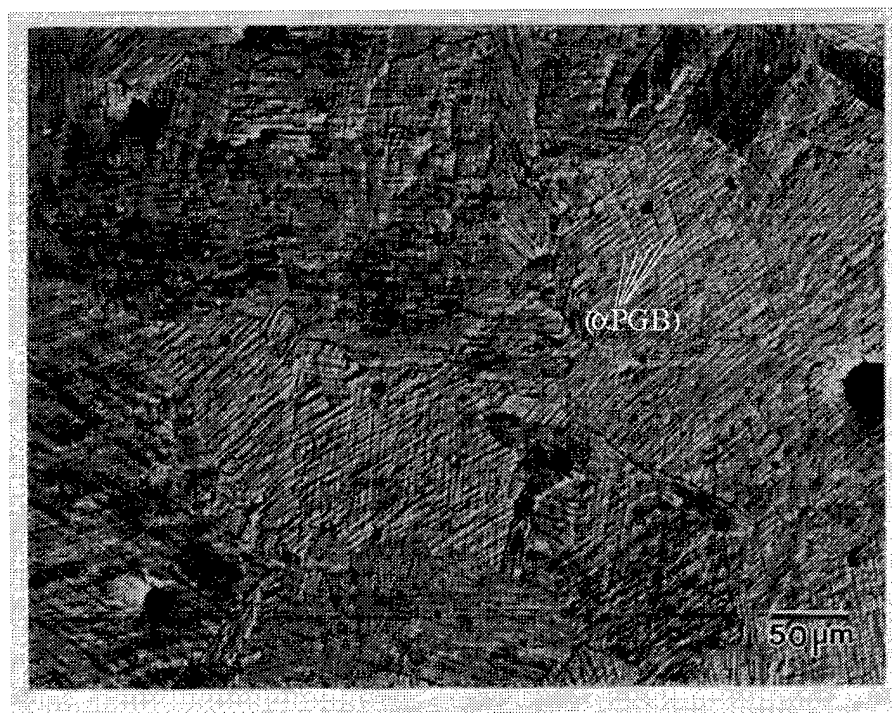
Figure 2-5. Optical microstructure of spray formed Ti-42Al-2Nb-2Cr. αPGB represents prior acicular α phase grain boundaries.

6

2.4. Summary

Gamma titanium aluminides with three different alloy compositions were successfully spray formed. Significant structure refinement through spray atomization and deposition process was observed for all these three alloys.

CHAPTER 3.

COMPRESSIVE CREEP BEHAVIOR OF SPRAY FORMED
GAMMA TITANIUM ALUMINIDE

3.1. Objective

The purpose of this effort is to investigate the compressive creep behavior of spray formed γ-TiAl, and compare it with that of conventionally processed γ-TiAl.

3.2. Experimental

Rectangular parallelepiped compression specimens with a 3 mm gauge length and a 1.5 mm × 1.5 mm cross section were prepared from the spray formed Ti-47Al alloy. Uniaxial compression creep tests were conducted in air over a temperature range of 780-850 °C (0.58-0.62 T_m, where T_m is the absolute melting temperature of γ-TiAl) under true stresses ranging from 180 to 320 MPa. All tests were performed at a single constant true stress and temperature. The microstructure prior and following creep deformation was examined using optical microscopy. The etchant used was Kroll's reagent with the following composition: 1 part HF, 2 parts HNO_3 and 50 parts H_2O.
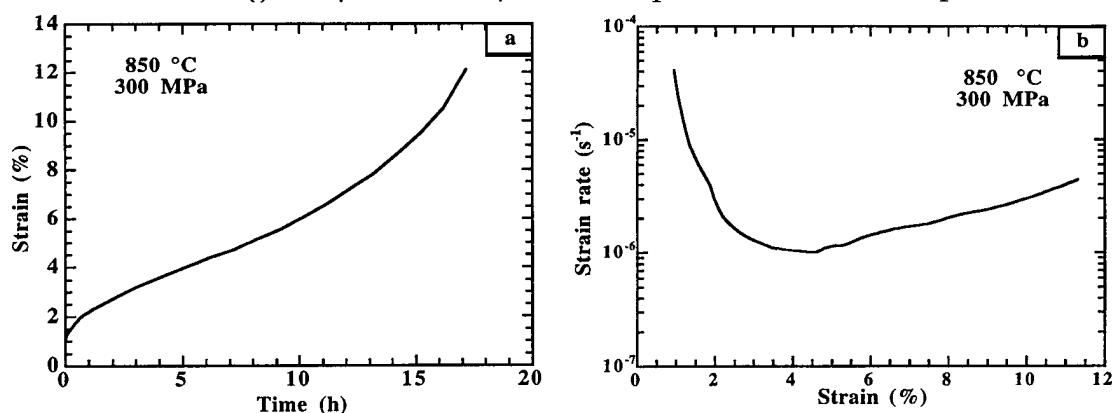
Figure 3-1. Creep curve of spray formed γ-TiAl at 850 °C with a stress of 300 MPa: (a) strain as a function of time, and (b) creep rate as a function of strain.

3.3. Results

Figure 3-1 shows a typical creep curve obtained for spray formed γ–TiAl. The data is for a temperature of 850 °C and a true stress of 300 MPa. A primary

creep stage (where the creep rate decreases with strain) was observed before a minimum creep rate of 1.04×10^{-6} s^{-1} was attained. This was followed by a region in which the creep rate gradually increases with strain. The experimentally observed minimum creep rates of all tests in the present study are summarized in Table 3-1.

Table 3-1. Summary of compressive creep testing of spray formed γ-TiAl

Temperature (°C)	True stress (MPa)	Minimum creep rate (s^{-1})
850	300	1.04×10^{-6}
850	260	5.76×10^{-7}
850	220	3.25×10^{-7}
850	180	8.57×10^{-8}
825	300	3.69×10^{-7}
825	280	3.1×10^{-7}
800	320	1.71×10^{-7}
800	300	1.66×10^{-7}
800	280	8.43×10^{-8}
800	250	5.73×10^{-8}
780	300	8.97×10^{-8}

In general, the creep deformation of a material may be described by a phenomenological equation such as:

$$\dot{\varepsilon}_{min} = A\, \sigma^n \exp(-Q/RT) \qquad (3\text{-}1)$$

where $\dot{\varepsilon}_{min}$ is the minimum strain rate, A is a pre-exponential constant, σ is the applied stress, n is the stress exponent, Q is the activation energy for creep, R is the universal gas constant, and T is the absolute temperature. Figure 3-2 shows the variation of minimum creep rate as a function of stress at temperatures of 800 and 850 °C. The slope of the curves in Figure 3-2 yields the stress exponent, n, according to Eqn. (3-1). From Figure 3-2, the values of the stress exponent, n, were identified to
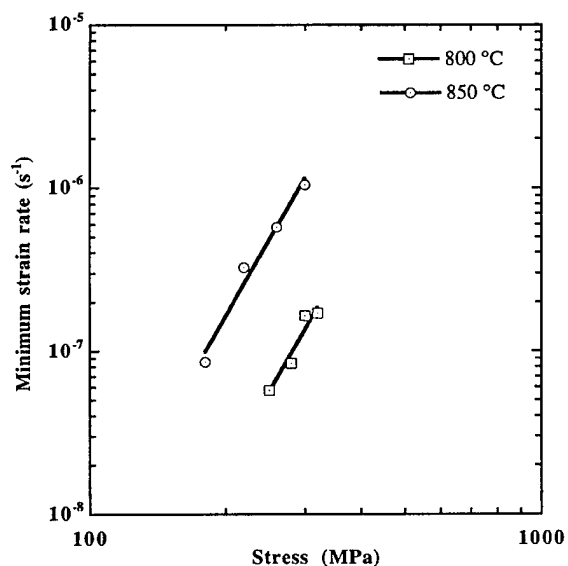
Figure 3-2. Minimum creep rate as a function of stress at 800 °C and 850 °C.

9

be 4.9 and 4.8 for 800 °C and 850 °C, respectively. Figure 3-3 shows the variation of minimum creep rate as a function of temperature with a stress of 300 MPa. An activation energy for creep of 342 kJ/mol was determined from this plot. Figure 3-4 shows the temperature compensated minimum creep rate as a function of stress applied, using an activation energy for creep of 342 kJ/mol, for data shown in Figure 3-2 plus additional data at 780 and 825 °C. All creep data obtained under different temperatures and stresses cluster about a straight line, as predicted from Eqn. (3-1), with a value of the slope equal to 4.3. Curve fitting to the data shown yields the following equation to describe the creep behavior of spray formed γ-TiAl:

$$\dot{\varepsilon}_{min} = 0.21 \, \sigma^{4.3} \exp(-342 kJmol^{-1}/RT) \qquad (3-2)$$
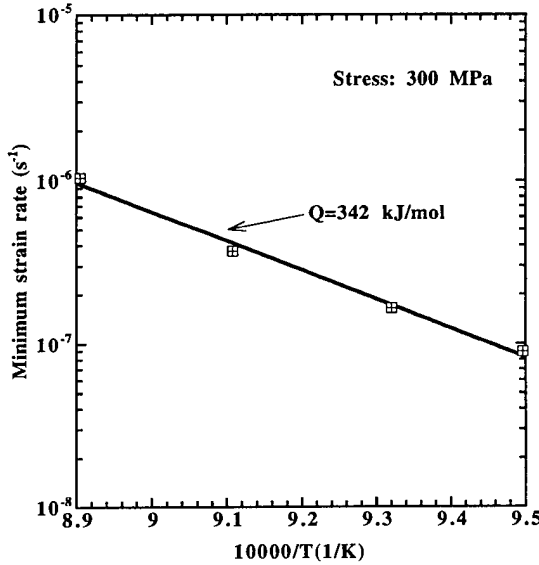
Figure 3-3. Minimum creep rate as a function of temperature at 300 MPa.
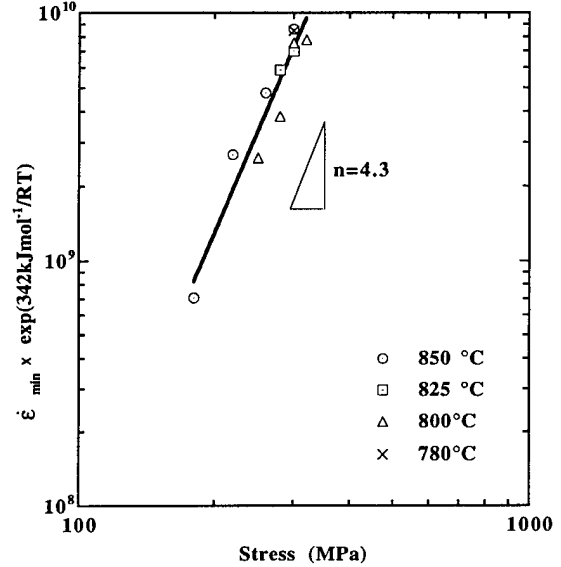
Figure 3-4. Temperature compensated minimum creep rate as a function of stress.

3.4. Discussion

The observed increase in creep rate with strain in Figure 3-1 at strains greater than 4.5% may imply that a microstructural change occurs in the specimen during deformation. To that effect, it has been suggested that a spheroidization of the lamellar microstructure may occur under thermo-mechanical exposure [37-39]. However, as shown in Figure 3-5, optical microstructural observation of the γ-TiAl following creep testing at 850 °C and 300 MPa revealed no obvious spheroidization. Other factors which can lead to the increase in creep rate with strain include: (1) void formation or loss of internal section, (2) environmental degradation (i.e., oxidation), (3)

necking or loss of external section which is normally associated with tensile testing, (4) microstructure degradation (i.e., particle coarsening or grain growth), and (5) inverse creep which is associated with the glide of dislocations [40-42]. Comparison between optical microstructures of as spray formed and crept specimens reveals no obvious grain growth during the creep testing. Moreover, as will be shown below, it appears that the governing mechanism for the creep of spray formed γ-TiAl is dislocation climb. Therefore, for the compressive creep behavior of spray formed γ-TiAl, it is unlikely that the observed increase in creep rate with strain results from either of the last three factors mentioned above. Conclusive determination of
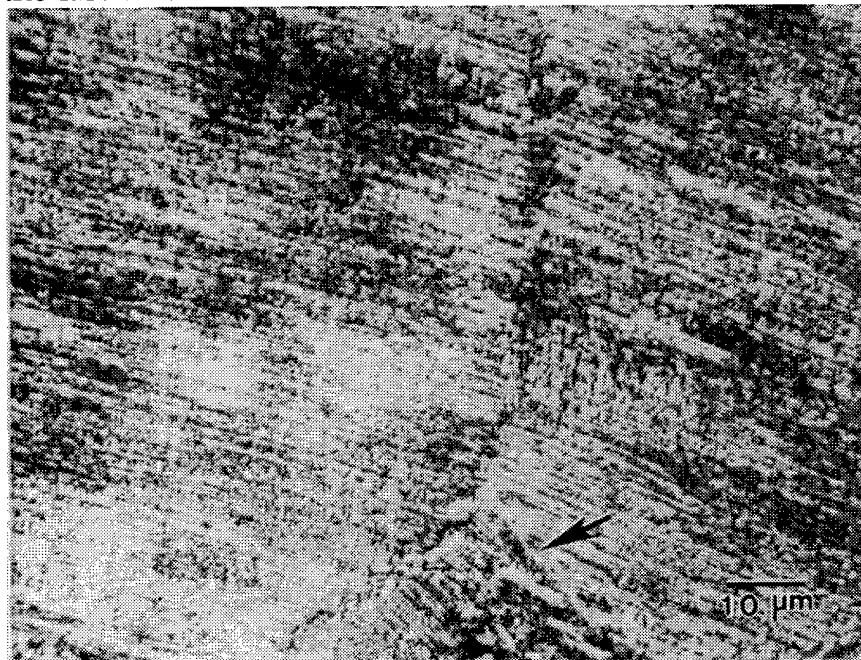
Figure 3-5. Microstructure of γ-TiAl following creep testing, ε=12.11%, at 850 °C with a stress of 300 MPa. The arrow indicates the distorted lamellae.

the effect of environmental degradation requires a comparison of creep behavior in vacuum and in air. However, since little oxidation has been observed on the surface of the crept specimens in the present study, it is likely that the increase of creep rate with strain, after the minimum creep rate has been obtained, results from the formation of voids. The voids in specimen crept at 850 °C with a stress of 300 MPa until ε=12.11% is shown Figure 3-6a. Since there are also voids in as-spray formed materials, as shown in Figure 3-6b, more reliable evidence on formation of voids during creep testing should be the general trend of density decrease for each specimen after creep

11

deformation. This necessitates the measurement of density changes for all of the specimens prior to and after the creep deformation, which has not been carried out in the present study. It is worth noting that in a recent study
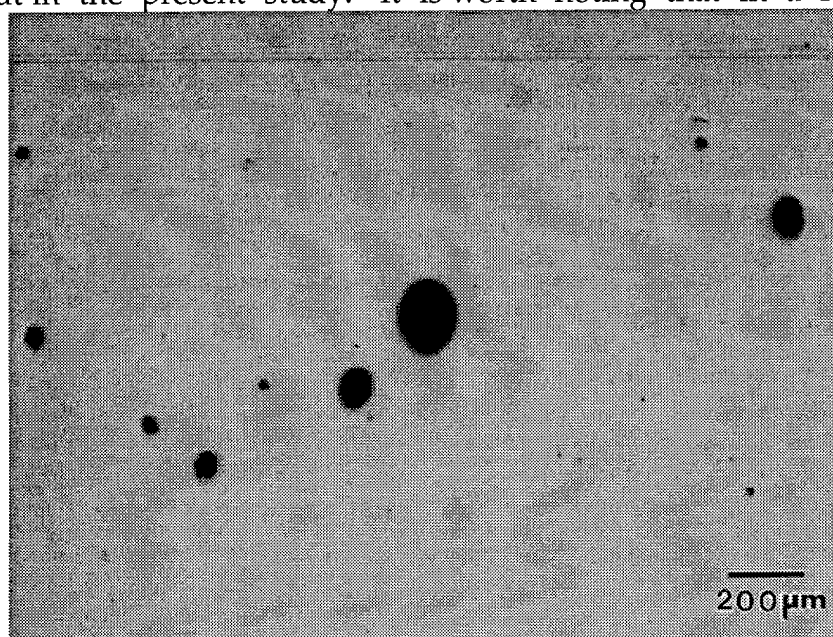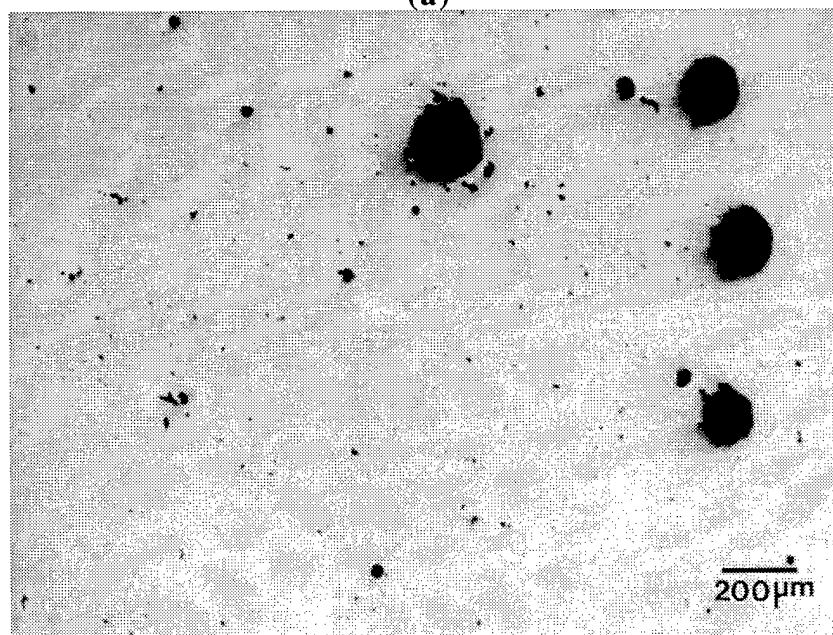
Figure 3-6. Voids observed under optical microscopy on metallographically polished/unetched γ-TiAl specimens: (a) crept, and (b) spray formed.

conducted by Es-Souni et al. [8] on creep behavior of fully lamellar γ-TiAl obtained through conventional cast + heat treatment, TEM observation

12

revealed no dynamic recrystallization of single phase γ regions or spheroidization of α_2 laths, which was detected to be the fundamental reasons for the observed minimum creep rate in a γ-TiAl with lamellar + γ microstructure [43]. Accordingly, early formation of voids and cavities at colony boundaries due to stress concentration, which may result from the strong dependence of yield stress on the orientation of the lamellae with respect to the tensile stress, was suggested to be responsible for the absence of steady state in creep behavior of fully lamellar γ-TiAl [8].

A stress exponent of 4.3 in the present study indicates that the creep behavior of the spray formed γ-TiAl is likely controlled by a dislocation climb process [44-46]. In this case, the activation energy for creep should be equal to the activation energy for lattice diffusion of the slowest species (Ti or Al) in γ-TiAl. Unfortunately, little data is available on self-diffusion of Ti or Al in two phase γ-TiAl. It is worth noting, however, that the activation energy for self-diffusion of Ti in single phase γ-TiAl (Ti-54Al) has been measured to be 291 kJ/mol [47]. This is close to the activation energy for creep, 342 kJ/mol, as observed in the present study.

The creep behavior of γ-TiAl based alloys with different microstructures (fully lamellar, duplex, nearly lamellar, and single phase gamma) has been investigated extensively, and turns out to be complex. Even for fully lamellar γ-TiAl alone, inspection of the available literature indicates that there are some discrepancies in the reported data. While creep curves similar to that shown in Figure 3-1 have been observed by several other researchers [8, 38, 48], a well defined steady state was also reported by Worth et al. [49] and Es-Souni et al. [50] for fully lamellar γ-TiAl. This may result from the differences in alloy composition or microstructural variables, such as grain size and interlamellar spacing, associated with each specimen under investigation. The magnitudes of stress exponent, n, and activation energy, Q, obtained in the present study are in agreement with that reported by Hayes et al. (n=4.6 and Q=335 kJ/mol) [48], Bartholomeusz et al. (n=5.4 and Q=407 kJ/mol) [38], and Worth et al. (n=5.2, Q=348 kJ/mol for high stress level) [49]. As mentioned before, a stress exponent ranging from 4 to 5 and an activation energy for creep close to that for self-diffusion suggest a dislocation climb mechanism in creep deformation. Es-Souni et al. [8, 50] have reported a

13

higher stress exponent (n= 7.6) with microstructural evidence for dislocation climb (i.e. subgrain) for fully transformed lamellar γ-TiAl. No activation energy for creep was determined in their studies. Thus, the present results are in agreement with previous results, including those of Es-Souni et al [8], on that the creep rate of fully lamellar γ-TiAl is controlled by dislocation climb. A stress exponent of 7.6, which was reported by Es-Souni et al [8, 50], may be rationalized in terms of two possible mechanisms: 1) dislocation climb under constant structure [51] or 2) the presence of a threshold stress [10]. The high stress exponent may result from the presence of fine intermetallic dispersoids or oxides/nitrides/carbides in the specimen. The fine particles can pin the subgrain boundaries, stabilizing the subgrain size (constant structure), or if the spacing between particles is smaller than the subgrain size, they can act as effective barriers to dislocation motion, giving rise to a threshold stress. It should be noted that for both creep under constant structure and creep in the presence of a threshold stress, the creep rate can still be controlled by dislocation climb.

It would be of interest to compare the minimum creep rates observed in the present study to those reported by other authors. To that effect, temperature compensated creep rate, using an activation energy for creep averaged on reported values by Bartholomeusz et al. [38], Hayes et al. [48], Worth et al. [49], and the present study, was plotted versus applied stress, as shown in Figure 3-7. A stress exponent of 4.8, averaged based on those authors, was used to curve fit the experimental results. This yields the following equations:

Figure 3-7. Comparison of temperature compensated minimum creep rates as a function of stress.

$$\dot{\varepsilon}_{min} = 0.251 \, \sigma^{4.8} \exp(-358 kJmol^{-1}/RT) \quad (3\text{-}3) \quad \text{for Worth et al. [49]}$$

$$\dot{\varepsilon}_{min} = 0.2 \, \sigma^{4.8} \exp(-358 kJmol^{-1}/RT) \quad (3\text{-}4) \quad \text{for Hayes et al. [48]}$$

14

$$\dot{\varepsilon}_{min} = 0.2 \, \sigma^{4.8} \exp(-358kJmol^{-1}/RT) \qquad (3\text{-}5) \quad \text{for Bartholomeusz}$$
$$\text{et al. [38]}$$

and $\quad \dot{\varepsilon}_{min} = 0.058 \, \sigma^{4.8} \exp(-358kJmol^{-1}/RT) \quad (3\text{-}6) \quad$ the present study

Evidently from Figure 3-7 and the above equations, the minimum creep rate observed in the present study is lower than those reported by other authors for a stress-temperature range where dislocation climb is the dominant mechanism. For FL microstructures, the variables which may influence the creep resistance include: interstitial level, chemical composition, grain size and interlamellar spacing [5, 37]. These variables for the materials used by the different authors are provided in Table 3-2, with their possible effect discussed individually below.

Table 3-2. Linear intercept grain size, interlamellar spacing, and interstitial level for different FL γ-TiAl

Materials	Grain size (μm)	Interlamellar spacing (μm)	C (at. %)	N (at. %)	O (at. %)	Source
Ti-48Al-2Nb-2Mn	150~200	--	0.035	0.018	0.182--	[48]
Ti-49Al-1V	850	0.54	0.07	0.01	0.12	[49]
Ti-44Al	70	5.1	--	--	--	[38]
Ti-47Al	60	0.3	0.25	0.08	0.35	Present study

(A). Interstitial level

It is evident from Table 3-2 that the interstitial levels of carbon and oxygen in the material used in the present study are higher relative to those investigated by other authors. This may lead to the incorrect conclusion that the higher creep resistance observed in the present study resulted from the higher interstitial content in the material investigated. When the creep deformation is controlled by dislocation glide, the above conclusion may sustain, since the movement of dislocation along the slip plane may be dragged by the solute atmosphere, leading to decreased creep rate (i.e., higher creep resistance) [52]. However, as discussed earlier, the creep behavior as reported by Worth et al. [49], Hayes et al. [48], Bartholomeusz et al. [38], and the

15

present study was controlled by dislocation climb, not dislocation glide. In this case, two solute strengthening mechanisms are possible: i). interaction of solute with stacking faults, and ii). pinning of the subgrain boundary by the precipitate/dispersoid.

The interaction of solute with stacking faults may decrease the dislocation mobility by increasing the stress for recombination of partial dislocation (hence decreasing the ability to activate cross slip or climb) [52]. Nevertheless, it was found that the creep deformation structure of the fully lamellar, at a temperature-stress regime similar to the one investigated here, was dominated by the presence of 1/2<110] dislocations [8, 52], of which partial formation is inhibited since it involves very high stacking fault energy [53]. When partial formation is inhibited, solute interaction with stacking faults and the corresponding strengthening effect vanish [54]. Therefore, it is unlikely that the interstitial will increase the creep resistance through solute/stacking-fault interaction.

When the subgrain boundary is pinned by the precipitate/dispersoid, the dislocation mobility may be reduced because of a change from climb to shear for dislocations to bypass the particles. This strengthening mechanism, however, introduces a threshold stress and gives rise to an experimentally determined stress exponent of 8 or higher [10, 52, 55, 56]. Indeed, in a study conducted by Worth et al. [52] regarding the influence of carbon on creep deformation of γ-TiAl alloys, it was found that the creep resistance of fully lamellar γ-TiAl was increased by a factor of 8 through increasing the carbon content from 0.07 to 0.3 at.%. Meanwhile, the stress exponent in their study [52] also increased from 5.2 for low carbon alloy to 8.4 for high carbon, suggesting that the precipitation of carbide in the matrix strengthened TiAl through a threshold stress mechanism. In the present study, the dominant mechanism for creep is dislocation climb, with the stress exponent in the range from 4 to 5. This excludes the influence of impurities on the higher creep resistance observed in the present study through precipitate/dispersoid strengthening mechanism.

Therefore, it is proposed that the higher creep resistance observed in the present study is not due to the relatively higher interstitial level associated with the spray formed γ-TiAl.

(B). Chemical composition

The effect of chemical composition on creep originates from its possible effect on the diffusivity. For a NiAl intermetallic compound, it was found that when the chemical composition deviates from the stoichiometric point, the diffusivity of Ni in NiAl increases [57]. This phenomenon was employed to rationalize the observed increase of creep resistance with decreasing Al content in single phase γ–TiAl [58, 59]. In the study of single phase γ–TiAl [58, 59], the Al content is above 50% for all materials. Decreasing Al content corresponds to less deviation from the stoichiometric composition; hence slower self-diffusion and higher creep resistance. In the present study, the deviation from the stoichiometric composition increases from Ti-49Al-1V, Ti-48-2Nb-2Mn, Ti-47Al, to Ti-44Al. Accordingly, it is anticipated that the self-diffusion of Ti or Al in these materials should increase from Ti-49Al-1V, Ti-48-2Nb-2Mn, Ti-47Al, to Ti-44Al. Because dislocation climb is essentially controlled by the lattice diffusion, the minimum creep rate is expected to increase from Ti-49Al-1V, Ti-48-2Nb-2Mn, Ti-47Al, to Ti-44Al. This is completely different from the trend evident in Table 3-2, suggesting that there are other mechanisms affecting the creep resistance.
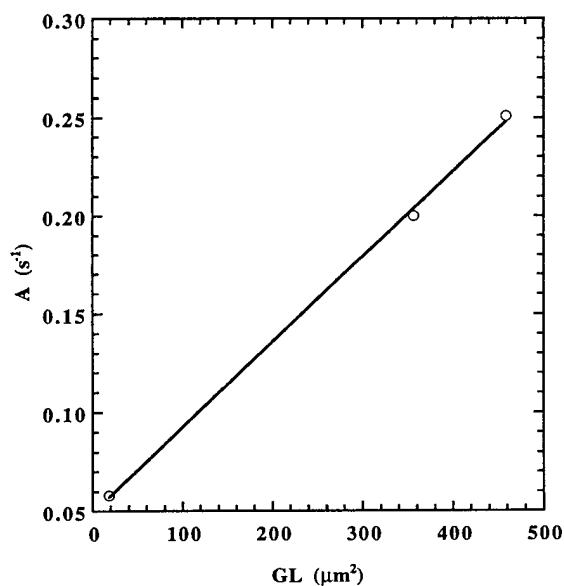
Figure 3-8. Relationship between minimum creep rate, interlamellar spacing (L), and grain size (G).

(C). Grain size

From Figure 3-7, Equations 3-6, and Table 3-2, it appears that the higher creep resistance observed in the present study may be associated with a decrease in grain size. Figure 3-8 plots the pre-exponential constants in Equations (3), (5) and (6), which represent the relative magnitude of creep rate for different materials investigated under the

same temperature and stress, as a function of the product of grain size and interlamellar spacing, GL. The results in Figure 3-8 indicate that the change of creep resistance may be well correlated with the change of GL: when GL increases, the minimum creep rate increases. However, the validity of this type of dependence requires a satisfactory elucidation of its fundamental mechanisms. This is somehow difficult if one notices that the creep deformation is controlled by a dislocation climb mechanism. When the creep deformation is controlled by a dislocation climb mechanism, it is generally considered that

Figure 3-9. TEM micrograph showing the interlocking in spray formed γ-TiAl.

creep behavior is relatively insensitive to the change of grain size [37, 44, 46].

(D). Interlamellar spacing

The interlamellar spacing in fully lamellar microstructure was widely considered to have major effect on the creep behavior of γ-TiAl. However, its exact origin remains to be explored, especially when the creep deformation is controlled by dislocation climb. It was suggested that the increased creep resistance for a lamellar microstructure originates from the reinforcing effect of α_2 laths [12, 52]. Nevertheless, when the deformation is controlled by dislocation climb, it is very difficult to imagine how the α_2 laths act as reinforcement. More studies are necessary to elucidate its fundamental mechanisms. Perhaps it is similar to the precipitate/dispersoid strengthening. In this case, a stress exponent of 8 or higher should be observed, which is not true in the present study.

The effect of interlamellar spacing on the creep behavior may be associated with the interlocking of lamellae in neighboring grains at the grain boundary. The interlocking of lamellae for γ-TiAl with fully lamellar microstructure was reported previously in the literature by several authors [38, 48, 60]. It is

18

also observed in the material used in the present study, as shown in Figure 3-9. Presence of the interlocking may make the grain boundary slide more difficult relative to the case where interlocking is absent, as observed in conventional materials. It has been observed by Bartholomeusz et al. [38], Hayes et al. [48], as well as being evident from Figure 3-5, that the lamellae at the grain boundary region are distorted after creep. This suggests that the interlocking of lamellae in neighboring grains at the grain boundary inhibited the movement of grains relative to each other.

With free grain boundary slide, the material may be divided into soft and hard bands parallel to the direction of applied stress (see Figure 3-10). The effective stress applied on the hard region increases by a factor of ζ ($1<\zeta<2$ [61, 62]), i.e., $\sigma_e=\zeta\sigma$, where σ_e and σ are the effective and applied stresses, respectively. Without grain boundary slide, the polycrystalline material in Figure 3-10 is a rigid body, and the effective stress, σ_e, equals to the applied stress, σ. If the applied stress, σ, in Eqn. (3-1), is substituted by the effective stress σ_e, it is evident that under the same applied stress, the observed creep rate would be higher for the case with grain boundary slide relative to that without grain boundary slide. This concept was illustrated rigorously in reference [61] (also see Chapter 6), where creep deformation of γ-TiAl alloys at two extreme cases, i.e., with and without grain boundary slide, were investigated. A natural extension of this concept is to incorporate the situations between these two extreme cases: the effect of smoothness/roughness of the grain boundary on the effective stress on the hard bands and, in turn, on the creep resistance of the material. It is not difficult to envision that the effective stress on the hard band would be less for materials with rough grain boundaries than that with smooth grain boundaries; and the creep resistance of the former would be higher relative to that of the latter. The smoothness/roughness of the grain boundary may be a function of several parameters describing the interlocking of the lamellae of neighboring grains. First, it is a function of the interlocking nodes. Assuming the interlamellar spacing to be L, and the segment of each hexagon in Figure 3-10 to be S, total number of nodes of interlocking lamellae in each interlocking boundaries may be readily calculated to be $(\sqrt{3}/2)(S/L)$. Secondly, it is intuitively more reasonable to describe the smoothness/roughness of the grain boundary by the node density, rather than the absolute number. The

node density is given by the total number of nodes per unit length of the grain boundary, which equals to $\sqrt{3}/2L$. Finally, the roughness is also a function of the step height, H: the larger the step height, the more rough the grain boundary is. Therefore, the roughness of the grain boundary is proportional to the step height and inversely proportional to the interlamellar spacing. Accordingly, when the step height remains to be the same, the creep resistance will increase with decreasing interlamellar spacing.
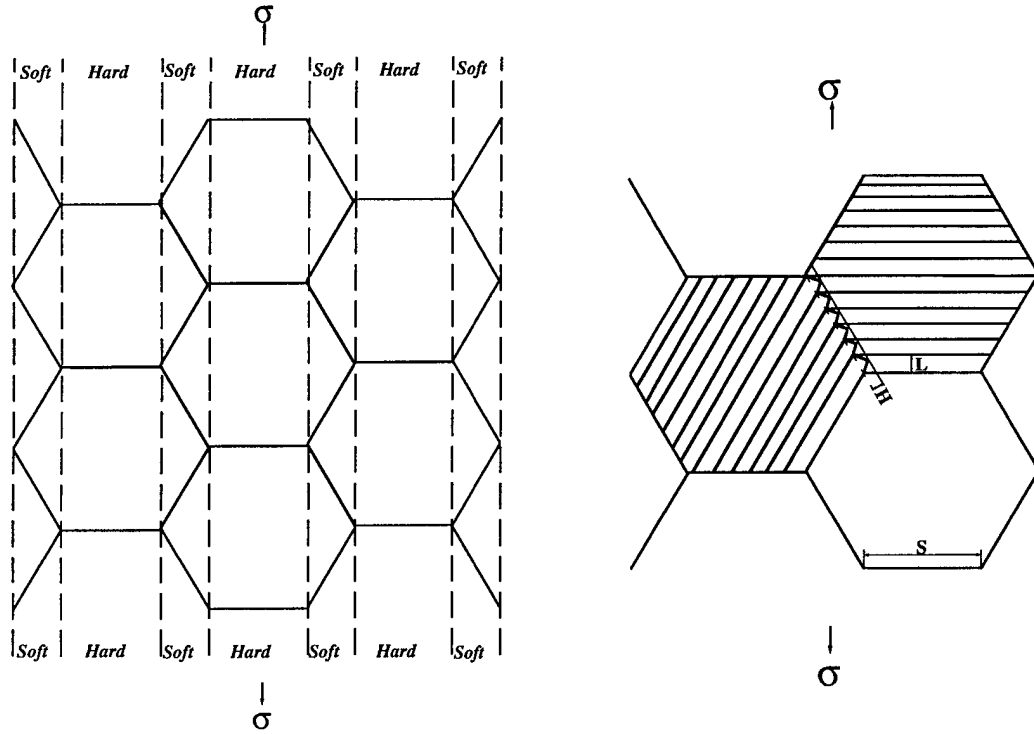
Figure 3-10. Schematic representation showing: (a) the hard/soft band in deformation of polycrystalline materials, and (b) the interlocking lamellae between neighboring grain boundaries. S, H, and L are the length of the hexagon segment, the step height, and the interlamellar spacing, respectively. s is the applied stress.

This is consistent with the higher creep resistance observed in the present study: smallest interlamellar spacing corresponds to lowest minimum creep rate. However, the minimum creep rate may not be satisfactorily described by the interlamellar spacing effect alone as evident from Figure 3-11, which shows the minimum creep rate as a function of interlamellar spacing. This suggests that the step heights for the three different materials in Figure 3-11 are different. Its effect has to be taken into account. It is worth noting that the

chemical composition also affects the creep resistance, as discussed earlier. Nonetheless, incorporation of the chemical composition effect into the interlamellar spacing effect does not help to explain the discrepancy between the observed results and the prediction. For example,

Figure 3-11. Relationship between minimum creep rate and the interlamellar spacing (L).

the creep resistance observed for Ti-49Al-1V was lower than that for Ti-44Al. According to the interlamellar spacing effect, the creep resistance for Ti-49Al-1V should be higher than that for Ti-44Al. The chemical composition effect also suggests that the creep resistance for Ti-49Al-1V should be higher than that for Ti-44Al. Combination of these two effect aggravates the discrepancy between the prediction and the experimental observations.

Figure 3-12. Schematic diagram showing the formation of a serrated grain boundary.

The analysis above indicates that the step height is another very important parameter affecting the creep resistance for fully lamellar spacing. Unfortunately, this parameter is barely studied in the literature for fully lamellar γ–TiAl alloys, and not available for either of the four materials in Table 3-2. Accordingly, it is impossible to evaluate its effect here quantitatively. In general, the step height may depend on the specific processing route used in the preparation of the materials through complex relationship. It is evident that detailed studies on this aspect are necessary to more clearly elucidate the experimental data in terms of the step height and the interlamellar spacing. However, it is worth noting that the step height in spray formed materials may have more chance to be larger than that in conventionally processed materials, as discussed below.

Qualitative analysis of the processing effect on step height necessitates knowledge on the fundamental mechanisms for the formation of interlocking at the neighboring grain boundaries. No existing theory is available in the literature regarding the formation of interlocking for fully lamellar γ-TiAl. However, studies on the solidification path and phase transformation of γ-TiAl indicated that a lamellar structure is formed via either of the following reactions, depending on the composition and cooling rate [12, 13, 18]:

$$\alpha \rightarrow L(\alpha / \gamma) \rightarrow L(\alpha_2 / \gamma) \qquad \text{(low composition, high cooling rate)}$$

or

$$\alpha \rightarrow \alpha_2 \rightarrow L(\alpha_2 / \gamma) \qquad \text{(high composition, low cooling rate)}$$
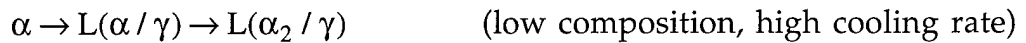
where L stands for lamellar. Similar to normal single phase grain boundaries, the grain boundaries of prior α (Ti solid solution, bcc) grains or prior α_2 (Ti$_3$Al, hcp) grains should be smooth. Accordingly, the lamellae interlocking could only evolve during precipitation of α_2/γ lamellae plates. It is reasonable to believe that the evolution of the lamellae interlocking involves encroach of the earlier precipitating α_2/γ lamellae plates (in grain 1) into later precipitating lamellae plates in neighboring grains (grain 2), as schematically shown in Figure 3-12. The extent of encroachment, or the step height, is therefore determined by the time difference between the initiations of precipitation of these two lamellae plates. The time difference may originate from the variance of local temperature in distinct grains. Compared with the conventional processes, variation of local temperature in distinct grains in spray forming is more likely to occur, since in spray forming the temperature of different impinging droplets are extremely different from each other. In this case, serrated steps may have a better chance to evolve, giving rise to larger step height.

3.5. Conclusions

The creep behavior of spray formed γ–TiAl with a fine equiaxed fully lamellar microstructure was studied in a temperature-stress regime of 780 °C to 850 °C and 180 MPa to 320 MPa. An apparent stress exponent of 4.3 and an activation energy of 342 kJ/mol were observed in the high-temperature high-stress regime. Compared with the FL γ–TiAl which was obtained through conventional casting + heat treatment processes, the spray formed γ–TiAl

exhibited higher creep resistance. The higher creep resistance observed in the present study was discussed in light of the interstitial level, the chemical composition, the grain size, and the interlocking of lamellae at the grain boundary which in turn may be a function of interlamellar spacing and the step height of the serrated grain boundaries. It was proposed that the small interlamellar spacing and possibly larger step height may contribute to the higher creep resistance observed in the present study.

CHAPTER 4.

INVESTIGATION OF THERMAL RESIDUAL STRESSES IN
SPRAY FORMED γ-TiAl USING FINITE ELEMENT METHOD

4.1. Objective

The purpose of this study is to investigate the thermal residual stresses that develop during the spray deposition processing of γ-TiAl using thermo-elastoplastic finite element analysis, and analyze the effect of different cooling conditions on the distribution of thermal residual stresses.

4.2. Finite Element Modeling

With the increasing availability of supercomputers, the finite element method is becoming an increasingly popular approach for gathering of information which can not be extracted from experiments alone, in a systematic manner. In particular, the finite element method has generated considerable interest for modeling the overall thermo-elastoplastic behavior of materials and has been successfully used to estimate residual stresses in various materials [63-69]. The theoretical basis for the thermo-elastoplastic finite element method is available in refs. [70, 71] in detail.

Since the stress and temperature distributions in the deposited preform during spray atomization and deposition process are interdependent, the posed thermo-mechanical problem is fully coupled. Therefore, the thermal and mechanical solutions must be performed simultaneously. In the present study, ABAQUS, a commercially available finite element code developed by Hibbitt, Karlsson, and Sorenson, Inc., Pawtucket, Rhode Island, was employed due to its capability to handle a coupled temperature-displacement problem. Elements provided in ABAQUS for this purpose have nodal variables including both displacement and temperature. These elements generally involve a low-order interpolation for temperature than for displacement (usually parabolic variation of displacement and linear variation of temperature) in order to obtain a compatible variation of thermal and mechanical strains. The minimum potential energy approach to the finite

element formulation of displacement problems gives the following general matrix equation:

$$\mathbf{F_l} = \mathbf{K_s}\mathbf{d} \qquad (4\text{-}1)$$

where $\mathbf{F_l}$ is the global load vector, $\mathbf{K_s}$ is the global stiffness matrix, and $\mathbf{d}$ is the global displacement vector. The application of Galerkin's method to the thermal problems produces the following matrix equation:

$$\mathbf{K_c}\mathbf{T} + \mathbf{C}\dot{\mathbf{T}} + \mathbf{F_h} = 0 \qquad (4\text{-}2)$$

where $\mathbf{T}$ is the temperature vector, $\mathbf{K_c}$ is the conductivity matrix, $\mathbf{C}$ is the heat capacity matrix, $\mathbf{F_h}$ is the heat flow vector. The heat capacity, conductivity, and stiffness matrices in equations (4-1) and (4-2) are generated using a full Gaussian integration scheme, and the coupled system is solved using Newton's method [72]. The detailed description of solution procedures for a coupled temperature-displacement analysis is available in reference [73].

4.2.1. Materials

In the present study, gamma titanium aluminide alloy (γ-TiAl) based on Ti-47 at.% Al was selected as a model material. The phase diagram of titanium-aluminum is shown in Figure 4-1 [74]. Gamma TiAl has special interest in aerospace and automotive industries due to its low density, high melting temperature, elevated temperature strength, high resistance to oxidation and hydrogen absorption, and excellent creep properties [12, 13, 16, 75, 76]. However, γ-TiAl suffers from low ductility and toughness at ambient temperatures which, along with poor formability, appears to be the

Figure 4-1. Phase diagram of titanium-aluminum [74].

single most serious obstacle to its fabrication and full utilization [77]. In order to improve the ambient temperature ductility of γ-TiAl, powder metallurgy or rapid solidification processes followed by powder consolidation, an approach which promotes a grain refinement, is typically employed. Considering the fact that the multiple steps of powder production, sieving, de-gassing, and consolidation may be consolidated into a single processing step, spray atomization and deposition process stands out as a potentially
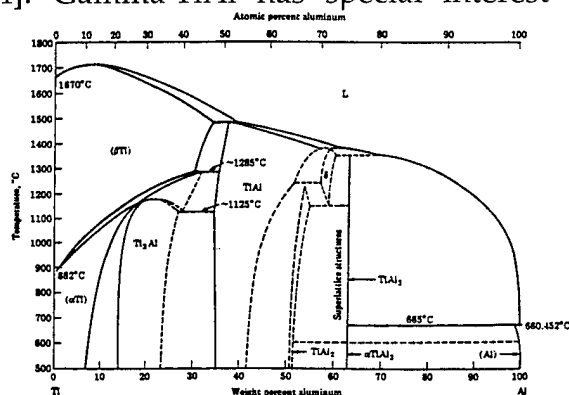
25

economical alternative to produce ductility-improved γ-TiAl. The physical and mechanical properties of γ-TiAl at various temperatures used in the present study are listed in Table 4-1 [75, 78-81].

4.2.2. Geometry

In the present investigation, due to the difficulty in modeling the transient problem posed by a growing preform during spray atomization and deposition, the fully grown preform at the end of deposition was modeled. Accordingly, the present model formulation (*i.e.*, initial conditions) begins immediately following the completion of the deposition stage. The geometrical shape of the final preform considered in this study was assumed to exhibit a contour akin to the Gaussian distribution of droplets impacting on the substrate as shown in Figure 4-2. The height and the bottom diameter of the deposited preform were assumed to be 27 and 100 mm, respectively, consistent with available experimental results [82, 83].

Table 4-1. The physical and mechanical properties
of γ-TiAl at various temperatures [75, 78-81]

Temperature (K)	Elastic Modulus (GPa)	Yield Stress (MPa)	Specific Heat (J/kg·K)	Thermal Expansion (μm/m)	Thermal Conductivity (W/m·K)
300	170	410	658	12.87	89.86
473	168	400	738	13.77	89.86
673	160	390	780	14.40	89.86
873	154	350	808	15.00	89.86
1073	147	300	807	15.60	37.57
1273	138	150	805	16.20	37.57
1473	129	75	800	16.80	37.57
1753	115	38	800	17.50	37.57

Density (kg/m^3) : 3852.5

As shown in Figure 4-2, the deposited preform exhibits an axisymmetric shape. Therefore, the three-dimensional preform could be modeled using two-dimensional axisymmetric elements. Initially, a coarse mesh using relatively small number of elements was employed for modeling, and the number of elements was gradually increased to obtain convergent solutions. A total of 486 four-noded temperature-displacement elements was used in

this study [72]. Figure 4-3 shows the two-dimensional axisymmetric element mesh used herein for modeling the preform.
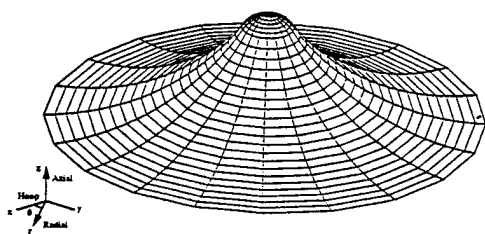
Figure 4-2. The geometrical shape of deposited preform from spray atomization and deposition.
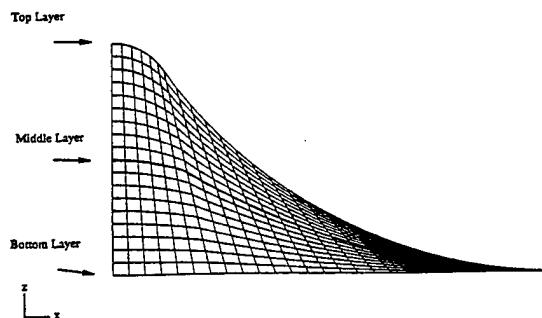
Figure 4-3. Two-dimensional axisymmetric element mesh for modeling of preform.

4.2.3. Boundary and initial conditions

Throughout the modeling, symmetric boundary conditions were imposed such that every symmetric line is constrained in its normal direction to represent the effect of the rest of the material. For the initial temperature condition of the modeling, the temperatures at the top and bottom surfaces of the preform were assumed to be 1753 and 1250 K, respectively, since the top surface of the preform was covered with partially solidified droplets with a solidus temperature of 1753 K at the end of the deposition process, and the bottom surface of the preform was cooled down during the process and assumed to have a temperature of 1250 K, when the deposition process was completed. The temperature inside the preform was then linearly interpolated.

During the spray atomization and deposition process, the deposited preform loses thermal energy through a combination of three heat transfer processes: a) conduction to the low temperature substrate, b) convection to the atomization gas, c) radiation to the environment [83]. On the basis of thermal flux measurements, Mathur *et al.* [84] concluded that the heat transfer process during the initial stage of deposition was very high and that the corresponding thermal conductive heat transfer coefficient between deposited preform and substrate was approximately 10^5 W/m²K. Following a brief transient period, the magnitude of the heat transfer coefficient decreases to approximately 550 W/m²K under steady state condition for the copper substrate cooled by water. The convective heat transfer coefficient from the

27

top surface of the preform to the atmosphere at the end of deposition is assumed to be at least one order of magnitude smaller than the conductive heat transfer coefficient from the bottom surface of the preform to the substrate [27]. Therefore, in this study, heat transfer coefficients of 21 and 550 W / m²K were used for the top and bottom surfaces of the preform, respectively, when the substrate material was copper, which represents the highly conductive substrate case. In addition, in order to investigate the effect of different cooling conditions on the thermal residual stresses, the same analysis was performed using two different conductive heat transfer coefficients, which represent for an insulated substrate case and an intermediate case, respectively, with the same convective heat transfer coefficient of 21 W/m²K. The heat transfer coefficients used in this study are listed in Table 4-2. The radiative heat transfer was not considered in this study, since its effect becomes significant only when the temperature of the deposited preform is extremely high [83]. Throughout the modeling of three different cases, the same initial temperature condition of the preform was used in order to focus on the effect of the substrate with different thermal conductivities. The ambient temperature was assumed to be 300 K.

Table 4-2. Heat transfer coefficients used for the modeling

Substrate Material	Conductive Heat Transfer Coefficient (W/m²K)	Convective Heat Transfer Coefficient (W/m²K)
Highly Conductive (Cu)	550	21
Intermediate	275	21
Insulated	0	21

4.3. Results and Discussion

Figures 4-4, 4-5, and 4-6 show the von Mises' equivalent stresses along the top, middle, and bottom layers in the preform as indicated in Figure 4-3. For the conductive substrate cases, the equivalent stresses have higher values for the region closer to the outer edge of the preform. In other words, the stresses increase as the deposit thickness decreases. This is due to the fact that the region with lower deposit thickness experiences higher thermal gradient during cool down. The region closer to the edge of the preform has stresses that are greater than 410 MPa, which is the yield stress of γ-TiAl at 300 K.

Therefore, plastic deformation or possibly cracks may develop in that region. For the insulated substrate case, however, the equivalent stress distribution is significantly reduced and exhibits a relatively homogeneous pattern for the three different layers as compared with those of two other cases. Overall, it was found that the equivalent stress distribution is a strong function of cooling rate in the preform and the deposit thickness. It was also found that the equivalent stresses decrease as the conductive heat transfer coefficient (h) decreases.
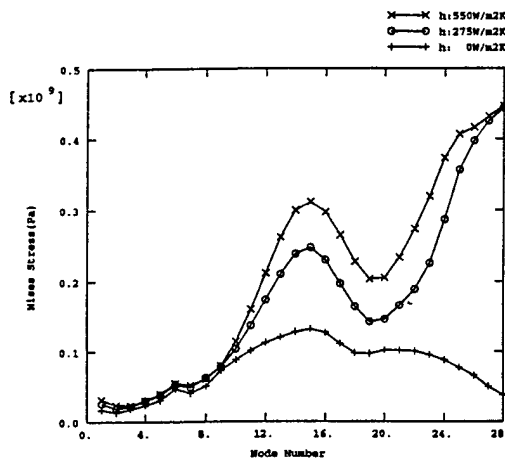
Figure 4-4. The von Mises' stresses along the top layer in the preform for three different cooling conditions.
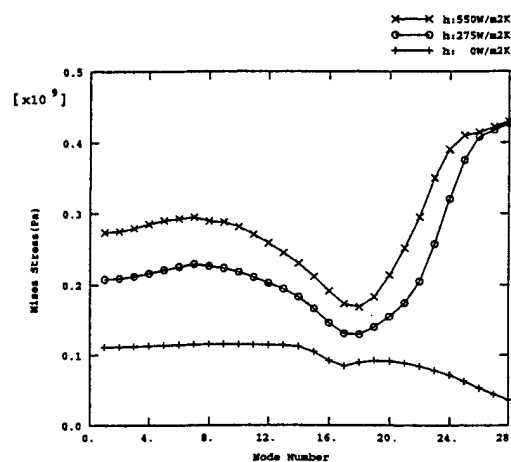
Figure 4-5. The von Mises' stresses along the middle layer in the preform for three different cooling conditions.

Figure 4-7 shows the equivalent stresses at the center of the preform as a function of distance along the z direction from the top to bottom of the preform. In the center region, it was found that the stress reaches the maximum value, and the stress distribution decreases as the h decreases. Depending on the h value, the maximum stress varies from 110 to 280 MPa. It was also noticeable that as the h decreases, the stresses in the center region gradually tend to be flattened.

The radial, hoop, and axial stresses along the center line of the preform are shown in Figures 4-8, 4-9, and 4-10, respectively. The radial stresses are mostly tensile for the upper region of the preform and compressive for the lower region of the preform for all three cases considered in this study. A similar trend can be observed for the hoop stresses. The axial stresses, however, are compressive for the entire preform. The magnitude of these

stresses increases as the distance from the top of the preform increases (*i.e.,* closer to the bottom of the preform). Again, the radial, hoop, and axial stresses decrease as the thermal conductivity of the substrate decreases.

Figure 4-6. The von Mises' stresses along the bottom layer in the preform for three different cooling conditions.
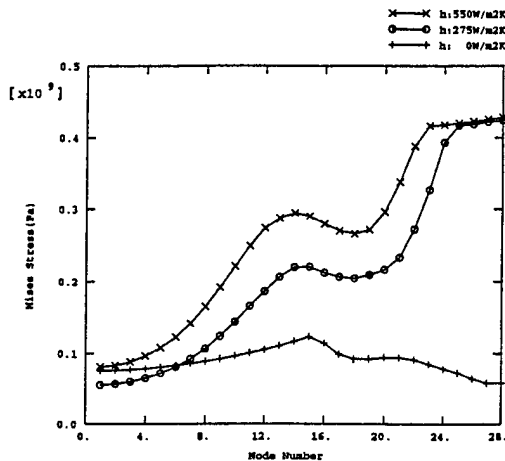

Figure 4-7. The von Mises' stresses at the center of the preform as a function of distance along the Z direction from the top to bottom of the preform for three different cooling conditions.
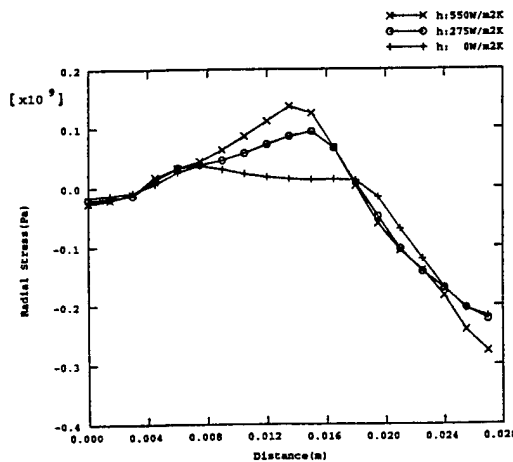
Figure 4-8. The radial stresses at the center of the preform as a function of distance along the Z direction from the top to bottom of the preform for three different cooling conditions.
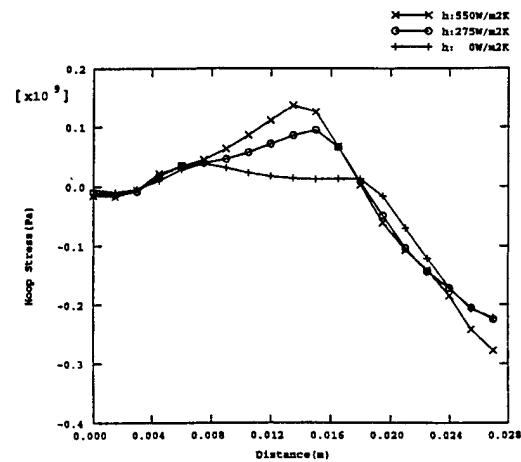
Figure 4-9. The hoop stresses at the center of the preform as a function of distance along the Z direction from the top to bottom of the preform for three different cooling conditions.

Figures 4-11, 4-12, and 4-13 show the radial, hoop, and axial stresses along the middle layer of the preform. The radial stresses in this region are mostly tensile for the entire preform, and these values are greatly reduced when the

X——X h:550W/m2K
O——O h:275W/m2K
+——+ h: 0W/m2K

X——X h:550W/m2K
O——O h:275W/m2K
+——+ h: 0W/m2K
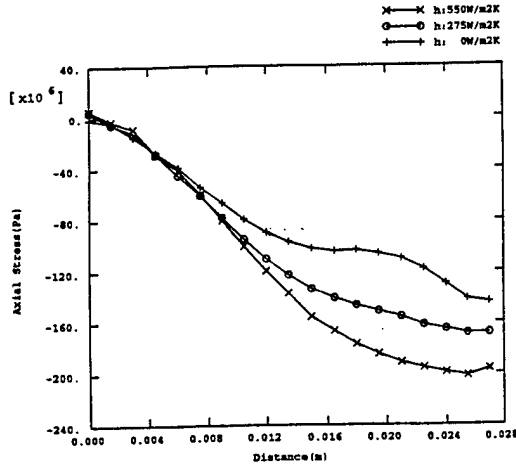
Figure 4-10. The axial stresses at the center of the preform as a function of distance along the Z direction from the top to bottom of the preform for three different cooling conditions.

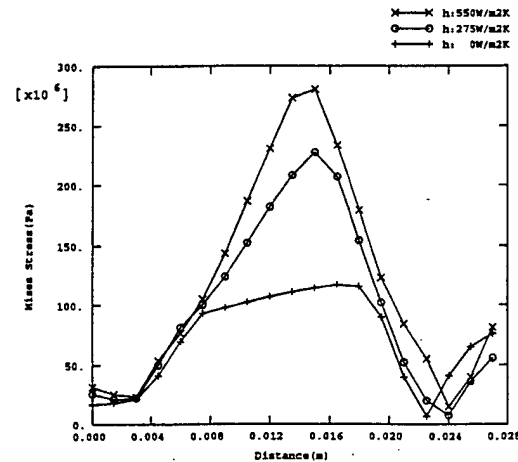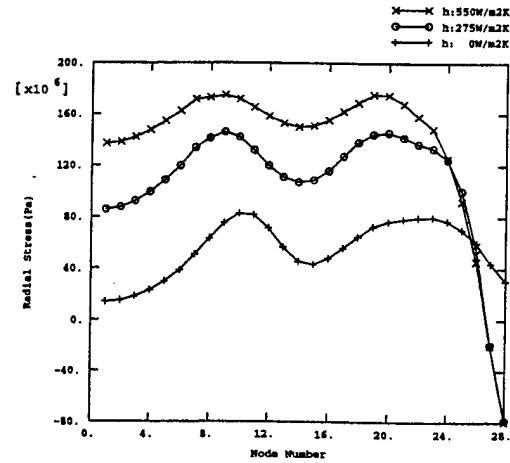**Figure 4-11.** The radial stresses along the middle layer of the preform for three different cooling conditions.
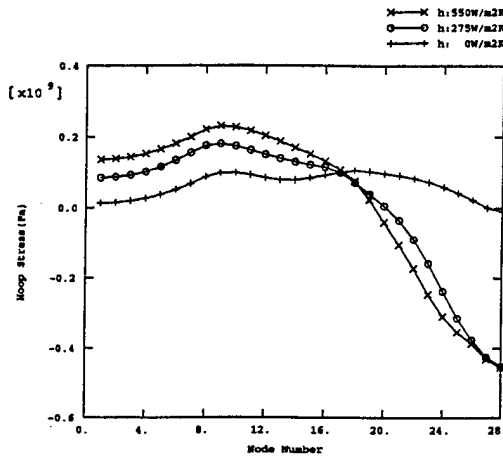
Figure 4-12. The hoop stresses along the middle layer of the preform for three different cooling conditions.
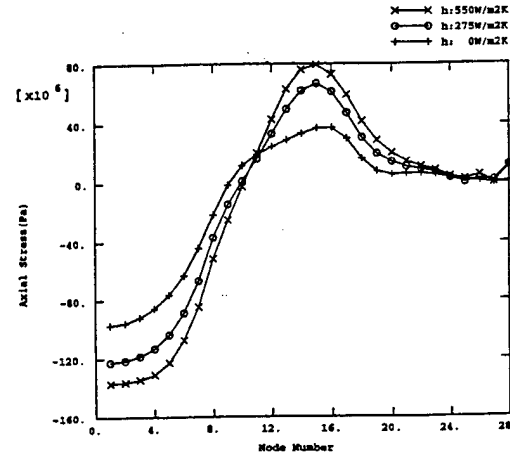
Figure 4-13. The axial stresses along the middle layer of the preform for three different cooling conditions.

insulated substrate case is considered. On the other hand, the hoop stresses are tensile for the inner area of the preform and compressive for the outer area of the preform for the conductive substrate cases. When the substrate is insulated, the hoop stresses become tensile for the entire preform. Contrary to the hoop stress distribution, the axial stress distribution exhibits compressive values for the inner area of the preform and tensile values for the outer area of the preform.

31

4.4. Summary

Based on the present study, the following conclusions were made:

1. Thermal residual stresses were developed in the spray formed γ-TiAl during cooling from the deposition temperature to ambient temperature.

2. The axial, hoop, and radial stresses were found to be mostly compressive for the lower center region of the preform. The magnitude of these compressive stresses increases for the region closer to the bottom of the preform. For the other region, the axial, hoop, and radial stresses become tensile.

3. The residual stress distribution is a strong function of cooling rate in the deposited preform, and the residual stresses decrease as the cooling rate decreases. When the substrate is insulated, the preform has the lowest residual stress distribution for the cases studied herein.

4. The residual stress distribution is a strong function of deposit thickness. For the region closer to the outer edge of the preform, which experiences the most severe thermal gradient, has the highest residual stresses. The von Mises' equivalent stresses in this region were found to be greater than the yield stress of γ-TiAl. Therefore, it is anticipated that plastic deformation or cracks may be present in this region of the preform.

CHAPTER 5.

TWO DIMENSIONAL MODELING OF MOMENTUM AND THERMAL BEHAVIOR DURING SPRAY ATOMIZATION OF γ-TiAl

5.1. Objective

The present study was undertaken with the objective of formulating a two-dimensional model to investigate the thermal and momentum behavior of γ-TiAl during spray atomization. A specific alloy composition of Ti-48 at.%Al was selected for study due to recent development of commercial alloys based on this stoichiometry: Ti-48Al-2.5Nb-0.3Ta [2], Ti-48Al-2Nb-2Zr [2], Ti-48Al-2V [14] and Ti-48Al-2Cr-2Nb [85] (All are in atomic percentage).

5.2. Model Formulation

The primary assumptions underlying the problem formulation that will be discussed in subsequent sections are listed as follows:

(1). The alloy melt is atomized instantaneously in a small atomization zone, whose magnitude is approximately 3~4 times the inside diameter (~0.001 m) of a metal delivery tube.

(2). Following atomization, the concentration of the droplets in the gas environment is sufficiently dilute, so that the droplet-droplet interactions may be safely neglected.

(3). The flow of the atomization gas is axisymmetric. As a result, the droplets do not experience rotation around the spray cone axis. The motion of the droplets is then assumed to be two dimensional. Accordingly, a radial coordinate system, (r, Z), is selected for the present problem, where r represents the radial distance and Z represents the axial distance. The coordinate system is shown schematically in Figure 5-1.
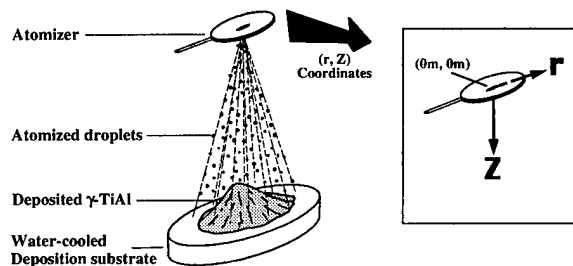
Figure 5-1. Schematic representation of the spray atomization and deposition process. The radial coordinate system, (r, Z), is shown in the insert on the right hand side.

33

(4). The (r, Z) coordinates at the center of the atomization zone are selected to correspond to (0m, 0m), where the radial droplet velocity is zero, and the axial droplet velocity has a relatively small value (for example, 1 m/s) as a result of the initial free fall of the alloy melt. Consistent with assumption (1), the initial positions, (r_0, Z_0), of atomized droplets will be in the range from (0m, 0m) to (0m, 0.004m). In addition, it is also assumed in the present study that droplets are randomly distributed in the atomization zone once they are formed.

5.2.1. Momentum profile of atomization gas

Based on the experimental results by Bewlay et al. [86] and Grant et al. [87], in which the geometry of the close-coupled atomization device used is similar to that used in the present investigation, the velocity profile of the atomization gas may be described as follows [88, 89]:

$$\upsilon_{zg}(0,Z) = \upsilon_{g0} \exp(-Z/\lambda) \tag{5-1}$$

with
$$\lambda = 3.04 \times 10^{-4} \upsilon_{g0}^{1.24} \tag{5-2}$$

and
$$\upsilon_{zg}(r,Z) = \upsilon_{zg}(0,Z)[1 - (\frac{r}{0.004 + 0.268Z})^{1.5}]^2 + \upsilon_{\infty} \tag{5-3}$$

$$\upsilon_{rg}(r,Z) = \upsilon_{zg}(r,Z)(\frac{r}{0.015 + Z}) \tag{5-4}$$

where υ_{zg} and υ_{rg} are the axial and radial components of gas velocity, respectively; υ_{g0} is the initial gas velocity; υ_{∞} is the axial gas velocity at Z= ∞; and λ is the exponential decay coefficient.

Eqns. (5-3) and (5-4) are applicable only for r/(0.004+0.268Z)<1, i.e., inside the spray cone. When r/(0.004+0.268Z)≥1, it is reasonable to assume that $\upsilon_{zg}(r, Z)$ and $\upsilon_{rg}(r, Z)$ are both close to zero.

5.2.2. Velocity profile of droplets

During atomization, droplets are subjected to an accelerating or decelerating drag force as a result of the differences in velocity between droplets and atomization gas [90]:

$$\rho_d V \frac{d\upsilon_{zd}}{dt} = V(\rho_d - \rho_g)g + (A/8)C_{drag}\rho_g(\upsilon_{zg} - \upsilon_{zd})U_{dg} \tag{5-5}$$

$$\rho_d V \frac{d\upsilon_{rd}}{dt} = (A/8)C_{drag}\rho_g(\upsilon_{rg} - \upsilon_{rd})U_{dg} \tag{5-6}$$

34

where ρ_d and ρ_g are the densities of droplet and atomization gas (Ar), respectively; V and A are the volume and surface area of droplet, respectively; υ_{zd} and υ_{rd} are the axial and radial components of droplet velocity, respectively; U_{dg} ($=[(\upsilon_{zg}-\upsilon_{zd})^2+(\upsilon_{rg}-\upsilon_{rd})^2]^{1/2}$) is the relative velocity between gas and droplet; C_{drag} is the drag coefficient; and g is the gravity constant.

Droplet-droplet interactions, Basset history term and added mass effect [90] are neglected in Eqns. (5-5) and (5-6) since these terms are generally much smaller than the inertia and the drag forces in processes such as spray atomization.

A well known relationship between the drag coefficient, C_{drag}, and the Reynolds number, N_{Re} ($=D\rho_g U_{dg}/\mu_g$, where D is the droplet diameter and μ_g the gas viscosity), is $C_{drag} = 0.28 + (6/N_{Re}^{0.5}) + (21/N_{Re})$ [91], which is applicable for $0.1<N_{Re}<4000$. In the present study, N_{Re} falls into a wider range (i.e. 0.02—8000) than the one mentioned above. Therefore, an improved expression for C_{drag}, as a function of N_{Re}, may be used as described in reference [89]:

$$C_{drag} = \begin{cases} 24/N_{Re} & 0 < N_{Re} < 1 \\ 24/N_{Re}^{0.646} & 1 \leq N_{Re} < 400 \\ 0.5 & 400 \leq N_{Re} < 3 \times 10^5 \end{cases} \qquad (5-7)$$

Using Eqns. (5-5)-(5-7), together with the gas velocity profiles calculated from Eqns. (5-1)-(5-4) and the parameters listed in Table 5-1, the two-dimensional trajectory and velocity profile of a given droplet may be calculated numerically once r_0 and $\upsilon_{zd}(r,0)$ are given.

5.2.3. Thermal and solidification history of droplets

In terms of T_I, T_N, T_L and T_P, which represent initial, nucleation, liquidus and peritectic temperatures of γ-TiAl, respectively, the thermal and solidification profiles of γ-TiAl may be classified into five well defined stages (refer to Figure 5-2 and Figure 5-7): (1) cooling in the liquid state when $T_N<T<T_I$, (2) recalescence when $T=T_N$, (3) segregated solidification when $T_P<T\leq T_L$, (4) peritectic solidification when $T=T_P$, and (5) cooling in the solid state following the completion of solidification. Before any detailed calculation of the droplet

thermal and solidification histories can be accomplished, the values of T_I, T_N, T_L and T_P need to be determined first. T_I may be determined from the degree of melt superheat; T_L and T_P may also be easily obtained according to Ti-Al phase diagram (Figure 5-2). The determination of T_N, however, requires detailed knowledge of the relevant solidification kinetics. Relevant formulation is described in more detail below.

Table 5-1. Physical parameters used in Eqns. (5-1) through (5-20)

parameter	value	source
C_{pg}	518.8 $Jkg^{-1}K^{-1}$	[92, 93]
C_{pl}	829 $Jkg^{-1}K^{-1}$	RMA*
C_{ps}	727 $Jkg^{-1}K^{-1}$	RMA
H_f	28.27 $kJmol^{-1}$	[Eqn. (5-21)]
k_e	0.74	[Fig. 2]
k_g	0.01636 $Wm^{-1}K^{-1}$	[92, 93]
R	0.01 $ms^{-1}K^{-1}$	[94]
T_I	1885 K	[12]
T_L	1785 K	[12]
T_M	2016 K	[12]
T_P	1764 K	[12]
T_{0i}	273 K	[92]
T_{0f}	473 K	[84]
α	0.1 m	[88]
υ_{g0}	150 ms^{-1}	[86, 88]
υ_∞	0.004 ms^{-1}	[86]
ε	0.5	[89]
μ_g	$1.7 \times 10^{-5}\, kgm^{-1}s^{-1}$	[92]
μ_m	$3.6 \times 10^{-3}\, kgm^{-1}s^{-1}$	RMA
ρ_d	3636 kgm^{-3}	RMA
ρ_g	1.654 kgm^{-3}	[92, 93]
σ_m	$203.4 \times 10^{-6}\, kJm^{-2}$	[Eqn. (5-22)]
Ω	$2.08 \times 10^{-5}\, m^3mol^{-1}$	RMA

*Rule of mixtures approach.

Based on the work of Hirth [95] and Turnbull [96], the maximum homogeneous undercooling ΔT_{hom} ($=T_L-T_N$) for a given droplet may be calculated as follows:

$$\Delta T^2_{hom} = \frac{16\pi\sigma^3_m\Omega^2 T^2_L}{3k(T_L - \Delta T_{hom})H^2_f \ln[10^{44}V\Delta T_{hom}/\dot{T}]} \qquad (5\text{-}8)$$

where H_f, σ_m and Ω are the latent heat of fusion, the solid-liquid interface energy and the atomic volume of γ-TiAl, respectively; k is the Boltzmann's constant; V is the droplet volume in m^3; and $\dot{T}$ is the cooling rate of droplet in the first stage, namely cooling in the liquid state.

As may be seen later (refer to Section 5.4.4), $\dot{T}$ depends strongly on the droplet size (D), initial position (r_0), and axial distance from the atomization zone (Z). As an approximation, a value averaged on different r_0 and Z was used for each droplet considered in present study. This is justified by results of numerical solution of Eqn. (5-8), which indicate that the value of ΔT_{hom} is relatively insensitive to the changes in $\dot{T}$.
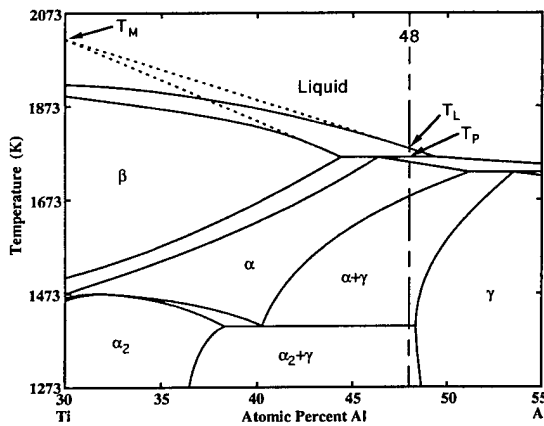
Figure 5-2. Central part of the equilibrium Ti-Al phase diagram [12, 18]. Dotted lines are drawn for calculation of k_e and T_M in equations (5-18) and (5-19). Dashed line represents the alloy composition in the present study.
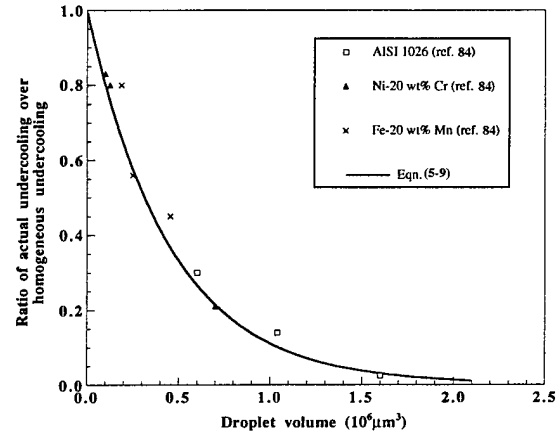
Figure 5-3. Relationship between actual undercooling, homogeneous undercooling and droplet size.

It is well established, nevertheless, that heterogeneous rather than homogeneous nucleation mechanisms limit the degree of undercooling experienced by a large proportion of the droplet population during atomization [84, 97]. Only in very small droplets (e.g., D≤20 μm) does homogeneous nucleation play an important role during solidification. Accordingly, the actual degree of undercooling experienced by a droplet, ΔT_{actual}, will generally be significantly smaller than the undercooling necessary for homogeneous nucleation, ΔT_{hom}. Based on experimental results

of Mathur et al. [84], an exponential relationship between ΔT_{actual} and ΔT_{hom} may be formulated as (Figure 5-3):

$$\Delta T_{actual} = \Delta T_{hom} \exp(-2.2 \times 10^{12} V) \qquad (5\text{-}9)$$

It should be noted that the degree of undercooling that is present during heterogeneous nucleation is controlled by the availability of heterogeneous nucleation sites in the volume or surface of the droplet and the wetting angle between nucleant and melt. However, the availability of heterogeneous nucleants is more important than the wetting angle between nucleant and melt. The former strongly depends on the droplet size [98, 99]. Accordingly, $\Delta T_{actual}/\Delta T_{hom}$ for a specific droplet during atomization is more significantly affected by droplet size than by alloy composition (ΔT_{hom} has already taken into account some of the effects derived from the alloy composition). Actually, the experimental results obtained by Mathur et al. [84] reveal that $\Delta T_{actual}/\Delta T_{hom}$ is relatively insensitive to chemical composition of the materials sprayed (see Figure 5-3). Therefore, the applicability of Eqn. (5-9) is extended to the γ-TiAl studied herein, despite the fact that this correlation was originally formulated on the basis of experimental results obtained for Ni-20 wt.% Cr and Fe-20 wt.% Mn.

Eqns. (5-8) and (5-9) may be used to calculate ΔT_{actual} and then T_N (=T_L-ΔT_{actual}) for any droplet with a given size (D or V). The values of ΔT_{actual} calculated for the range of droplet sizes studied herein are listed in Table 5-2. Generally, experimental measurement of the magnitude of undercooling experienced by droplets during spray atomization is very difficult. To that effect, inspection of available literature indicates that there is no experimental data reported so far on the undercooling experienced by atomized γ-TiAl droplets during spray atomization. It is worth noting, however, that in a related study conducted by Valencia et al. [100], an undercooling as large as 286 K was experimentally achieved using a levitation technique for a Ti-50Al droplet with a diameter of approximately 5000 μm.

Table 5-2. Calculated actual undercooling of γ-TiAl with various droplet sizes

size(μm)	20	50	80	175	325	500
undercooling(K)	469	393	247	1	0	0

5.2.3.1. Cooling in the liquid state ($T_N \leq T < T_l$)

In a completely molten droplet, thermal energy is dissipated into the environment via a combination of convection and radiation until T_N is reached:

$$-\rho_d V C_{pl} \frac{dT}{dt} = h(T - T_0)A + \varepsilon\sigma(T^4 - T_0^4)A \qquad (5\text{-}10)$$

where C_{pl} is the specific heat of liquid γ-TiAl; ε is the emissivity of the surface; σ is the Stephen-Boltzmann constant; h is the convection heat transfer coefficient, which may be expressed as [101]:

$$h = (k_g/D)[2 + 0.6N_{Re}^{1/2}N_{Pr}^{1/3}] \qquad (5\text{-}11)$$

where N_{Pr} ($= \mu_g C_{pg}/k_g$) is the Prandtl number; k_g and C_{pg} are the thermal conductivity and the specific heat of gas, respectively; and T_0 is the temperature of the gas, which is assumed to increase exponentially as a result of heat transfer between the gas and the droplets [88]:

$$T_0 = T_{0f} - (T_{0f} - T_{0i})\exp(-Z/\alpha) \qquad (5\text{-}12)$$

where T_{0i} and T_{0f} are initial and final gas temperatures, respectively; and α is a constant.

The approximation of Newtonian cooling underlying Eqn (5-10) is acceptable when the magnitude of the Biot number, Bi ($= [h(D/2)]/k_d$, where k_d is the thermal conductivity of droplet), is less than 0.1 [92, 102]. In the present study, Bi<0.012.

Eqns. (5-10)-(5-12), along with the values of T_I and T_N may be used to predict the temperature, T, for a given droplet at any time, t, or any position, (r, Z). In this stage the fraction of solid, f, contained in a droplet is, by definition, zero.

5.2.3.2. Recalescence ($T=T_N$)

Recalescence is the rapid heating of an undercooled molten sample due to the nucleation of the solid phase. Since recalescence is driven by the magnitude of the undercooling present, as the droplet heats up the rate of heat release decreases and recalescence terminates when the rate of heat release becomes equal to the rate of heat extraction from the outer surface of the droplet:

$$H_f[\rho_d V(1 - f_r)]\frac{df}{dt} = h(T_r - T_0) \qquad (5\text{-}13)$$

where f_r and T_r are the fraction solidified in the droplet and the temperature of the droplet at the end of recalescence, respectively.

39

The rate of growth of solid phase in undercooled melt with small to moderate undercoolings may be given by [94]:

$$\frac{df}{dt} = \frac{R\Delta T}{D}$$ (5-14)

in which R is the solid/liquid interface mobility, and $\Delta T = T_L - T_r$ at the end of recalescence.

By establishing a thermal energy balance between the latent heat released and the thermal energy that is needed to accommodate the temperature rise in the droplet, f_r in Eqn. (5-13) may be calculated as:

$$H_f f_r = (T_r - T_N)[C_{pl}(1-f_r) + C_{ps}f_r]$$ (5-15)

where C_{ps} is the specific heat of solid γ-TiAl.

Using Eqns. (5-13)-(5-15), the droplet temperature and the fraction solidified at the end of recalescence may be readily determined. Detailed calculations indicate that, when $(h/(\rho_d C_{ps}R)) < 2$ K, Eqns. (5-13)-(5-15) may be approximated as

$$T_r^2 - (\frac{H_f}{C_{ps}} + T_L + T_N)T_r + \frac{H_f}{C_{ps}}T_L + T_L T_N = 0$$ (5-16)

Taking into account the fact that $T_r \leq T_L$, then Eqn. (5-16) is equivalent to

$$T_r = \begin{cases} T_L \dots\dots\dots\dots\dots\dots(H_f/C_{ps}) + T_N > T_L \\ T_N + (H_f/C_{ps}) \dots\dots\dots(H_f/C_{ps}) + T_N \leq T_L \end{cases}$$ (5-17)

In the present study, the values of $h/(\rho_d C_{ps}R)$ are smaller than 1.41 K for droplet sizes corresponding to D≥20 μm.

In addition, available results reveal that the time interval that is associated with the recalescence phenomenon is less than 10^{-6} seconds [103]. Therefore, it is safe to assume that the recalescence is essentially complete within a single calculation step in present study (which is in the order of milliseconds).

5.2.3.3. *Segregated solidification* ($T_P \leq T \leq T_L$)
The segregation behavior of the solute following the completion of recalescence may be described by the Scheil equation [104], the Brody-Flemings theory [105], the Bower-Brody-Flemings theory [106] and the Clyne-Kurz

theory [107]. However, it was found that the selection of a particular theory has only a limited effect on the overall cooling behavior of atomized droplets [88]. Therefore, because of its simplicity, the Scheil equation is employed to describe segregation behavior in the present study:

$$(c_l - c_s)df = (1-f)dc_l \qquad (5\text{-}18a)$$

or, after being integrated,

$$f = 1 - (1 - f_r)(\frac{c_l - 30}{c_0 - 30})^{1/(k_e - 1)} \qquad (5\text{-}18b)$$

where c_0, c_s and c_l are the initial, solid and liquid composition of solidifying γ-TiAl droplet, respectively; and k_e [$=(c_s-30)/(c_l-30)$, refer to Figure 5-2] is a constant similar to the conventional equilibrium coefficient.

Writing c_l and c_0 in terms of T, T_L and T_M yields:

$$f = 1 - (1 - f_r)(\frac{T_M - T}{T_M - T_L})^{1/(k_e - 1)} \qquad (5\text{-}19a)$$

and

$$\frac{df}{dT} = \frac{1 - f_r}{(k_e - 1)(T_M - T_L)}(\frac{T_M - T}{T_M - T_L})^{\frac{2-k_e}{k_e - 1}} \qquad (5\text{-}19b)$$

where T_M is a reference temperature as defined in Figure 5-2.

The thermal energy balance governing the thermal history of the droplet during this stage is identical to that described by Eqn. (5-10) if C_{pl} is substituted with $C_{pl}(1 - f) + C_{ps}f - H_f\frac{df}{dT}$, in which the third term takes into account the latent heat released during solidification.

5.2.3.4. *Peritectic solidification* ($T=T_P$)

In this stage, the droplet temperature remains at the peritectic temperature, T_P, until the droplet is completely solidified. It then follows that the fraction of solid present in the droplet, as a function of time or position may be expressed as:

$$\rho_d H_f V\frac{df}{dt} = h(T_P - T_0)A + \varepsilon\sigma(T_P^4 - T_0^4)A \qquad (5\text{-}20)$$

5.2.3.5. *Cooling in the solid state* ($f=1$)

In this stage, $f=1$ and the associated thermal energy balance is established by using Eqn. (5-10), and substituting C_{ps} for C_{pl}.

5.3. Numerical Solution

Computer programs have been prepared for the execution of the calculations required by Eqns. (5-1) through (5-20). The primary point of the present computational exercise is to concentrate on a given droplet, formed near the atomization point (e.g. $Z_0=0$ m, $r_0=0.001$ m), having a particular diameter (say 80 μm), and then follow its two-dimensional trajectory as it travels down the atomization chamber.

Numerical calculation will be carried out for each pair of droplet size and droplet initial position, $\{D, (Z_0, r_0)\}$. Consistent with the results of Moll et al [108], the characteristic sizes, D_{16}, D_{50} and D_{84}, which represent droplet diameters for which 16 wt. %, 50 wt. % and 84 wt. % of droplets are smaller than these values, respectively, were selected to be 80 μm, 175 μm and 325 μm in the present study. Although D_{16}, D_{50} and D_{84} of atomized powders strongly depend on the processing parameters, such as atomization gas pressure, superheat temperature and metal/gas flow ratio, the selection of a particular powder size distribution does not affect the primary conclusions which will be drawn later. Taking into account the maximum droplet size (~500 μm) and the minimum droplet size (~20 μm) that are generally encountered during atomization, the droplet sizes 20 μm, 50 μm, 80 μm, 175 μm, 325 μm and 500 μm are selected for calculation in the present study. Following assumptions (1) and (4) in Section 5.2, representative initial positions $r_0=$ 0 m, 0.00001 m, 0.0001 m, 0.001 m, 0.002 m and 0.003 m are chosen for numerical calculation (Z_0 remains to be zero for all values of r_0). Therefore, the diameter-initial position pairs will be {20μm, (0m, 0m)}, {20μm, (0m, 0.00001m)}, {20μm, (0m, 0.0001m)}, {20μm, (0m, 0.001m)}, {20μm, (0m, 0.002m)}, {20μm, (0m, 0.003m)}, ..., {500μm, (0m, 0.002m)}, {500μm, (0m, 0.003m)}.

No experimental values are available for some of the physical properties of γ–TiAl. In this case, a simple rule of mixtures approach was used.

The heat of fusion of γ-TiAl is determined on the basis of information in reference [109] as follows:

42

$$\frac{H_f^{\gamma}(J/mol)}{T_m^{\gamma}(K)} = 0.52\frac{H_f^{Ti}(J/mol)}{T_m^{Ti}(K)} + 0.48\frac{H_f^{Al}(J/mol)}{T_m^{Al}(K)} + 5.76(J/mol \cdot K) \qquad (5\text{-}21)$$

where the superscripts γ, Ti, Al denote the properties of γ-TiAl, Ti, and Al, respectively; and subscript m denotes melting temperature.

The solid/liquid interfacial energy of γ-TiAl is calculated using [110]:
$$\sigma_m(J/m^2) = 0.46H_f(J/atom)[\Omega(m^3/atom)]^{-2/3} \qquad (5\text{-}22)$$

The experimentally determined and calculated physical properties of γ-TiAl used in the present study are summarized in Table 5-1.

5.4. Results and Discussion

5.4.1. Velocity evolution of gas and droplets in spray cone

Figure 5-4 shows the axial gas velocity and droplet velocities for different droplet sizes along the axial line ($r_0=0$ m) as a function of the axial distances. Initially, a droplet is accelerated to a maximum velocity, and then subsequently decelerated by the environmental gas. The results reveal that the maximum velocity achieved by a droplet increases with decreasing droplet size. This is consistent with the results anticipated from Eqns. (5-5) and (5-7), which suggest that, the smaller a droplet is, the larger the magnitude of the force acted on it becomes. It is worth noting that the present problem formulation assumes that
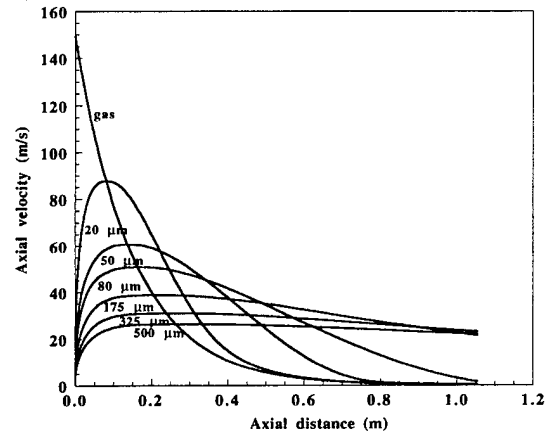
Figure 5-4. Axial gas velocity and droplet velocities with different droplet sizes along the spray central line. Droplet sizes are 20 μm, 50 μm, 80 μm, 175 μm, 325 μm and 500 μm.

there is no radial velocity component when $r_0=0$ m, i.e., it regresses to the one dimensional problem when $r_0=0$ m. Actually, the results summarized in Figure 5-4 are qualitatively similar to the one dimensional results obtained in earlier studies [88, 92].

Figure 5-5 shows the calculated axial (Figure 5-5(a)) and radial (Figure 5-5(b))

components of droplet velocities and gas velocities with $r_0=0.001$ m. Only results for 20 μm and 500 μm droplets are shown here. Comparison of Figure 5-5(a) to Figure 5-4 reveals that both the gas velocity and the maximum axial droplet velocity (for the same droplet size) in Figure 5-5(a) are smaller than those in Figure 5-4. Detailed calculation reveals that, the maximum axial component of gas and droplet velocities decreases with increasing r_0. Another distinct difference between the results shown in Figure 5-4 and Figure 5-5(a) is the gas velocities. It should be noted here that the gas velocities, both in Figure 5-4 and Figure 5-5, are referred to as the velocity of gas in the vicinity of droplets. Accordingly, although the entire gas velocity profile in the spray cone is independent of r_0, the gas velocities in the vicinity of the droplets may be different if the trajectories of these droplets are different than each other. It is evident from Eqn. (5-3) that the axial component of gas velocity is a function of r and Z, i.e., the trajectory of droplet. For $r_0=0$ m, the trajectories for different droplets fall into one line, i.e., the central line of the spray cone, as a result of the absence of a radial velocity component in this case. Therefore, when $r_0=0$ m, the axial component of gas velocity remains the same for all droplets (Figure 5-4). When r_0 deviates from zero, however, the trajectories of droplets with various diameters become different from each other (refer to Section 5.4.2), and consequently the gas velocities in the vicinity of different droplets will be different from each other (Figure 5-5(a)). As will be shown in Section 5.4.2, at any given axial distance, the radial distance corresponding to a 500 μm droplet is smaller than that of a 20 μm droplet. This calculated result, along with Eqn. (5-3), imply that the gas velocity in the vicinity of a 500 μm droplet should be larger than that of a 20 μm droplet. The velocity profiles in Figure 5-5(b) are almost the same as those shown in Figure 5-5(a). It is worth noting, however, that the radial velocity values for both droplet and gas are
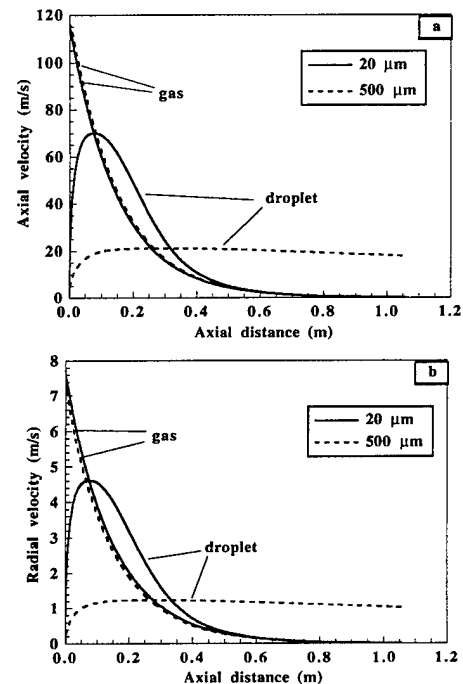
Figure 5-5. Gas and droplet velocities for 20 μm and 500 μm droplets with an initial radial position, r_0, of 0.001 m: (a) axial component and (b) radial component.

44

much smaller than the axial ones. For example, the maximum radial velocity achieved by a 20 μm droplet is 4.6 m/s, while the axial one is 70 m/s. This difference is qualitatively consistent with available experimental observations [86], in which the radial component of droplet velocity is found to be smaller than the axial one. Moreover, the radial component of gas velocity in the vicinity of a 500 μm droplet, contrary to the case of the axial component, is smaller than that in the vicinity of a 20 μm droplet at any given axial distance. This may be understood from inspection of Eqns. (5-3) and (5-4), in which $\upsilon_{rg}(r, Z)$ is a function whose value increases with increasing r provided that r is not too large, while $\upsilon_{zg}(r, Z)$ is a function whose value decreases with increasing r. Regarding the influence of the value of r_0 on the radial component of gas and droplet velocities, it is found that, the maximum value of the radial component initially increases and then decreases with increasing r_0.

5.4.2. Droplet size distribution in spray cone

Figure 5-6 shows the trajectories of droplets of various diameters with $r_0=0.0001$ m and 0.003 m. The general trends observed for $r_0=0.003$ m may be summarized as follows. First, for a given axial distance which is smaller than some critical value (say, 0.75 m), the radial distance traveled by a droplet increases with decreasing droplet diameter. Second, for a given axial distance which is larger than the critical value, the radial location of droplets becomes random. The results obtained herein for all other initial conditions ($r_0=0$, 0.00001, 0.0001, 0.001 and 0.002 m) are qualitatively similar to those

Figure 5-6. Trajectories of droplet of different sizes for $r_0=0.0001$ m and $r_0=0.003$ m. Droplet diameters are 20 μm, 50 μm, 80 μm, 175 μm, 325 μm and 500 μm.

obtained with $r_0=0.003$ m. It is worth noting, however, that the radial distance range, Δr, at a given axial distance decreases with decreasing r_0. For example, when $r_0=0.0001$ m, the radial distance range Δr corresponding to any axial distance is so small that the trajectories of different droplets are almost

indistinguishable in Figure 5-6. In addition, for the same droplet size, droplets initially located at a larger r_0 will go farther in radial direction from the spray cone axis than that at a smaller r_0.

For an individual droplet, the radial distance corresponding to a given axial distance may be expressed as an integral of the product of flight time and the radial droplet velocity component. Consequently, there will be several factors influencing the radial distances traveled by droplets at a given axial distance, which finally leads to the calculated two dimensional droplet size distribution in the spray cone. For droplets with identical r_0, the radial droplet velocity component for a fine droplet is initially larger and then smaller than that corresponding to a coarse one (Figure 5-5(b)). Moreover, as will be discussed in a later section, the flight time for a given axial distance critically depends on droplet size. Combined, all of these effects result in the trajectory band for each r_0, as shown in Figure 5-6. The effect of r_0 on the radial distance traveled by a droplet may be attributed to two factors. First, to reach a given axial distance, droplets which are initially located at a larger r_0 will experience a longer flight time relative to those corresponding to a smaller r_0, as will be shown in Section 5.4.3. Second, as discussed in Section 5.4.1, the radial component of droplet velocity initially increases and then decreases with increasing r_0. Detailed calculations for other initial positions (r_0=0, 0.00001, 0.001 and 0.002 m) indicate that the radial distance traveled by a droplet is more significantly affected by changes in flight time than that in radial component of droplet velocity.

It may be envisioned that, if all the results calculated for different values of r_0 were to be shown in Figure 5-6, the trajectory bands for different values of r_0 will overlap with each other and a complete picture of the spatial distribution of droplets with different diameters in the spray cone will be obtained. As a result, when the axial distance is smaller than some critical value (say 0.75 m), coarse droplets tend to concentrate in the central region of the spray cone, whereas fine droplets populate the periphery; when the axial distance is larger than the critical value, the two dimensional droplet size distribution in the spray cone will be homogeneous. These calculated results are qualitatively consistent with the experimental results reported by McDonell et al. [111]. The experimental results of McDonell et al. [111] reveal that coarse droplets

46

concentrate in the central region of the spray cone at an axial distance of 0.025 m. When the axial distance increases from 0.025 m to 0.28 m, however, the two dimensional droplet size distribution becomes relatively insensitive to the radial position, i.e., from heterogeneous to almost homogeneous. The quantitative discrepancy between the results obtained herein and those obtained by McDonell et al. [111] may be attributed to the difference in material properties and process parameters. The study by McDonell et al. [111], for example, involved the atomization of water with air.

5.4.3. Flight time

The flight times corresponding to droplets with different sizes and initial conditions were calculated as a function of the axial distance. The calculated results reveal that, for the same values of r_0, there are two distinct regimes. For axial distances smaller than a critical value (e.g., 0.35 m for $r_0=0.0001$ m), flight time increases with increasing droplet size. This may be rationalized on the basis of the results shown in Figures 4 and 5(a), which reveal that fine droplets are readily accelerated and that the axial velocity component of fine droplets exceeds that of coarse droplets. Accordingly, the time elapsed during travel of a particular distance decreases with decreasing droplet size. When the axial distance is larger than the critical value, the flight time corresponding to finer droplets (i.e., 20 μm, 50 μm and 80 μm) increases rapidly to a much higher magnitude relative to that corresponding to coarse droplets (i.e., 175 μm, 325 μm and 500 μm). This behavior may be attributed to the fact that finer droplets are readily decelerated to very small velocity values once a maximum velocity has been achieved, while the velocities of coarse droplets remain almost unchanged once the maximum velocity has been attained (e.g., see Figures 4 and 5). When r_0 increases, flight time increases rapidly due to the differences in the magnitude of the axial velocity component of the droplets, as discussed in detail in Section 5.4.1.

5.4.4. Cooling rate

The cooling rates of a droplet in various thermal and solidification stages are completely different than each other, from being negative in recalescence stage to being zero in peritectic solidification stage, and to being positive in other three stages (cooling in the liquid state, cooling in the solid state and segregated solidification). Even in the same stage, cooling rate of a droplet

also critically depends on its droplet size, initial position and axial position. For example, the cooling rate in the stage of cooling in the liquid state ranges from 1.73×10^3 K/s to 1.55×10^6 K/s, depending on its droplet size, initial position and axial distance from the atomization zone. Detailed calculation of cooling rates for droplets of different sizes and different initial conditions, however, indicates that there are two distinct tendencies: i) cooling rate decreases significantly with increasing droplet size; and ii) cooling rate remains almost unchanged when r_0 increases. As evident from Eqn. (5-10), the difference between the calculated cooling rate for different values of D results from the variations in droplet volume, V, and heat transfer coefficient, h. The latter, h, is a complex function of D and U_{dg}, the relative velocity between gas and droplet. The influence of the value of r_0 on the calculated cooling rate may be inferred from the variation of U_{dg} under different r_0, as discussed in Section 5.4.1.
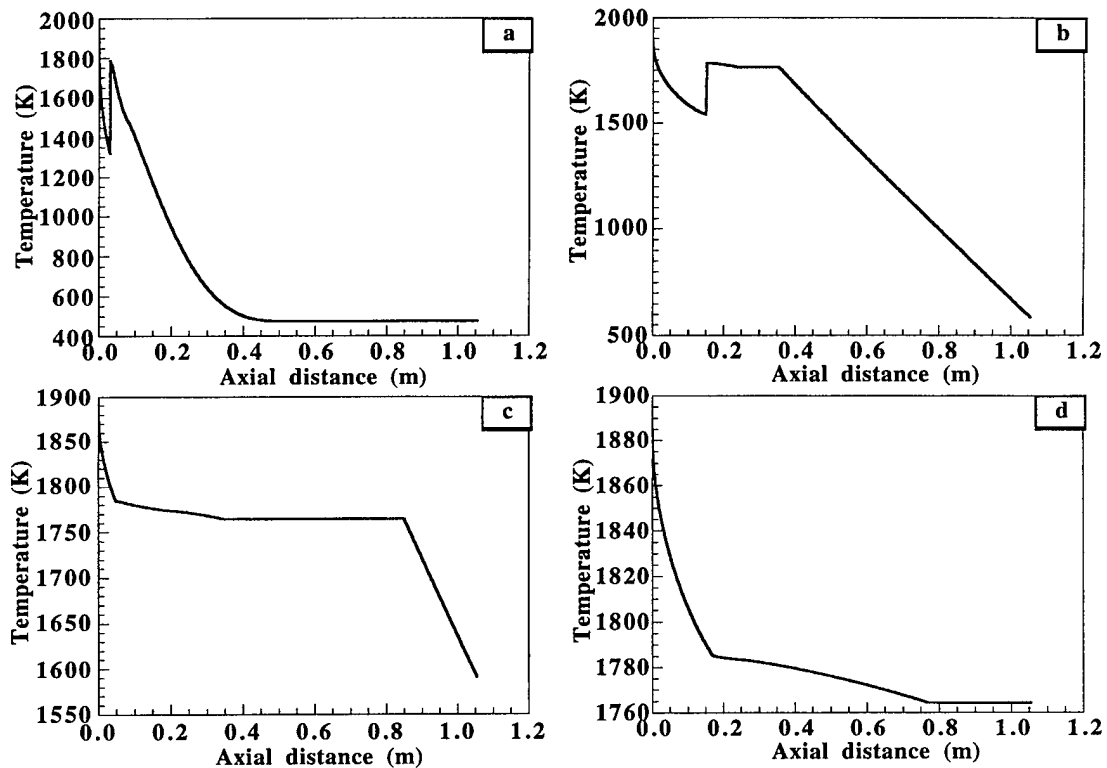
Figure 5-7. Thermal history of different droplets with initial radial position $r_0=0$ m: (a) D=20 μm; (b) D=80 μm; (c) D=175 μm and (d) D=325 μm.

5.4.5. Thermal history

Figure 5-7 shows the calculated thermal histories for droplets of different sizes assuming a value of $r_0=0$ m. All five stages described in Section 5.2.3 were

experienced by droplets with D=20 μm (Figure 5-7(a)) and D= 80 μm (Figure 5-7(b)). Some stages, such as recalescence and cooling in the solid state, are absent, depending primarily on droplet size. The disappearance of a recalescence stage in coarse droplets (D=175 μm and 325 μm) may be rationalized on the basis of the very small undercoolings that are associated with these droplets (see Eqn. (5-9)). The disappearance of the cooling in solid state stage, as noted for 325 μm droplets, is a result of their relatively lower cooling rate compared with those of finer droplets (see Section 5.4.4). Accordingly, in large droplets, the temperature is not sufficiently low in the calculated regime to develop this stage. Detailed calculation indicates that, when r_0 increases, the curve becomes steeper. This phenomenon is a result of the combined effects of the longer flight time and the relatively unchanged cooling rate with increasing r_0.

5.4.6. Solidification behavior

Figure 5-8 shows the solidification tendencies of droplets of different sizes for two different initial conditions (r_0=0.00001 m and 0.003 m). The results obtained for other initial conditions (r_0=0 m, 0.0001 m, 0.001 m and 0.002 m) are similar to

Figure 5-8. Solidification tendencies of different droplets with: (a) r_0=0.00001 m and (b) r_0=0.003 m. The droplet diameters are 20 μm, 50 μm, 80 μm, 175 μm, 325 μm and 500 μm.

those shown in Figure 5-8. There are two trends that are evident from the results summarized in Figure 5-8. The first one is that for some axial distance (say 0.14 m in Figure 5-8(a)), the fraction solidified in coarse droplets (0.13 in 175 μm droplets) is higher than that in fine droplets (0 in 80 μm droplets). The second one is that, once the nucleation temperature is reached in fine droplets (80 μm), they are more readily solidified relative to coarse droplets (175 μm) even if they start to nucleate much later than coarse ones. The first trend may be rationalized from the very small actual undercoolings

experienced by coarse droplets, which result in a much higher nucleation temperature relative to those experienced by fine droplets. Consequently, although fine droplets have higher cooling rate than coarse ones, it is still possible that in some cases the nucleation temperature of coarse droplets is reached earlier than that of fine droplets, i.e., coarse droplets start nucleation earlier than fine ones. The second trend may be understood from inspection of Eqns. (5-11), (5-14), (5-19b) and (5-20). For example, Eqn. (5-14), which describes the solidification occurring in the recalescence stage, implies that a smaller droplet size and a larger undercooling correspond to a higher solidification rate. A smaller droplet size also corresponds to a larger undercooling (Table 5-2). Therefore, fine droplets solidify at a higher rate relative to coarse ones during recalescence stage. Furthermore, the second trend is also consistent with the results obtained from the one dimensional modeling of spray atomization [88].

Comparison between Figure 5-8(a) and Figure 5-8(b) indicates that, for identical droplet sizes, the solidification fraction at a given axial distance increases with increasing r_0. This may be understood in terms of the flight time which increases rapidly with increasing r_0, as discussed in Section 5.4.3. A longer flight time will allow for more fraction being solidified provided that the droplets under investigation are not fully solidified.

The two dimensional solidification behavior of atomized γ-TiAl droplets in the spray cone may be elucidated through calculations of the average solid fraction, f_{avg}, for a collection of droplets which is initially located at an identical position, r_0. In a given collection of droplets, the average solid fraction in it may be estimated from [27]:

$$f_{avg} = (f_{16} + f_{84}) \times 32\% + f_{50} \times 36\% \qquad (5-23)$$

where f_{16}, f_{50} and f_{84} represent the solid fraction in characteristic droplets with diameters D_{16}, D_{50} and D_{84}, respectively.

The size distribution of a collection of droplets with identical initial position, r_0, may be assumed to be the same as that corresponding to the droplets formed in the atomization zone, provided that droplets are randomly distributed in the atomization zone once they are formed (refer to assumption (4) in Section 5.2). Accordingly, D_{16}, D_{50} and D_{84} in a collection of

droplets with a particular r_0 will be the same for all collections of droplets with different given initial positions, and representative of the size distribution of droplets formed in the atomization zone, which are 80 μm, 175 μm and 325 μm, respectively. Hence, f_{avg} for a collection of droplets with any particular r_0 may be obtained by using Eqn. (5-23) along with the magnitude of f_{16}, f_{50} and f_{84} in droplets with diameters of 80 μm, 175 μm and 325 μm, respectively. It should be noted that the solid fractions f_{16}, f_{50} and f_{84} are functions of the initial position, r_0.

The calculated f_{avg} as a function of axial distance is summarized in Figure 5-9 for $r_0=0$, 0.001 and 0.003 m. The effect of changing r_0 on the solidification behavior is evident there: the larger the value of r_0, the higher the solid fraction at a given axial distance. As mentioned in Section 5.4.2, for identical droplet size (D), the radial distance traveled by a droplet at any given axial distance increases with increasing r_0, i.e., if a substrate is inserted
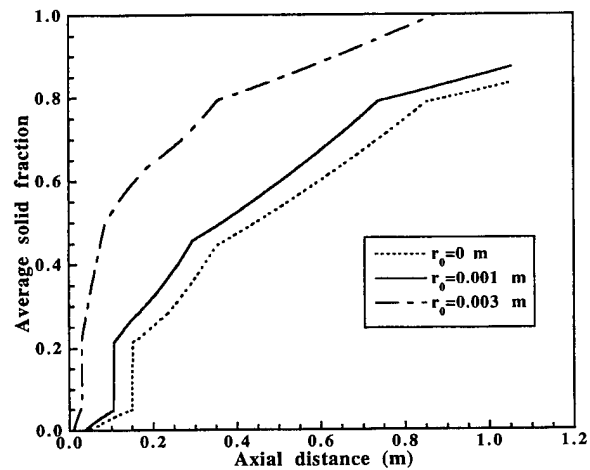
Figure 5-9. The average solid fraction contained in droplets which are initially located at: (a) $r_0=0$ m; (b) $r_0=0.001$ m and (c) $r_0=0.003$ m.

across the spray cone, droplets with smaller r_0 will concentrate in the central region of the substrate whereas droplets with larger r_0 will populate the periphery of the substrate. Therefore, if a substrate were to be inserted across the spray cone, the solid fraction contained in the droplets arriving on the substrate would become higher with increasing radial distance from the center of the substrate. Although there is no direct experimental support to the two dimensional solidification behavior calculated herein, it is experimentally found that in spray deposited materials, such as: Al-Cu-Li-Ag-Mg-Zr alloy Weldalite™ 049 [112], 6061 aluminum alloy [113] and more recently for spray formed γ-TiAl [114], the peripheral region generally contains a higher volume fraction of porosity relative to that present in the central region. Moreover, the available experimental evidence suggests that porosity present in spray deposited material generally develops from interstices formed as droplets impinge on one another, leaving micro-sized,

51

irregular cavities as they overlap [112, 115]. On the basis of this mechanism of porosity formation in spray deposited materials, a high solid fraction in the spray will result in a high volume fraction of porosity in the deposit, since insufficient molten material is available to flow over the deposit to fill pores and interstices. Therefore, the experimental observation that the peripheral region contains a higher volume fraction of porosity relative to that present in the central region implies, to some extent, that the fraction solidified in the periphery is higher than that in the central region.

5.5. Summary

1. The velocity, temperature, cooling rate, flight time and solidification behavior of atomized droplets strongly depends on the initial position, r_0, and the diameter of the droplet, D. In addition, the velocity profiles, temperature histories, cooling rates, flight times and solidification behavior of droplets are also closely related to each other.

2. For identical r_0, i) fine droplets are more readily accelerated or decelerated relative to coarse droplets along both axial and radial directions, ii) fine droplets cool at a higher cooling rate than coarse ones, and iii) fine droplets also solidify at a faster rate relative to coarse ones.

3. For identical D, i) the maximum value of the axial component of droplet velocity decreases with increasing r_0, while the maximum value of the radial component of droplet velocity initially increases and then decreases with increasing r_0, ii) flight time increases with increasing r_0 and iii) the solid fraction at any given axial distance increases with increasing r_0 resulting from the longer flight time for larger r_0.

4. The two dimensional droplet size distribution in the spray cone changes from being heterogeneous to be almost homogeneous with increasing axial flight distance. When the axial distance is smaller than a critical value (approximately 0.75 m for the conditions used in present study), coarse droplets concentrate in the central region of the spray cone, whereas fine droplets populate the periphery. When the axial distance increases beyond

this critical value, the spatial droplet size distribution in the spray cone becomes independent of the radial position.

5. The two dimensional distribution of the fraction solidified in the spray cone is heterogeneous. The fraction solidified at any axial distance increases with increasing radial distance from the spray axis.

CHAPTER 6.

FINITE ELEMENT SIMULATION OF CREEP DEFORMATION
AND RUPTURE OF TITANIUM ALUMINIDES

6.1. Objective

The objectives of this work are: 1) to study the creep behavior of TiAl alloys under tensile creep conditions and to investigate the effect of grain boundary sliding on the overall high temperature deformation and damage processes, and to compare the creep behavior of FL and duplex microstructures; 2) to model and analyze the grain boundary cavitation in fully lamellar ($\alpha_2+\gamma$) titanium aluminide.

6.2. Model Formulation

6.2.1. Creep deformation

The FL and duplex forms of TiAl are modeled using a nonlinear, implicit two dimensional finite element code, NIKE2D [116], developed at Lawrence Livermore National Laboratory. The representative microstructure is taken as a conglomeration of seven equiaxed grains. The duplex structure is modeled by considering a single equiaxed grain of α_2, surrounded by six equiaxed γ grains. Grains of the FL microstructure consist of alternate α_2 laths and packets of γ laths as shown in the Figure 6-1. The orientation of the laths with respect to each other are chosen at random so that the model resembles a realistic microstructure [117, 118].
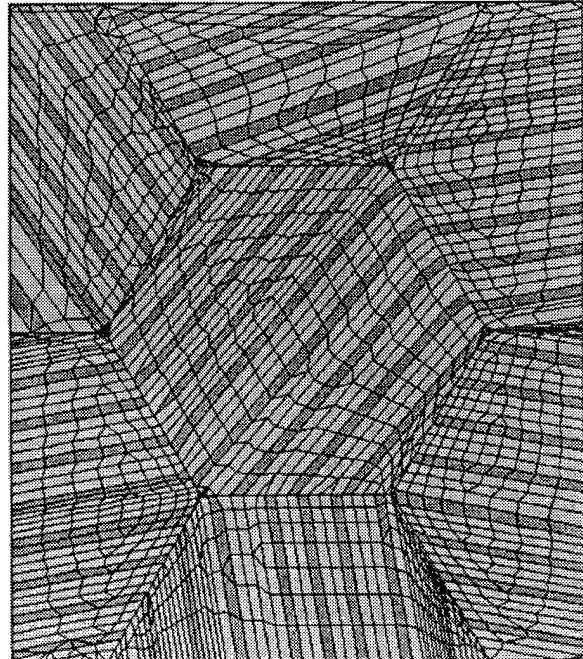
Figure 6-1. FE mesh for the fully lamellar TiAl microstructure. The darker shading indicates the α_2 lamellae.

Two case studies have been performed for both the duplex and FL models. In the first case, the lath and grain boundaries are not allowed to slide. In the second case, all grain boundaries, except those at the continuum boundaries, for both models are capable of frictionless sliding. The results of the present model have been compared with those of a model having fifteen grains and it has been found that the stress distributions are identical. This finding provides justification for using the present smaller model which reduces the computation time without adversely affecting the accuracy of the analysis.

Four noded isoparametric elements are used to model the duplex and FL forms. Sliding elements are used for modeling the grain boundaries. A penalty function approach is used in NIKE2D to implement the contact mechanics formulation that takes into account of the sliding capability of the elements. A 2x2 gauss quadrature is used for numerical integration and the Broyden-Fletcher-Goldfarb-Shanno (BFGS) method [119] is employed as the solution routine for the set of non-linear equations arising out of the finite element formulation.
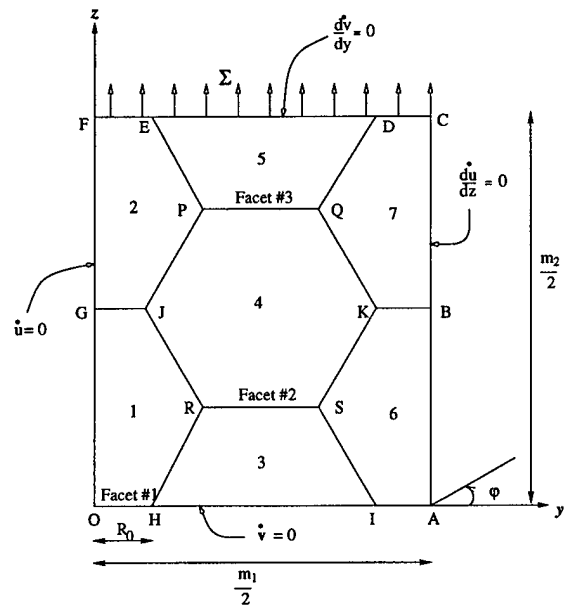
Figure 6-2. Unit cell with grain boundary conditions.

6.2.1.1. _Geometry of the model_

The geometry of the model is shown in Figure 6-2. Both the FL and duplex forms are assumed to have a grain size of 70 mm and have a phase ratio of 1:3 ($\alpha_2 : \gamma$). The orientation of the grains for FL models are given in Tables 6-1 and 6-2:

6.2.1.2. _Boundary conditions_

The boundary conditions of the present models, illustrated in Figure 6-2, are implemented in such a way that the grain boundaries can slide freely without separation. Nodes at the grain boundary triple points are pinned together to meet strain compatibility conditions. Symmetry boundary conditions, u=0

55

and v=0, are applied on sides OF and OA of the cell OACF respectively. This unit cell forms a larger cell when reflected about OA and OF and repetition of this process builds a representative bulk material sample. Nodes on cell boundary AC are constrained to have the same y displacement, u, while nodes on boundary CF are constrained to have the same z displacement, v, at all times. Stress, Σ, is applied on boundary CF. External stress is maintained constant all the time. Plane strain conditions are assumed to exist in the representative continuum [117, 118].

Table 6-1. Angular lath orientation in the grains of the FL-1 model.

Grain no.	Orientation, φ (degrees)
1	10.0
2	125.2
3	99.1
4	49.3
5	99.1
6	10.0
7	125.2

Table 6-2. Angular lath orientation in the grains of the FL-2 model.

Grain no.	Orientation, φ (degrees)
1	10.0
2	125.2
3	99.1
4	49.3
5	19.6
6	169.5
7	8.8

6.2.2. Creep constrained cavitation

At very low tensile stresses, grain boundary diffusion is the dominant mechanism and creep flow is negligible [120]. The volumetric growth rate of equilibrium shaped cavities in this case is given after Rice and Needleman [120] as:

$$\dot{V}_1 = 4\pi \mathcal{D} \frac{\sigma_n - (1 - \zeta)\sigma_s}{\log(1/\zeta) - (3 - \zeta)(1 - \zeta)/2} \tag{6-1}$$

Where, σ_n is the average normal stress on the cavitated grain boundary. The sintering stress, σ_s, is given as $\sigma_s = 2\,\gamma_s\,\sin(\psi)/a$, where γ_s is the surface free energy. The cavity tip angle, ψ, is obtained from the following relation:

$$\mathrm{Cos}(\psi) = \frac{\gamma_b}{2\gamma_s} \tag{6-2}$$

where γ_b is the grain boundary free energy. The area fraction of the cavitated grain boundary, ζ, is given by:

$$\zeta = \mathrm{maximum}\left\{ \left(\frac{a}{b}\right)^2, \left(\frac{a}{a + 1.5L}\right)^2 \right\}$$

where b is the cavity half spacing as shown in Figure 6-3. L is given by:

$$\mathcal{L} = (\mathcal{D}\sigma_e / \dot{\varepsilon}_e^c)^{\frac{1}{3}} \tag{6-3}$$

Here, σ_e is the remote effective Mises stress and ε_e^c is the corresponding effective creep strain rate which are obtained from the power law.

D is defined by:

$$\mathcal{D} = D_B \delta_B \Omega / kT \tag{6-4}$$

where D_B is the grain boundary diffusivity, δ_B is the grain boundary thickness, Omega is the atomic volume and kT is the energy per atom measure of temperature. L denotes the effective radius of the grain boundary diffusion zone around the cavity. Material outside this zone primarily deforms solely by dislocation creep while within this zone grain boundary diffusion from the cavity surface contributes to the deformation.

Applied Stress Direction

Applied Stress Direction
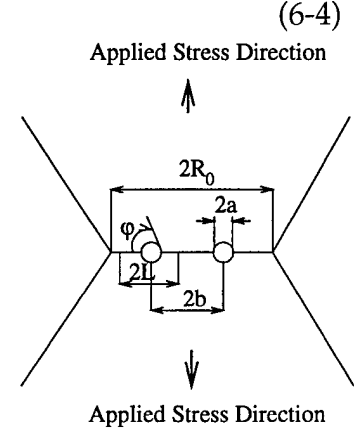
Figure 6-3. Schematic showing grain boundary cavity.

Equations for void growth due to dislocation creep were developed by Budiansky et al. [121] for high triaxial stress conditions. Tvergaard [122] modified these equations to make them applicable for the low triaxiality range and have the form:

$$\dot{V}_2 = {}^{+}_{-}2\pi \dot{\mathcal{E}}_c\, a^3 h(\psi) \left[\alpha_n \left| \frac{\sigma_m}{\sigma_e} \right| + \beta_n \right]^n \quad \text{for} \; {}^{+}_{-}\frac{\sigma_m}{\sigma_e} \geq 1$$

and

$$\dot{V}_2 = 2\pi \dot{\mathcal{E}}_c\, a^3 h(\psi) [\alpha_n + \beta_n]^n \; \frac{\sigma_m}{\sigma_e} \quad \text{for} \; \left| \frac{\sigma_m}{\sigma_e} \right| < 1 \tag{6-5}$$

where $\alpha_n = 3/2n$ and $\beta_n = (n-1)(n+0.4319)/(n^2)$. The parameters σ_m and σ_e are the remote mean stress and Mises stress respectively. The function $h(\psi)$ accounts for the shape of the cavity which is given as:

$$h(\psi) = [(1 + \cos(\psi))^{-1} - \tfrac{1}{2}\cos(\psi)] / \sin(\psi) \tag{6-6}$$

The above equation is based on the assumption that surface diffusion in the voids is sufficiently rapid to retain a spherical cap (equilibrium) shape. Cavities grow as a result of diffusion of surface atoms of the cavity to adjacent grain boundaries. If the void growth is facilitated by creep deformation, the cavities will tend to elongate in the tensile direction. On the other hand, the

cavities tend to become lenticular when grain boundary diffusion is the only mechanism of void growth. It is rapid surface diffusion combined with grain boundary diffusion and dislocation creep that results in equilibrium shaped cavities [120]. The total volumetric cavity growth rate can be determined by summing equations (6-1) and (6-5), thus:

$$\dot{V} = \dot{V}_1 + \dot{V}_2, \text{for} \frac{a}{L} \le 10 \qquad (6\text{-}7)$$

The corresponding rate of change of cavity radius is given as:

$$\dot{a} = \frac{\dot{V}}{4\pi a^2 h(\psi)} \qquad (6\text{-}8)$$

The growth of cavities on grain boundary facets results in the separation of grains by the plating of atoms out onto the grain boundary from the surface of the cavities [123].

The average separation delta can be expressed in terms of cavity volume V and cavity half spacing b as $\delta = V/\pi b^2$. Therefore, the rate of separation of the grains, δ, is [122]:

$$\dot{\delta} = \frac{\dot{V}}{\pi b^2} - \frac{2V\dot{b}}{\pi b^3} \qquad (6\text{-}9)$$

where V is given by equation (6-7). The contribution of the second term in equation (6-9) becomes important when finite strains in the zones close to the cavities result in significant changes in the void spacing. The rate of change of void spacing, b, can be correlated with the true strain rate, ε_p, in the grain boundary plane under plane strain conditions as in [124]:

$$\frac{\dot{b}}{b} = \frac{1}{2}\dot{\varepsilon}_p \qquad (6\text{-}10)$$

We assume that all the cavities along a facet are of same size and they are spaced equally. In this case, the distinct distribution of cavities at grain boundaries can be represented by a uniform value of δ [124].

6.2.2.1. *Method of analysis*
It is assumed that the spatial distribution of the cavitating facets follows a periodic order so that we can confine our analysis to a unit cell. Only transverse grain boundaries with respect to the direction of externally applied stresses are assumed to cavitate. Figure 6-2 shows one quarter of the unit cell with boundary conditions. It can be seen from this figure that the dimensions

58

of the unit cell are specified in terms of the number of grains in the y direction, m_1, the number of grains in the z direction m_2 and the initial radius of the grain boundary facets R_0.

As in the creep deformation models, finite element techniques were used here also to model creep constrained cavitation in the fully lamellar TiAl. All the analyses are performed under plane strain boundary conditions. Finite element code, NIKE2D [116] and its associated pre- and post-processors were used to analyze all of the cases presented here. Grain boundary sliding under the action of externally applied stresses was simulated using slide lines along the grain boundaries. Details on the use of slide lines in FE models can be found elsewhere [116, 125]. In all of the analyses performed here, it is assumed that grain boundary sliding takes place freely. This assumption should be particularly valid for intermetallic materials, such as TiAl alloys, which have a relatively low dislocation mobility under the conditions considered making boundary sliding more prevalent as a deformation mechanism [126, 127]. Furthermore, Hayes and Martin [9] have observed grain boundary triple point wedge cracks in single phase gamma TiAl which suggest that the friction stress against grain boundary sliding in this material is relatively low under creep conditions.

It has also been proposed that certain γ/γ lath boundaries may slide by the dissociation of superdislocations in fully lamellar TiAl [128]. Although experimental evidence has been reported for this mechanism during plastic deformation at ambient temperature, both theoretical [61] and experimental [43] studies have shown that with the possible exception of the earliest stages of primary creep, this mechanism is not operative under typical creep conditions. Accordingly, lath boundary sliding is not considered in the present models.

The boundary conditions at the cavitating grain boundary are modeled after Tvergaard [122]. In each time increment, the facet OH was subjected to an incremental displacement δ given as:

$$\delta = \frac{\dot{\delta}}{2}\Delta t \qquad (6\text{-}11)$$

where δ is given by equation (6-11) and δ_t is the time increment. Stresses σ_m, σ_e and σ_n used in equations (6-1) and (6-5) and the true strain rate ε_p used in evaluating equation (6-10) are obtained directly from the elements at the center of the cavitating facet at each time step. The center of the cavitating facet is chosen as this sampling point because the influence of the singularity at the grain boundary triple points is minimal there and thus the stresses and strains are more representative of the overall stress on the boundary. For fully lamellar models, this position is also within a γ lath which is under a higher stress compared to neighboring α_2 laths since α_2 is weaker than γ under the present creep conditions [61]. The length of the time steps during the initial period of cavitation is kept very small so that numerical stability is maintained. Normal stresses, σ_n, at the cavitating grain boundary elements are evaluated at each time step to assure that they are greater than zero. Whenever, the normal stress reaches zero in any element at a cavitating boundary, that particular element edge is treated as a free surface from that time step onward.

6.2.2.2. *Modeling TiAl microstructures*

Models of the dual phase equiaxed microstructure that has the same phase ratio (α_2/γ) as that in the fully lamellar microstructure have been developed to compare the latter structure with the former.

Two forms of dual phase $\alpha_2+\gamma$ microstructures are analyzed here. The first, DX-1, is modeled by considering a unit cell which has equiaxed grains of α_2 phase surrounded by six equiaxed grains of gamma phase. Thus the mesh used here is the same as that used in the single phase model except that the central grain, 4, is composed of α_2 phase. The boundary conditions are identical to those in the previous case. The second model of the dual phase structure, DX-2, is configured as grains 3 and 5 of α_2 phase and all other grains, including grain 4, of γ phase. Other than this difference, the mesh used for the DX-2 model is the same as that used for the DX-1 model.

Furthermore, it has been proposed that serrated grain boundaries inhibit grain boundary sliding during creep deformation [48, 61, 129, 130]. Considering this hypothesis, models of fully lamellar TiAl intermetallics are analyzed in the present work for both the case of cavitation with the presence

60

of grain boundary sliding and the case of cavitation without the influence of grain boundary sliding. We refer to the mesh, used in creep deformation studies as either FL-1 or FL-2 depending on the loading and boundary conditions. For the FL-1 models, tensile stress Σ is applied at the face CF of the unit cell OACF and all other boundary conditions are the same as for the single phase and dual phase models. For the FL-2 models, tensile stress Σ is applied at the face OA and the boundaries OF and CF are constrained to have zero displacements along y and z directions respectively. The nodes at boundaries OA are constrained to move together along the z direction and the nodes at boundaries AC are constrained to move together along the y direction at all time. As before, grain boundary triple points are pinned together to have the same y and z displacements at all the time. The cavitating facet is OH in all models except for the FL-2 models in which it is the facet EF.

The last stages of cavity coalescence involves rapid tearing of the ligaments between the cavities and it is reasonable to assume that this process begins to occur once the cavitation damage, ω, reaches about 0.6 [131]. Accordingly, a critical level of cavitation is assumed to occur when $\omega=0.6$ in all of the present analyses. In all of the analyses, it is assumed that the cavities nucleate upon loading and there is no nucleation of any new cavities during the rest of the simulation. The following initial values are assumed, $(a/b)_0=0.1$ and $(b_0/R_0)=0.4$. It should be noted that the above assumptions are uniformly made for all of the present models. Riedel [131] observed that the initial size of the cavities in metals and alloys is typically 0.2-1 μm. Accordingly, we assume a representative initial value of a to be 0.7 μm. We note that the model results are relatively insensitive to the initial cavity radius as long as it is within a range of reasonable values. For most metals and alloys, the grain boundary surface energy, γ_s is between 1-2 J/m^2 [132]. We estimate $\gamma_s=\mu b\backslash 10$ =1.69 J/m^2, where b is the burgers vector and μ is the shear modulus, following the work of Chu and Thompson [132]. Sintering stress, σ_s, is found to be 4.54 MPa for a cavity radius of a = 0.7 μm which is negligibly small compared to the externally applied stress of 120 MPa. Accordingly, σ_s is taken to be zero in the present models. We also assume that the properties γ_s and ψ are the same at all the grain boundaries of the single phase gamma, dual phase equiaxed ($\gamma+\alpha_2$), and fully lamellar ($\gamma+\alpha_2$) TiAl models. Reference

61

time, t_E is calculated for the fully lamellar alloy and used to normalize the time for all models. In the present work, grain boundary diffusivity D_B is assumed to have the same value for the single phase models and the γ/γ grain boundaries in the dual phase equiaxed models. Since, D_B of the gamma phase is higher than that for the α_2 phase [133, 134], we have assumed that the D_B of the fully lamellar alloy is approximately equal to that for the gamma phase. Grain boundary properties of gamma TiAl are given in Table 6-3. Although the above assumptions could result in significant errors in predicting absolute rupture time, they appear to be sufficient for an accurate comparison of the susceptibility of different phase morphologies to grain boundary cavitation.

Table 6-3. Grain boundary properties

Property	Value
D_B	$7.5825 \times 10^{-7} m^2/s$ [133]
δ_B	$0.001 \ \mu m$ [133]
ψ	$70°$ [131]
Ω	$4.62 \times 10^{-30} m^3$ [133]

6.3. Results and Discussion

6.3.1. Creep deformation

Normal stress (σ_z) contours for the homogeneous model are plotted in Figure 6-4. It can be seen that the stress distribution is identical from grain to grain in the unit cell. As expected, regions near grain boundary triple points correspond to stress concentrations. It had been shown analytically that grain boundary triple points have a singularity in stress when grain boundary sliding is accommodated by power law creep of the grain matrix. In the present analysis, the maximum stress value at the grain boundary triple point is of the order of two times the externally applied stress. However, this error will have an insignificant effect in the results of the present analysis since the singularity is confined to a very small volume.

Figure 6-5 shows a plot of normal stress contour in the dual phase model in absence of grain boundary sliding (GBS). It is evident from this figure that the central grain, which is of α_2-Ti_3Al phase, supports a low level of stress compared to that for the adjacent γ TiAl grains. Grain boundary triple points
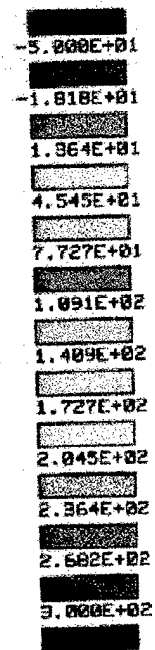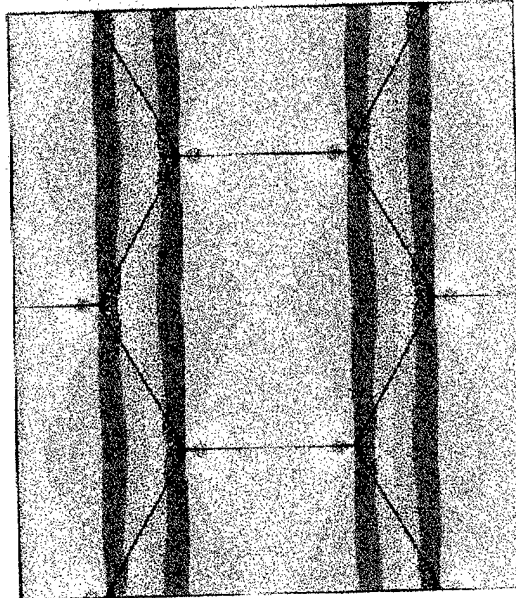
fringes of z stress

Figure 6-4. Axial stress (σ_{zz}) distribution in single phase γ TiAl in the presence of grain boundary sliding. The fringe levels defined on the right side are in units of MPa.

fringes of z stress

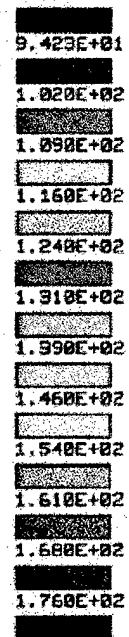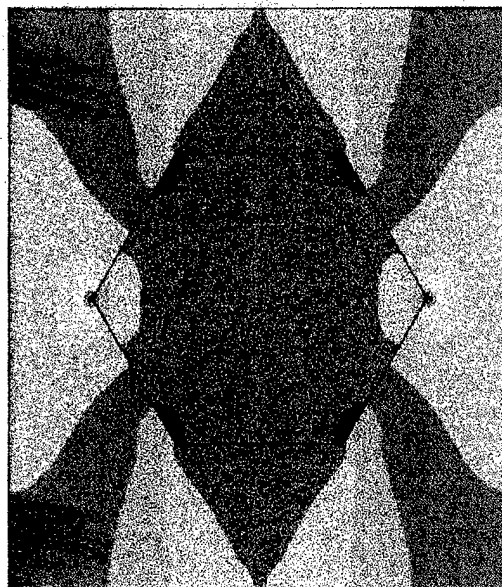**Figure 6-5.** Axial stress (σ_{zz}) distribution in dual phase $\alpha_2+\gamma$ TiAl without grain boundary sliding. The fringe levels defined on the right side are in units of MPa.

J and K are found to be in regions of high stress concentrations. However, the four other triple points (R, S, Q and P) in the unit cell are relatively free from stress concentrations. Since the γ phase has a greater creep strength that the α_2 phase under present conditions, load is shed from the α_2 grain to adjacent γ grains which results in the low level of σ_z at the transverse grain (α_2/γ) boundaries. By contrast, transverse grain boundaries between two γ/γ grains (GJ and KB) are subjected to a high level of σ_z.

The features of the σ_z fringe pattern for the dual phase model in presence of GBS are similar to that of Figure 6-4, except that the stress distribution inside the central grain (α_2 phase) is different from that in adjoining grains (γ phase). Moreover, grain boundary triple points J and K have a higher level of stress concentration compared to other triple points R, S, Q and P.

The normal stress fringe pattern for the FL-1 model without GBS is illustrated in Figure 6-6. It is interesting to note the stress distribution in the α_2 laths in this figure. Those α_2 lamellae which are inclined at an angle close to transverse direction are found to have a σ_z level almost identical to the adjacent γ laths. As the angle of inclination increases, stress in α_2 laths is redistributed and, as a result, the adjacent γ laths are under a higher stress level. A similar stress pattern was obtained in FL-2 model without GBS.

The σ_z distribution in the FL-1 model with grain boundary sliding is illustrated in Figure 6-7. The stress distribution is nonuniform throughout the structure. It is not evident from this figure that the angular orientation of the γ and α_2 phase boundaries have an effort on the stress distribution. However, abrupt changes in stress contours inside the grains result from the alternate change of phases. As in the case of the single phase or dual phase equiaxed models, the transverse grain boundaries are observed to be the most heavily stressed regions. A similar stress pattern was obtained for the FL-2 model.

The normal stress distribution in FL-1 model having γ/γ lamellar boundary sliding is illustrated in Figure 6-8. Grain boundary triple points P, Q, K and B are found to be at regions of stress concentration. It can also be seen in Figure 6-8 that a few regions along grain boundaries RJ, JP, PQ, QD and QK have

time=1.00000E+01
dsf =1.00000E+00

fringes of z stress

minval= 8.468E+01
maxval= 1.624E+02
fringe levels

9.066E+01
9.664E+01
1.030E+02
1.090E+02
1.150E+02
1.210E+02
1.270E+02
1.330E+02
1.390E+02
1.440E+02
1.500E+02
1.560E+02
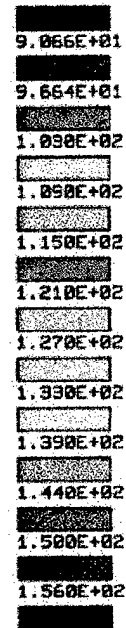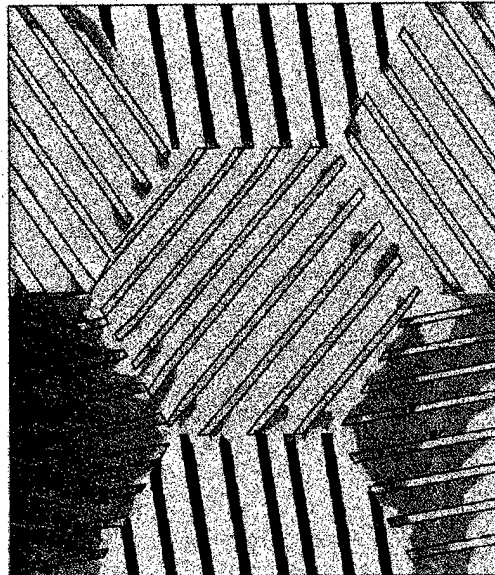
Figure 6-6. Axial stress (σ_{zz}) distribution in fully lamellar TiAl (FL-1) without grain boundary sliding. The fringe levels defined on the right side of this figure are in units in MPa.

time=1.00000E+01
dsf =1.00000E+00

fringes of z stress

minval=-1.370E+02
maxval= 3.828E+02
fringe levels

-5.000E+01
-1.818E+01
1.364E+01
4.545E+01
7.727E+01
1.091E+02
1.409E+02
1.727E+02
2.045E+02
2.364E+02
2.682E+02
3.000E+02

Figure 6-7. Axial stress (σ_{zz}) distribution in fully lamellar TiAl (FL-1) in the presence of grain boundary sliding. The fringe levels defined on the right side of this figure are in units in MPa.

65

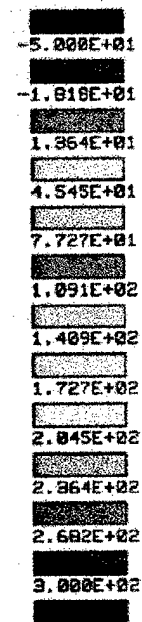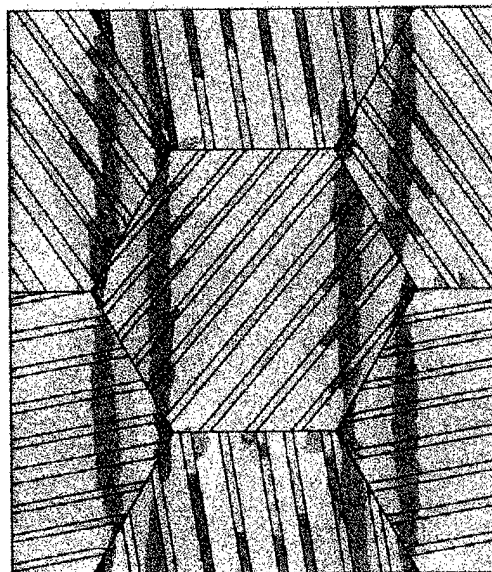stress concentrations which resulted from the slide lines (γ/γ phase boundaries) that are constrained at these grain boundaries. It appears from this figure that the stress distribution in each grain is affected by the orientation of the laths. Grains 1 and 6 have a relatively uniform σ_z distribution which results from the near transverse lath orientation in these two grains.

For the normal stress distribution in FL-2 model having γ/γ lamellar boundary sliding, fewer stress concentrations result for this model compared to that for the FL-1 model. It appears that the asymmetric orientation of laths allows for greater stress relaxation where the sliding phase boundaries are constrained, particularly along grain boundary PQ.

A comparison of overall strain rate as a function of strain for the different models is shown in Figure 6-9. It is evident from this figure that the single phase model without GBS exhibits the lowest minimum strain rate. On the other hand, FL-1 with grain boundary sliding exhibits the highest minimum creep rate. We note from this figure that the effect of grain boundary sliding is very similar in nature from one microstructure to another. It is also evident from this figure that the models exhibit a strain softening behavior. This softening behavior is a result of the 8% increase in the stress throughout the deformation process.

Figure 6-10 shows the minimum strain rates of FL-1 and FL-2 models with γ/γ lath boundary sliding. It can be seen in this figure that the minimum strain rate is higher for the FL-1 model by a factor of 4 as compared to that in FL-2 model. A separate calculation based on a shear crack model and subsequently modified for a random microstructure was performed as an alternate method to estimate the effect of γ/γ phase boundary sliding in these two models. In spite of some sources of error in applying the shear crack model to phase boundary sliding, we find that the trend in the results obtained using a shear crack model is similar to that obtained in present modeling using FEM. We note that this shear crack approximation is good for a rough estimation of phase boundary sliding but a detailed finite element analysis must be carried out in order to gain more insight into the problem.

time=1.00000E+01
dsf =1.00000E+00

fringes of z stress

minval=-4.958E+02
maxval= 6.302E+02
fringe levels

-5.000E+01
-1.818E+01
1.364E+01
4.545E+01
7.727E+01
1.091E+02
1.409E+02
1.727E+02
2.045E+02
2.364E+02
2.682E+02
3.000E+02
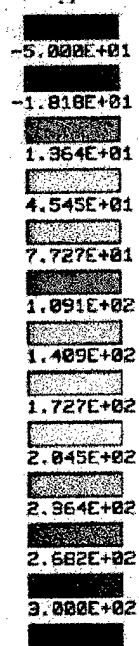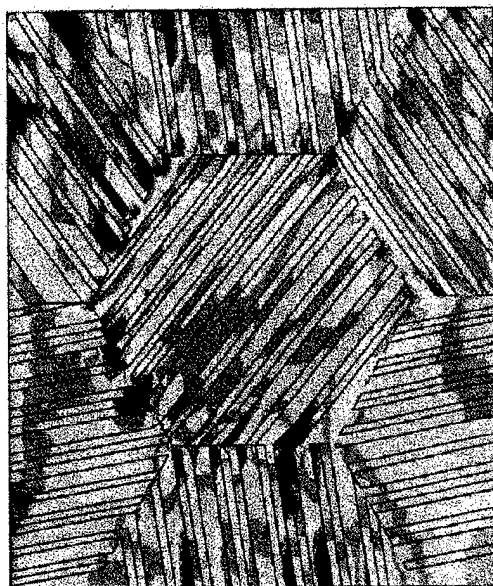
Figure 6-8. Axial stress (σ_{zz}) distribution in fully lamellar TiAl (FL-1) in the presence of γ/γ phase boundary sliding. The fringe levels defined on the right side of this figure are in units in MPa.
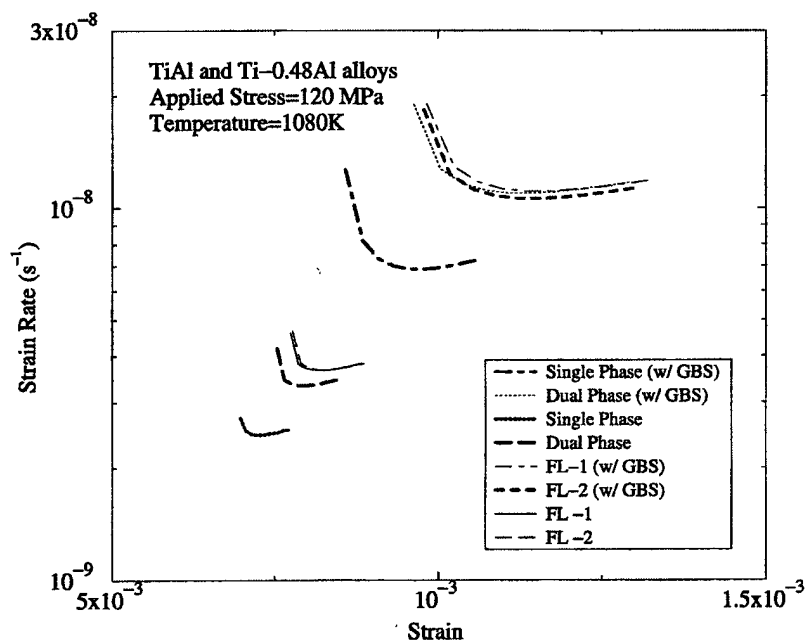
Figure 6-9. Comparison of overall strain rate vs. strain for different TiAl microstructures. Models which include grain boundary sliding are indicated by w/GBS.

67
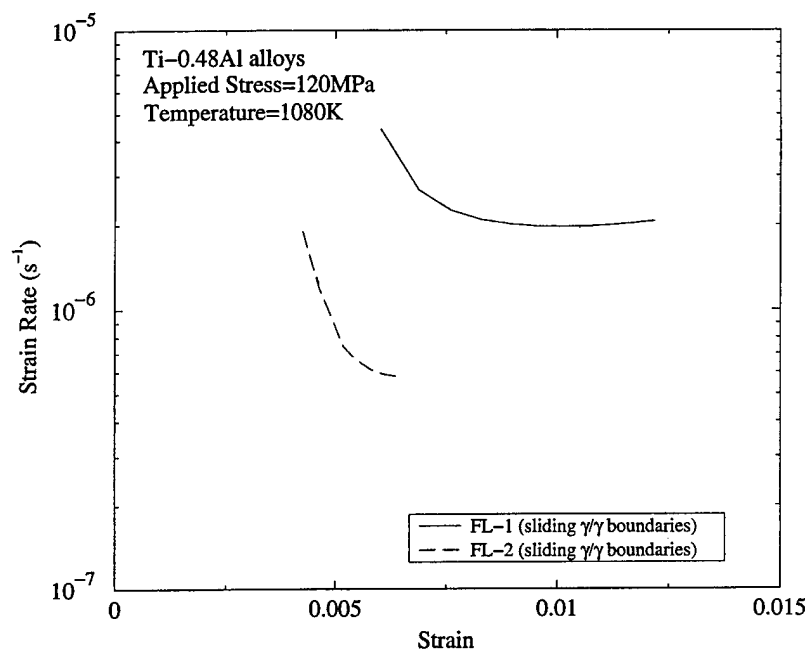
Figure 6-10. Comparison of overall strain rate vs. strain in FL TiAl for lath boundary sliding in the absence of grain boundary sliding.
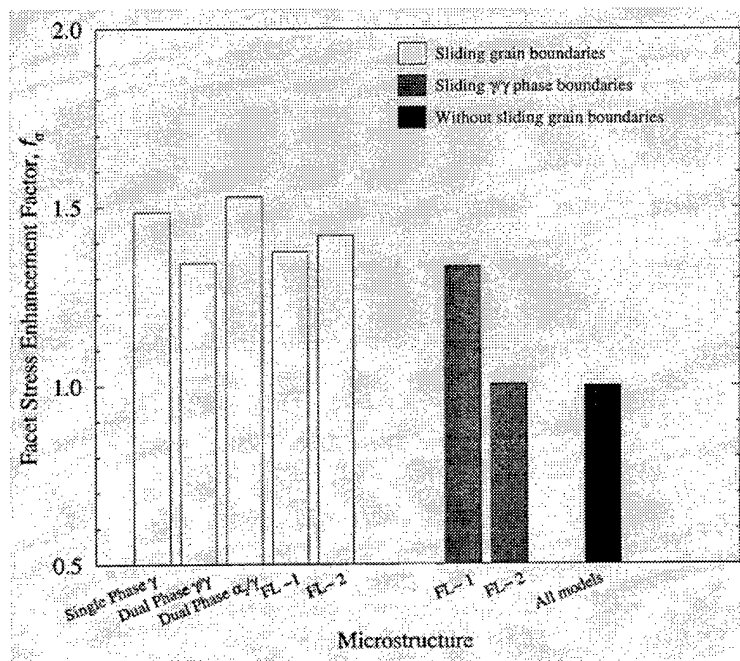
Figure 6-11. Local stress enhancement factor, f_σ, for different TiAl microstructures.

Facet stress enhancement factors were calculated for all the models and are compared in Figure 6-11. Anderson and Rice used a self consistent approach to study the effect of constraints on diffusive creep cavity growth for f.c.c. metals. They found a value of facet stress enhancement factor, $f_\sigma = 1.67$ for $n = 5$ for 3D Wagner-Seitz cells when hexagonal facets are normal to externally applied stress. Rice has shown from 2D analysis that f_σ for a homogeneous single material with freely sliding grain boundaries is approximately 1.5. We obtained $f_\sigma = 1.49$ for the single phase model, as shown in Figure 6-11.

The single phase model exhibits a greater value for f_σ, than that obtained at the γ/γ grain boundaries of dual phase equiaxed model. However, f_σ at the α_2/γ grain boundaries of the dual phase model is greater than the facet stress enhancement factor of single phase model. Grain boundary sliding in the FL-1 and FL-2 models yields a lower value of f_σ when compared to single phase and dual phase equiaxed models. We observe that the minimum strain rate is enhanced due to grain boundary sliding in the single phase and dual phase equiaxed structures by factors of 2.8 and 3.3 respectively. On average, the stress in the γ grains is higher than that supported by the α_2 grains. In the single phase structure, the mean stress in the γ grains is lower resulting in a minimum strain rate as compared to the dual equiaxed model by a factor of 1.6. This observation is consistent with the experimental findings that under similar creep conditions, a duplex TiAl alloy indeed exhibits a higher creep strain rate than that for the corresponding single phase γ microstructure by a factor of 1.83.

Of all of the present forms of TiAl considered in a present work, the FL microstructure was found experimentally to possess the highest creep strength and fracture toughness. This finding can only be consistent with the present model results if grain boundary sliding is inhibited in the fully lamellar microstructure while relatively easy in the equiaxed microstructures. Two different types of lamellar grain boundaries had been found in FL TiAl alloy. One with a composition of Ti- 44%, is found to have serrated grain boundaries. It was observed that the alloy having serrated grain boundaries exhibits a lower creep strain rate compared to the alloy with straight grain boundaries by a factor of 8 and concluded that the serrated nature of the grain boundary is the primary reason for higher creep strength. This is in accord

with the present FE results given that the straight grain boundaries undergo sliding during creep but the serrated grain boundaries are generally prevented from sliding. A comparison of Figures 6-9 and 6-10 indicates that the FL alloys would exhibit an overall strain rate in presence of γ/γ lath boundary sliding that is about two orders of magnitude greater than that for the equiaxed microstructures in the presence of grain boundary sliding. This result appears unrealistic as the overall strain rates obtained from the lath boundary sliding models are more than hundred times greater than the typical minimum creep strain rates observed experimentally for LF TiAl alloys under similar temperature and stress conditions. Moreover, it was observed experimentally that the density of superdislocations <101] in γ lamella do not change during the course of creep deformation. Therefore, it was concluded that the superdislocations do not favor any extra deformation mode along the γ/γ laths. Thus it is doubtful that many superdislocations are able to reach the lath boundaries to dissociate under the creep conditions imposed. Based on this data and our model results, it is unlikely that γ/γ phase boundary sliding occurs to any great degree during the creep deformation of lamellar TiAl alloys.

6.3.2. Creep constrained cavitation

6.3.2.1. *Cavitation in fully lamellar and dual phase equiaxed models*

Figure 6-12 shows the normalized axial stress distribution in the fully lamellar model (FL-1) in the absence of GBS. It is observed that α_2 laths that are more closely aligned with the applied stress direction redistribute more stress to the adjacent gamma laths. This results in inhomogeneous stress distributions along grain boundaries RS and PQ. However, the stress level discontinuities are more extreme at boundary RS than those at PQ. This is apparently due to the more isostress orientation of the lamellae in grain 5 as well as the proximity of RS to the cavitating facet.

The distribution of normalized axial stress in FL-1 model in the presence of GBS is illustrated in Figure 6-13. It is evident from this figure that the transverse grain boundaries RS and KB are heavily stressed regions in the microstructure. Cavitation at grain boundary OH again redistributes stress from grain 1 to adjacent grains. However, a high level of stress at grain boundary RS ensues as a result of the load shedding of the α_2 laths at this

70

Fringes of z stress   fringe levels
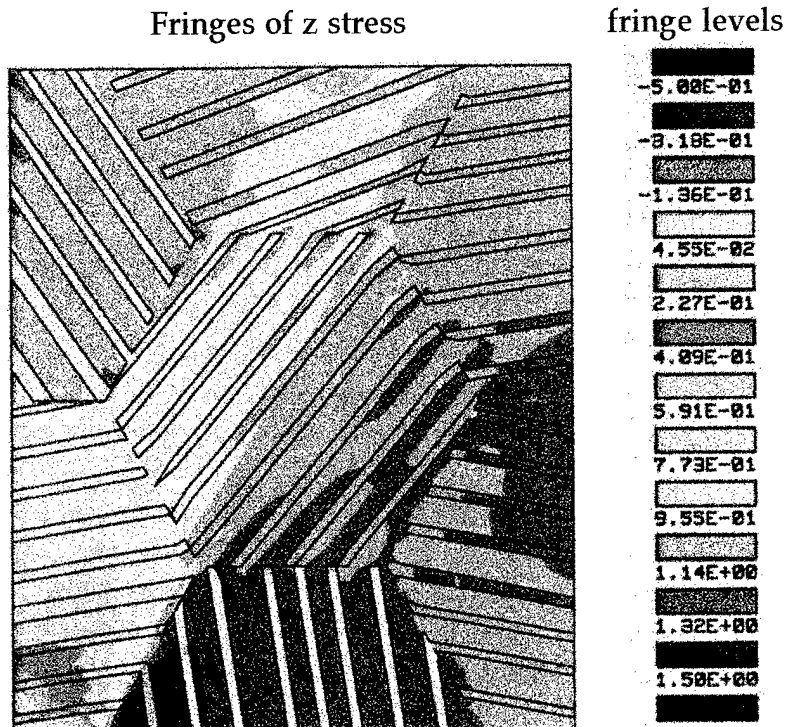
Figure 6-12. Normalized axial stress (σ_z/Σ) distribution in the fully lamellar TiAl (FL-1) during creep cavitation at central grain boundary OH without GBS. It should be noted that the fringe levels in this figure are different from those in previous figures.

Fringes of z stress   fringe levels
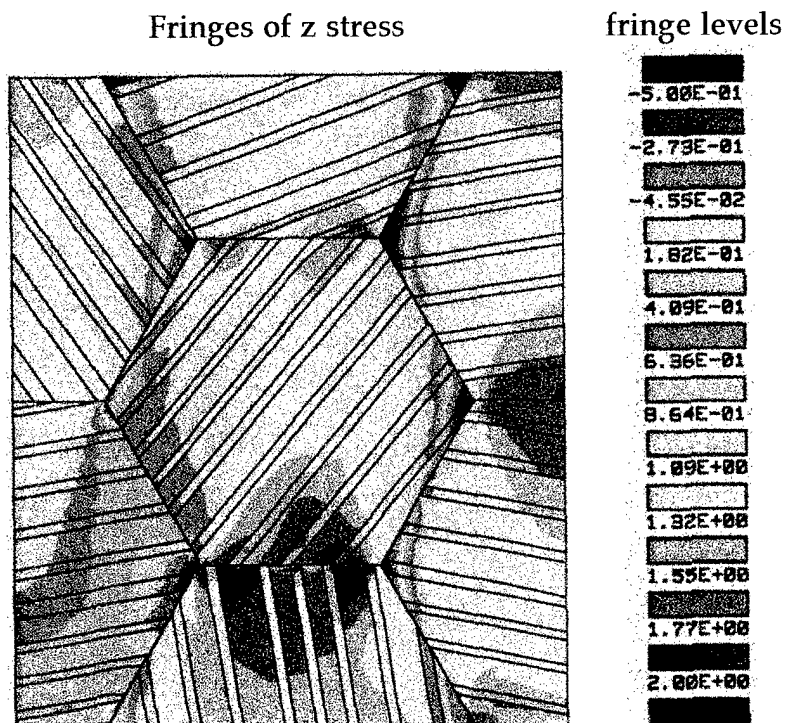
Figure 6-13. Normalized axial stress (σ_z/Σ) distribution in the fully lamellar TiAl (FL-1) during creep cavitation at central grain boundary OH in the presence of GBS.

grain boundary and due to the sliding of the inclined grain boundaries. It is interesting to note that the transverse grain boundary KB is stressed to a higher level than either boundary GJ or PQ although these boundaries have lath orientations that are less characteristic of an isostress arrangement. It appears that the higher stress at boundary KB is due to the fact that it lies in the path of the highest stresses which arise from the growth of the cavities at grain boundary OH.

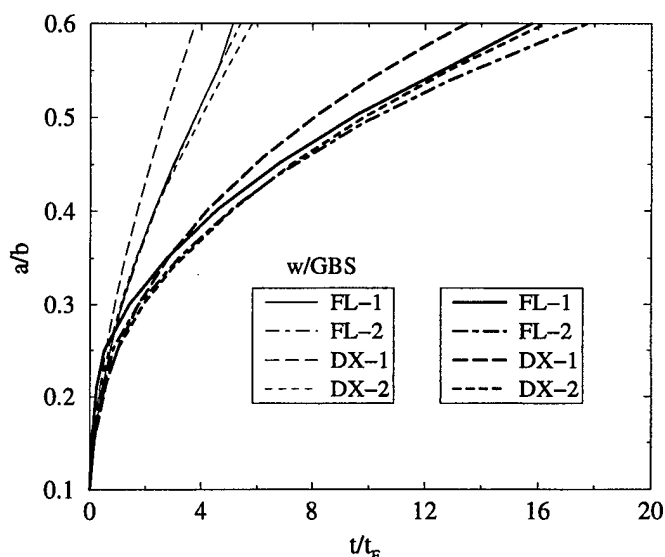The development of creep cavitation damage $\omega = a/b$ as a function of normalized time t/t_E is illustrated in Figure 6-14, for the present models. It is evident from this figure that grain boundary sliding substantially reduces the cavity coalescence time for all the microstructures considered.

The two fully lamellar models, FL-1 and FL-2

Figure 6-14. Plot of creep damage at the facet #1 in FL and DX models versus normalized time.

yielded identical results for cavitation in the presence of GBS. This similarity indicates that the effect of lamellae orientation on creep cavitation is not as pronounced in the presence of grain boundary sliding. In the absence of GBS, the FL-2 model is found to be stronger than the FL-1 model. The important point here is that a difference in cavity coalescence time for the two FL models is only evident when GBS is suppressed. This is likely the case for the FL microstructure which normally exhibits serrated grain boundaries. The present results indicate that cavities at a grain boundary with intersecting lath orientations which are isostress in nature will tend to grow slower compared to the case where the intersecting lath orientations are closer to an isostrain orientation. Lath orientations that are nearly parallel to the applied stress direction in the zone adjacent to the cavitating grain boundary result in load

shedding from α_2 laths to γ laths which then produces less constraint on the cavitation process.

6.3.2.2. *Effect of lamella thickness*

Effect of lath width on creep constrained grain boundary cavitation in the fully lamellar TiAl intermetallics was also investigated. Two models FL-1b and FL-2b having $l/d=0.058$ are analyzed here. l is the lath thickness and d is the grain size with $d=4R_0$. The FL-1 and FL-2 models have $l/d=0.029$. The meshes used for FL-1b and FL-2b models are identical with those used for FL-1 and FL-2 models except that the laths have twice the thickness.

Figure 6-15 shows the comparative growth of creep damage in the fully lamellar models FL-1, FL-2, FL-1b and FL-2b. Cavity growth as a function of normalized time t/t_E is calculated at facet OH in models FL-1 and FL-1b and at facet EF for FL-2 and FL-2b models. It is evident from this figure that the development of cavitation damage for all the models is practically identical in the
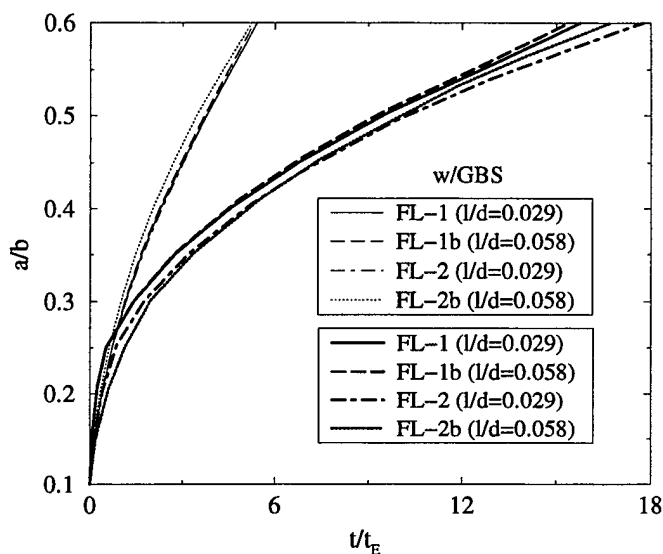
Figure 6-15. Plot of creep damage at the facet #1 in FL-1 and FL-2 models versus normalized time.

presence of the GBS. This is due to the fact that when grain boundary sliding takes place, the regions around the grain boundaries carry the bulk of the load and deform heavily which overrides the effect the laths have on stress redistribution in the adjoining grains. In the absence of grain boundary sliding, the thicker lath width resulted in faster cavity growth rates for both the FL models. However, these differences in cavity growth rates are small and for all practical purposes may be deemed negligible. It is also evident from this figure that the cavity growth rate is consistently dependent on the lamella orientation in the absence of grain boundary sliding. Laths in the regions immediately adjacent to the cavitating facets in the FL-2 and FL-2b

73

models are of isostress orientation providing more constraint on cavitation as compared to that for the FL-1 and FL-1b models.

It appears from experimental observations that a thicker lath width can result in a lower degree of lamella interlocking at the grain boundaries [5]. Therefore, grain boundary sliding mobility could also be higher in a microstructure having thicker lath width. It follows that, the effect of thicker lath width on grain boundary cavitation could be detrimental due to more stress redistribution from sliding grain boundaries. A good understanding of the relationship between lath thickness and grain boundary sliding mobility in TiAl requires further study.

6.3.2.3. _Effect of interaction between cavitating facets_

Figure 6-16 shows the development of creep damage, omega due to the interaction between the cavitating facets 1 and 2 as a function of normalized time, t/t_E for the fully lamellar models, FL-1 and FL-2. As in the previous figure, GBS results in a significant reduction in rupture time for the present FL models. It is evident here that the growth of cavities at the two facets are nearly identical in all the models. Cavitation damage in one facet redistributes stresses to its adjacent transverse grain boundaries. Thus, a positive interaction between the cavitating facets 1 and 2 takes place which results in nearly identical cavity growth in both the facets. As in the previous section, the FL-2 model is found to be more resistant to cavity growth than the FL-1 model in the absence of GBS. The difference in rupture time for all the models with GBS is not very large and hence can be considered as identical for all practical purposes.

Figure 6-16. Plot of creep damage at the facets #1 and #2 in FL-1 and FL-2 models versus normalized time.

74

The creep damage due to the interaction between the cavitating facets 1 and 3 in the FL models are plotted as a function of normalized time, t/t_E, in Figure 6-17.

6.3.2.4. _Effect of cavitating facet density_

Mesh used for studying the effect of lower cavitating facet density in FL TiAl is shown in Figure 6-18. The boundary conditions used for this bigger unit cell are similar to those applied to the smaller unit cell OACF.
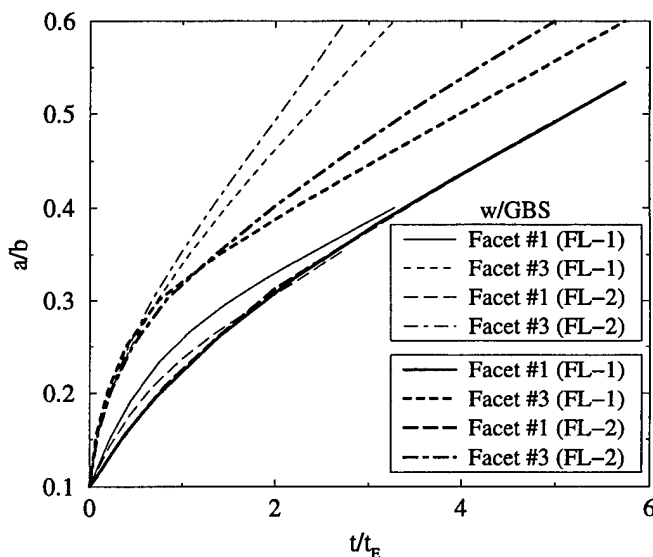
Figure 6-17. Plot of creep damage at the facets #1 and #3 in FL-1 and FL-2 models versus normalized time.

The effect of cavitating facet density on creep cavitation damage is shown in Figure 6-19. The FL-1 model with higher cavitating facet density yielded faster cavity growth for both with and without the GBS. The FL-1 model with $\rho=0.03186$ exhibited rapid cavitation damage growth in the absence of GBS from the very onset of cavitation. However, the two FL-1 models with $\rho=0.01416$ and $\rho=0.03186$ yielded identical damage growth until the cavities reach a critical stage at $\omega=0.42$ in the presence of GBS. From this time onward, the FL-1 model with $\rho=0.03186$ yielded much faster damage growth till the cavities coalesce. It should be noted here that an increase of ρ by a factor of 2.25 only reduces the rupture time by a
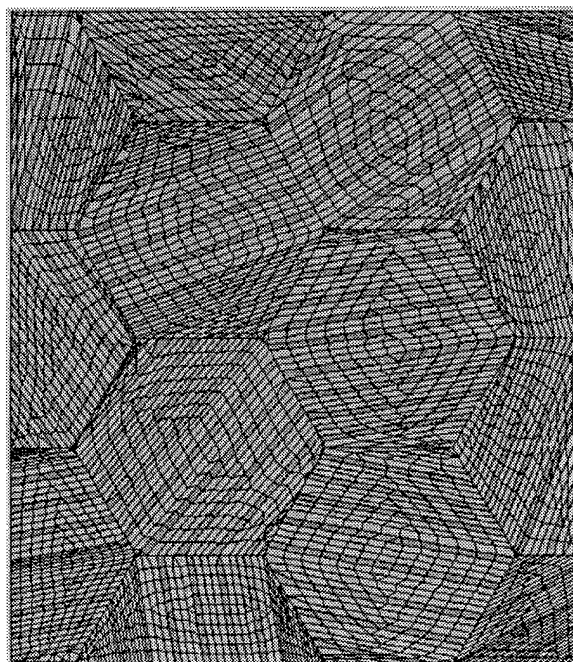
Figure 6-18. FE mesh for the FL-1 and FL-2 models having r=0.01416. The α_2 laths are indicated by darker shading.

75

factor of 1.28 and 1.23 for the FL-1 model with and without the GBS respectively.

6.4. Conclusion

The following conclusions are drawn from the present study of creep deformation and cavitation in fully lamellar and dual phase equiaxed ($\alpha_2+\gamma$) TiAl microstructures.

It is found that inherent creep strength of the fully lamellar TiAl is due to the nature of its serrated grain boundaries which inhibits boundary sliding during creep deformation. It is also found that the γ/γ boundary sliding does not take place to a great extent during the creep deformation. These findings are consistent with the experimental observations published in the literature.
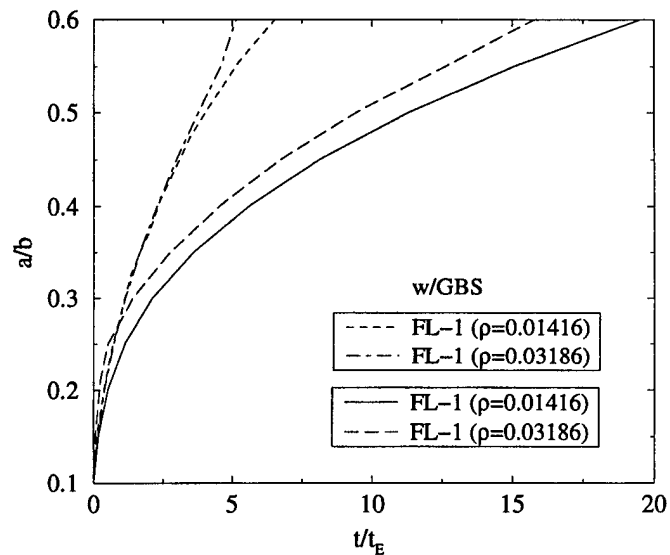
Figure 6-19. Effect of cavitating facet density on creep damage of the fully lamellar models versus normalized time.

The present model results indicate that the dual phase equiaxed microstructure exhibits the greatest resistance against cavitation when cavity growth occurs at the γ/γ grain boundary adjacent to the α_2 grain. This occurs in the presence of grain boundary sliding. Conversely, this microstructure is the most susceptible to cavitation damage when cavitation occurs at an inclined angle to a neighboring α_2 grain. The effect of lamellae orientation on creep cavitation damage in the fully lamellar microstructures is found to be insignificant in the presence of grain boundary sliding. However, isostress orientation of laths in the grains adjacent to the cavitating grain boundary is found to delay the cavity growth and thereby increases the rupture life. However, in real microstructures with random lamellae orientation, this

beneficial effect may not be seen. It has been observed in the present study that the lamellae width does not affect the cavity growth process as long as the grain boundary mobility is the same in all the different fully lamellar microstructures. The effect of interaction between the cavitating facets in the fully lamellar models is generally positive when cavitating boundaries are on neighboring grains. However, a negative interaction effect can take place for certain cavitating facet configuration.

Based on the present results, the relatively long rupture times observed experimentally for fully lamellar TiAl may be primarily attributed to the suppression of grain boundary sliding in this microstructure.

REFERENCES

1. M. H. Yoo, S. L. Sass, C. L. Fu, M. J. Mills, D. M. Dimiduk and E. P. George, *Acta Metall. Mater.*, Vol. 41 (1993) 987.

2. S. L. Semiatin, N. Frey, S. M. El-Soudani and J. D. Bryant, *Metall. Trans.*, Vol. 23A (1992) 1719.

3. S. L. Semiatin and P. A. McQuay, *Metall. Trans.*, Vol. 23A (1992) 149.

4. R. Nekkanti, P. A. Mcquay and S. L. Semiatin, *Scripta Metall. Mater.*, Vol. 26 (1992) 1089.

5. Y. W. Kim, *JOM*, Vol. 46 (1994) 30.

6. K. S. Chan and Y. M. Kim, *Acta Metall. Mater.*, Vol. 43 (1995) 439.

7. K. S. Chan and D. S. Shih, *Metall.&Mater. Trans.*, Vol. 28A (1997) 79.

8. M. Es-Souni, A. Bartels and R. Wagner, *Acta Metall. Mater.*, Vol. 43 (1995) 153.

9. R. W. Hayes and P. L. Martin, *Acta Metall.*, Vol. 43 (1995) 2761.

10. J. Wolfenstine and G. Gonzalez-Doncel, *Mater. Lett.*, Vol. 18 (1994) 286.

11. W. O. Soboyejo, S. L. Semiatin, B. Majundar and V. Seetharaman, in *Processing and Fabrication of Advanced Materials for High Temperature Applications-II*, (edited by V. A. Ravi and T. S. Srivatsan), TMS, Warrendale, PA, 1993, p. 169.

12. Y. W. Kim and D. M. Dimiduk, *JOM*, Vol. 43 (1991) 40.

13. Y. W. Kim, *Acta Metall. Mater.*, Vol. 40 (1992) 1121.

14. K. S. Chan, *JOM*, Vol. 44 (1992) 30.

15. H. Deve and A. G. Evans, *Acta Metall. Mater.*, Vol. 39 (1991) 1171.

16. H. Deve, A. G. Evans and D. S. Shih, *Acta Metall. Mater.*, Vol. 40 (1992) 1259.

17. K. T. V. Rao, G. R. Odette and R. O. Ritchie, *Acta Metall. Mater.*, Vol. 40 (1992) 353.

18. C. M. McCullogh, J. J. Valencia, C. G. Levi and R. Mehrabian, *Acta Metall. Mater.*, Vol. 37 (1989) 1321.

19. J. D. Bryant and S. L. Semiatin, *Scripta Metall. Mater.*, Vol. 25 (1991) 449.

20. S. L. Semiatin, D. C. Vollmer, S. M. El-Soundani and C. Su, *Scripta Metall. Mater.*, Vol. 24 (1990) 1409.

21. R. Vetter, L. Z. Zhuang, I. Majewska-Glabus and J. Duszezyk, *Scripta Metall. Mater.*, Vol. 24 (1990) 2025.

22. J. Zhang, R. J. Perez and E. J. Lavernia, *Acta Metall. Mater.*, Vol. 42 (1994) 395.

23. X. Liang and E. J. Lavernia, *Metall. Trans.*, Vol. 25A (1994) 2341.

24. D. G. Morris and M. A. Morris, *J. Mater. Res.*, Vol. 6 (1991) 361.

25. X. Liang, H. K. Kim, J. C. Earthman and E. J. Lavernia, *Mater. Sci. Eng.*, Vol. 153A (1992) 646.

26. X. Liang, J. C. Earthman and E. J. Lavernia, *Acta Metall.*, Vol. 40 (1992) 3003.

27. X. Liang and E. J. Lavernia, *Mater. Sci. Eng.*, Vol. 161A (1993) 221.

28. Y. Wu, J. Zhang and E. J. Lavernia, *Metall. Trans.*, Vol. 25B (1994) 135.

29. A. R. E. Singer, *Mater. Sci. Eng.*, Vol. 135A (1991) 13.

30. M. Gupta, F. A. Mohamed and E. J. Lavernia, *Metall. Trans.*, Vol. 23A (1992) 831.

31. T. S. Srivatsan, T. S. Sudarshan and E. J. Lavernia, *Prog. Mater. Sci.*, Vol. 39 (1995) 317.

32. D. G. Morris, M. A. Morris, S. Gunter, M. Leboeuf and G. Hollrigl, *Scripta Metall. Mater.*, Vol. 27 (1992) 1645.

33. J. M. Young, G. Itoh, M. H. Jacobs and T. P. Johnson, "Centrifugal Spray Deposition of Titanium Aluminide" in *Powder Metallurgy in Aerospace, Defense and Demanding Applications*, (edited by F. H. Froes), MPIF, 1993.

34. J. W. Sears, "Titanium Spray Formed Structures" in *1992 Powder Metallurgy World Congress*, (edited by J. M. Capus and R. M. German), MPIF/APMI, 1992, p. 281.

35. J. W. Sears, G. Itoh and M. H. Loretto, "Spray Forming of Ti-Aluminide-Based Alloys" in *Titanium '92: Science and Technology*, (edited by F. H. Froes and I. L. Caplan), TMS, 1993.

36. S. C. Huang, *Metall. Trans.*, Vol. 23A (1992) 375.

37. D. I. Kimm and J. Wolfenstine, *Scripta Metall. Mater.*, Vol. 30 (1994) 615.

38. M. F. Bartholomeusz, Q. Yang and J. A. Wert, *Scripta Metall. Mater.*, Vol. 29 (1993) 389.

39. S. C. Cheng, J. Wolfenstine and O. D. Sherby, *Metall. Trans.*, Vol. 23A (1992) 1509.

40. M. F. Ashby and B. F. Dyson, "Creep Damage Mechanics and Micromechanisms" in *Proceeding of the 6th International Conference on Fracture*, (edited by S. R. Valluri, D. M. R. Taplin, P. R. Rao and J. F. Knott), Pergamon, Oxford, UK, 1984, p. 3.

41. K. J. Hemker, M. J. Mills and W. D. Nix, *Acta Metall. Mater.*, Vol. 39 (1991) 1901.

42. J. H. Schneibel and J. A. Horton, *J. Mater. Res.*, Vol. 3 (1988) 651.

43. M. Es-Souni, A. Bartels and R. Wagner, *Mater. Sci. Eng.*, Vol. 171A (1993) 127.

44. J. Cadek, *Creep in Metallic Materials* (Elsevier, Armsterdam, 1988).

45. A. K. Mukherjee, J. Bird and J. E. Dorn, *Trans. ASM*, Vol. 62 (1969) 155.

46. O. D. Sherby and P. M. Burke, *Prog. Mater. Sci.*, Vol. 13 (1967) 325.

47. S. Kroll, H. Mehrer, N. Stolwijk, C. Herzig, R. Rosenkranz and G. Frommeyer, *Z. Metallk.*, Vol. 83 (1992) 591.

48. R. W. Hayes and P. A. McQuay, *Scripta Metall. Mater.*, Vol. 30 (1994) 259.

49. B. D. Worth, J. W. Jones and J. E. Allison, *Metall. Mater. Trans.*, Vol. 26A (1995) 2947.

50. M. Es-Souni, A. Bartels and R. Wagner, *Mater. Sci. Eng.*, Vol. 192/193A (1995) 698.

51. J. Wolfenstine, G. Gonzalez-Doncel and O. D. Sherby, *J. Mater. Res.*, Vol. 5 (1990) 1359.

52. B. D. Worth, J. W. Jones and J. E. Allison, *Metall. Mater. Trans.*, Vol. 26A (1995) 2961.

53. G. Hug, A. Loiseau and A. Lasalmonie, *Phil. Mag.*, Vol. 54A (1986) 47.

54. S. I. Hong and C. Laird, *Acta Metall. Mater.*, Vol. 38 (1990) 1581.

55. J. H. Hausselt and W. D. Nix, *Acta Metall.*, Vol. 25 (1977) 1491.

56. R. W. Lund and W. D. Nix, *Metall. Trans.*, Vol. 6A (1975) 1329.

57. G. F. Hancock and B. R. McDonnell, *Phys. Stat. Sol.*, Vol. 4A (1971) 143.

58. K. Maruyama, T. Takahashi and H. Oikawa, *Mater. Sci. Eng.*, Vol. 153A (1992) 433.

59. H. Oikawa, *Mater. Sci. Eng.*, Vol. 153A (1992) 427.

60. R. W. Hayes and B. London, *Acta Metall. Mater.*, Vol. 40 (1992) 2167.

61. A. Chakraborty and J. C. Earthman, *Metall. Mater. Trans. A*, in press (1997)

62. P. M. Anderson and J. R. Rice, *Acta Metall.*, Vol. 33 (1985) 409.

63. S. Ho and A. Saigal, *Mater. Sci. Eng.*, Vol. 183A (1994) 39.

64. S. Ho and A. Saigal, *Acta Metall.*, Vol. 42 (1994) 3253.

65. C. A. Bigelow, *J. Compos. Technol. Res.*, Vol. 15 (1993) 304.

66. A. Levy and J. M. Papazian, *Proc. 12th Riso Int. Sym. on Materials Science*, (1991) p. 475.

67. S. Ho and E. J. Lavernia, *Appl. Comp. Mater.*, Vol. 2 (1995) 1.

68. N. Shi and R. J. Arsenault, *J. Comp. Technol. Res.*, Vol. 13 (1991) 211.

69. T. Nakamura and S. Suresh, *Acta Metall.*, Vol. 41 (1993) 1665.

70. S. Ho, Ph.D. Dissertation, Tufts University, 1994.

71. M. D. Snyder and K. J. Bathe, *Nucl. Eng. Des.*, Vol. 64 (1981) 49.

72. ABAQUS Users' Manual (Hibbitt, Karlsson and Sorensen, Inc., 1995).

73. ABAQUS Theory Manual (Hibbitt, Karlsson and Sorensen, Inc., 1995).

74. W. F. Smith, *Principles of Materials Science and Engineering* (McGraw-Hill, Inc., New York, 1990).

75. Y. W. Kim, *JOM*, Vol. 41 (1989) 24.

76. G. Conzales-Doncel and J. Wolfenstine, *Scripta Metall.*, Vol. 28 (1993) 885.

77. H. A. Lipsitt, D. Shechtman and R. E. Schafrik, *Metall. Trans.*, Vol. 6A (1975) 1991.

78. T. Kawabata, T. Kanai and O. Izumi, *Acta Metall.*, Vol. 33 (1985) 1355.

79. M. Nazmy and M. Staubli, *Scipta Metall.*, Vol. 31 (1994) 829.

80. R. E. Schafrik, *Metall. Trans.*, Vol. 8A (1977) 1003.

81. S. Yamauchi and H. Shiraishi, *Mater. Sci. Eng.*, Vol. 152A (1992) 283.

82. X. Liang and E. J. Lavernia, *Scripta Metall.*, Vol. 29 (1993) 353.

83. X. Liang, Ph.D. Dissertation, University of California, Irvine, 1994.

84. P. Mathur, D. Apelian and A. Lawley, *Acta Metall.*, Vol. 37 (1989) 429.

85. S. C. Huang, *Titanium Aluminum Alloys Modified by Chromium and Niobium and Method of Preparation*, U.S. Patent Number 4,879,092, (Nov. 7, 1989).

86. B. P. Bewlay and B. Cantor, *Metall. Trans.*, Vol. 21B (1990) 899.

87. P. S. Grant and B. Cantor, *Cast Metals*, Vol. 4 (1991) 140.

88. P. S. Grant, B. Cantor and L. Katgerman, *Acta Metall. Mater.*, Vol. 41 (1993) 3097.

89. H. Liu, R. H. Rangel and E. J. Lavernia, *Mater. Sci. Eng.*, Vol. 191A (1995) 171.

90. J. Szekely, *Fluid Flow Phenomena in Metalls Processing* (Academic Press, New York, 1979), p. 261.

91. H. Kurten, J. Raasch and H. Rumpf, *Chemie-Ingenieur-Technik*, Vol. 38 (1966) 941.

92. E. M. Gutierrez, E. J. Lavernia, G. M. Trapaga, J. Szekely and N. J. Grant, *Metall. Trans.*, Vol. 20A (1989) 71.

93. R. E. Bolz and G. L. Tuve, *Handbook of Tables for Apllied Engineering Science* (CRC Press, Cleveland, Ohio, 1973), p. 56.

94. C. G. Levi and R. Mehrabian, *Metall. Trans*, Vol. 13A (1982) 221.

95. J. P. Hirth, *Metall. Trans.*, Vol. 9A (1978) 401.

96. D. Turnbull, *J. Chem. Phys.*, Vol. 20 (1952) 411.

97. D. Turnbull, in *Undercooled Alloy Phases*, (edited by E. W. Collings and C. C. Koch), AIME-TMS, Warrendale, PA, 1987, p. 3.

98. D. Turnbull and R. E. Cech, *J. Appl. Phys.*, Vol. 21 (1950) 804.

99. J. H. Perepezko and D. H. Rasmussen, *Met. Trans.*, Vol. 9A (1978) 1490.

100. J. J. Valencia, C. McCullough, C. G. Levi and R. Mehrabian, *Acta Metall.*, Vol. 37 (1989) 2517.

101. W. E. Ranz and Marshall, *Chem. Eng. Prog.*, Vol. 48 (1952) 141.

102. F. P. Incropera and D. P. Dewitt, *Introduction to Heat Transfer* (John Wiley & Sons, New York, 1985), p. 179.

103. R. Willnecker, D. M. Herlach and B. Fenerbacher, *Appl. Phys. Lett.*, Vol. 49 (1986) 1339.

104. E. Scheil, *Zeitschrift fur Metallkunde*, Vol. 34 (1942) 70.

105. H. D. Brody and M. C. Fleming, *Trans. Metall. Soc. AIME*, Vol. 236 (1966) 615.

106. T. F. Bower, H. D. Brody and M. C. Flemings, *Trans. Metall. Soc. AIME*, Vol. 236 (1966) 624.

107. T. W. Clyne and W. Kurz, *Metall. Trans.*, Vol. 12A (1981) 965.

108. J. H. Moll, C. F. Yolton and B. J. McTiernan, *Int. J. Powder Metall.*, Vol. 26 (1990) 149.

109. E.A. Brandes, *Smithells Metals Reference Book*, 6th ed., Butterworths, London, (1983.)

110. D. P. Woodruff, *The Solid-Liquid Interface* (Cambridge University Press, 1973), p. 70.

111. V. G. McDonell, E. J. Lavernia and G. S. Samuelsen, "Simultaneous Measurement of Metal Atomizer Particle Size and Velocity Using Phase Doppler Interferometry" in *Synthesis and Analysis in Materials Processing: Advances in Characterization and Diagnostics of Ceramics and Metal Particulate Processing*, (edited by E. J. Lavernia, H. Henein and I. Anderson), The Minerals, Metals &Materials Society, 1989, p. 13.

112. J. M. Marinkovich, F. A. Mohamed, J. R. Pickens and E. J. Lavernia, *JOM*, Vol. 41 (1989) 36.

113. J. Zhang, M. N. Gungor and E. J. Lavernia, *J. Mater. Sci.*, Vol. 28 (1993) 1515.

114. B. Li, W. Cai and E. J. Lavernia, *J. Mater. Synth. Proc.*, Vol. 4 (1996) 35.

115. E. J. Lavernia, *Int. J. Rapid Solidif.*, Vol. 5 (1989) 47.

116. B. Engelmann and J. O. Hallquist, *NIKE2D User Manual* (Lawrence Livermore National Laboratory, 1991).

117. B. K. Kad, M. Dao and R. J. Asaro, *Phil. Mag.*, Vol. 71A (1995) 567.

118. M. Dao, B. K. Kad and R. J. Asaro, *Phil. Mag.*, Vol. 74A (1996) 569.

119. H. Matthies and G. Strang, *Int. J. Num. Meth. Eng.*, Vol. 14 (1979) 1613.

120. A. Needleman and J. R. Rice, *Acta Metall*, Vol. 28 (1980) 1315.

121. B. Budiansky, J. W. Hutchinson and S. Slutsky, in *Mechanics of Solids: The Rodney Hill 60th Anniversary Volume*, (edited by H. G. Hopkins and M. J. Sewell), Pergamon Press, Oxford, 1982, p. 13.

122. V. Tvergaard, *J. Mech. & Phys. of Solids*, Vol. 32 (1984) 373.

123. J. R. Rice, *Acta Metall.*, Vol. 29 (1981) 675.

124. E. v. d. Giessen and V. Tvergaard, *Mech. Mater.*, Vol. 17 (1994) 47.

125. J. O. Hallquist, G. L. Goudreau and D. J. Benson, *Comp. Meth. App. Mech. and Eng.*, Vol. 51 (1985) 107.

126. G. Hug, A. Loiseau and P. Veyssiere, *Phil. Mag.*, Vol. 57A (1988) 499.

127. H. K. Kim, J. Wolfenstine and J. C. Earthman, *Scripta Metall. Mater.*, Vol. 27 (1992) 1067.

128. B. K. Kad, P. M. Hazzledine and H. L. Fraser, *High Temperature Ordered Intermetallic Alloys V*, (1993) p. 495.

129. S. Mitao, S. Tsuyama and K. Minakawa, in *Microstructure/Property Relationships in Titanium Aluminides and Alloys*, (edited by Y. W. Kim and R. R. Boyer), TMS., Warrendale, 1991, p. 297.

130. D. S. Shih, S. C. Huang, G. K. Scarr, H. Jang and J. C. Chestnut, in *Microstructure/Property Relationships in Titanium Aluminides and Alloys*, (edited by Y. W. Kim and R. R. Boyer), TMS., Warrendale, 1991, p. 135.

131. H. Riedel, *Fracture at High Temperatures* (Springer-Verlag, 1986).

132. W.-Y. Chu and A. W. Thompson, *Metall. & Mater. Trans.*, Vol. 23A (1992) 1299.

133. W. O. Soboyejo and R. J. Lederich, in *Structural Intermetallics*, (edited by R. D. e. al.), TMS., Warrendale, 1993, p. 353.

134. H. Mehrer, *Mater. Trans., JIM*, Vol. 37 (1996) 1259.

APPENDIX 1. INTERACTIONS/TRANSITIONS

A1.1. Participation at Meetings

A1.1.1. Presentations

1. "Spray Processing and Mechanical Behavior of γ-TiAl", B. Li and E.J. Lavernia, to be presented at **the Second International Symposium on Structural Intermetallics**, September 21-26, 1997, Champion, Pennsylvania.

2. "Numerical Simulations of Grain Boundary Cavitation", A. Chakraborty and J.C. Earthman, to be presented at **the Seventh International Conference of Creep and Fracture in Engineering Materials and Structures**, August 10-15, 1997, Irvine, California.

3. "Investigation on the Creep Behavior of Spray Formed γ-TiAl Alloys" B. Li and E.J. Lavernia, presented on **the 4th International Conference on High Temperature Intermetallics**, April 27-May 1, 1997, San Diego, California.

4. "Spray forming of TiB_2 Reinforced gamma Titanium Aluminide alloys" B. Li and E.J. Lavernia, presented on **the 126th TMS Annual Meeting: Symposium on Advances in Synthesis and Processing of Metal and Ceramic Matrix Composites**, February 9-13, 1997, Orlando, Florida.

5. "Spray Atomization and Deposition of gamma Titanium Aluminide Alloys" co-authored by B. Li and E.J. Lavernia, presented on **the 126th TMS Annual Meeting: Symposium on Spray Forming — Experiment, Analysis and Applications**, February 9-13, 1997, Orlando, Florida.

6. "Finite Element Analysis of Grain Boundary Cavitation in Fully Lamellar Titanium Aluminide Intermetallic Alloy", A. Chakraborty and J.C. Earthman, presented at **the 126th TMS Annual Meeting: Symposium on Fundamentals of Gamma Titanium Aluminides**, February 9-13, 1997, Orlando, Florida.

7. "Investigation of Thermal Residual Stresses in Layered 2024Al/SiC Composite using Finite Element Method and X-Ray Diffraction" S. Ho and E.J. Lavernia, presented at **the TMS/ASM International Symposium on Processing and Fabrication of Advanced Materials**, October 7-10, 1996, Cincinnati, Ohio.

8. "Characterization of Low-Cycle Fatigue Damage on Inconel 718 by Laser Light Scattering," K. J. C. Chou and J. C. Earthman, presented at **the ASM/TMS Materials Week: Nondestructive Evaluation and Material Properties Symposium**, October 7-10, 1996, Cincinnati, Ohio.

9. "Spray Forming of Gamma Titanium Aluminide Alloys", B. Li and E.J. Lavernia, presented on **the 3rd International Conference on Spray Forming**, September 9-11, 1996, Cardiff, Wales, UK.

10. "Finite Element Models of High Temperature Deformation Mechanisms in Equiaxed and Fully Lamellar TiAl Alloy Microstructures," A. Chakraborty and J. C. Earthman, presented at **the ASME Mechanics and Materials Conference: Deformation Mechanisms in Structural Materials Symposium,** June 14, 1996, Baltimore, Maryland.

11. "Two Dimensional Profile of Momentum and Thermal Behavior of Spray Atomized γ-TiAl Droplets", B. Li, X. Liang, J.C. Earthman and E.J. Lavernia, presented at **the 4th International Conference on Powder Metallurgy in Aerospace, Defense and Demanding Applications**, May 8-10, 1995, Anaheim, California.

12. "Characterization of Low-Cycle Fatigue Damage on Inconel 718 by Laser Light Scattering", K. J. C. Chou and J. C. Earthman, presented at **the 124th TMS Annual Meeting: High Temperature Materials Characterization Symposium**, Feb. 12-16, 1995, Las Vegas, Nevada.

13. "Microstructure and Fracture Behavior of a Spray Atomized and Deposited Nickel Aluminide Intermetallic", D. Lawrynowicz, X. Liang, T.S. Srivatsan and E.J. Lavernia, presented at **the Second International**

Symposium on Fatigue and Fracture of Ordered Intermetallic Materials, October 2-6, 1994, Rosemont, Illinois.

14. "Analysis of a Dendritic Ni_3Al Alloy by X-Ray Diffraction", K. J. C. Chou and J. C. Earthman, presented at **the International Conference on High-Temperature Intermetallics**, May 16-19, 1994, San Diego, California.

A1.1.2. Posters

1. "Finite Element Analysis of Primary Creep in Fully Lamellar γ TiAl Intermetallics", A. Chakraborty and J.C. Earthman, postered at **the MRS Spring Meeting**, April 8-12, 1996, San Francisco, California.

A1.2. Consultative/Advisory Functions

1.   Interactions with **Dr. Lee Semiatin** (Wright Laboratories, WL/MLLN Wright Patterson AFB, OHIO 45433). During the AFOSR funded period, we actively exchanged results, including both processing details as well as compressive creep data obtained in our AFOSR funded research program with Dr. Semiatin. Dr. Semiatin's comments on our data were very useful in the interpretation of the results obtained in the present AFOSR program.

2.   Interactions with **Dr. Don Larsen** (Howmet Corporation, Operhall Research Center, 1500 South Warner Street, Whitehall, MI 49461-1895). Dr. Larsen has been actively working with cast γ-TiAl for a number of years. Presently, the Howmet Corporation is actively working with a variety of compositions for elevated temperature aerospace applications. Moreover, the Howmet Corporation is actively developing spray forming technology as a manufacturing approach for the spraying of superalloy rings. Since the pilot plant spray facility that is available at Howmet is not designed for the spraying of Ti, Dr. Larsen expressed a strong interest in our AFOSR funded program. During the AFOSR funded period, we successfully spray formed one of the titanium aluminide compositions provided by Howmet Corporation. The spray formed titanium aluminide was then sent to Howmet for characterization.

3.   Interactions with **Dr. Shyh-Chin Huang** (General Electric Research and Development Center, Building K-1, Room MB 275, P.O. Box 8, Schenectady, NY 12301). Dr. Huang has extensive experiences in the study of γ-TiAl alloys. He has been well known for the development of Ti-48Al-2Nb-2Cr alloys. Our interactions with Dr. Huang included successful spray forming of Ti-42Al-2Nb-2Cr alloys supplied by General Electric Research and Development Center, characterization of spray formed Ti-42Al-2Nb-2Cr in General Electric, and exchange of the preliminary results.

APPENDIX 2. HONORS AND AWARDS

1. Professor E.J. Lavernia

AWARDS RECEIVED

Dates	Award
1996	Silver Medal of the Materials Science Division of ASM International
1995	Best Paper Award, with X. Liang and J. Wolfenstine, Journal of Thermal Spray Technology
1995	Alexander Von Humboldt Fellowship from Germany
1993	Fellowship from the Iketani Science and Technology Foundation, Tokyo, Japan
1993	ASM International 1993 Bradley Stoughton Award for Young Teachers
1993	Elected to Who's Who in Science and Engineering
1992	Elected to National Honorary Society of Alpha Kappa chapter of Phi Delta Beta
1992	Elected to 2000 Notable American Men
1991	Elected to American Men and Women of Science
1991	Elected to Who's Who in the West
1990-1993	Young Investigator Award, Office of Naval Research (ONR)
1990-1992	Aluminum Company of America (ALCOA) Fellowship
1989-1994	Presidential Young Investigator, National Science Foundation (NSF)
1989-1990	Outstanding Assistant Professor, School of Engineering, UCI
1989	Faculty Career Development Award, University of California, Irvine
1982-1984	Rockwell International Fellowship
1982	George H. Main 1945 Fund Award, Brown University
1978	Alfred J. Loepsinger Scholarship, Brown University

MEMBERSHIPS IN BOARDS OF REVIEW
AND ADVISORY ROLES

Dates	Description
1996	Advisory Board *Key Engineering Materials*, Trans. Tech
1996	Board of Review *International Journal of Non-Equilibrium Processing*
1996 May 21-24	Member of NSF's Panel on Materials Research Science and Engineering Centers
1996 April 15-17	Member of NSF's Panel on Materials Research Science and Engineering Centers
1996	Co-Editor *Journal of Materials Synthesis and Processing*
1996	ASM International Chair of *Bradley Stoughton Award Committee*
1995	Member of NASA's Headquarters Review Panel on Microgravity in Materials Science
1994-1996	ASM International *Bradley Stoughton Award Committee*
1994	Advisory Board, *Advanced Composites Newsletter*
1994	Board of Review *Journal of Applied Composite Materials*
1994	Board of Review *Metallurgical and Materials Transactions*
1993, 1994	National Research Council's Review Board on NSF Graduate Fellowships Program
1993	Advisor for the Composites Committee *Journal of Metals*
1993	Invited Scientist, technical exchange, The Korea-U.S. *Joint Symposium on Advanced Materials*
1992	National Science Foundation's *Manufacturing Initiative*

2. Professor J. C. Earthman

AWARDS RECEIVED

Date	Award
1996	Elected to Dictionary of International Biography
1996	Elected to Who's Who in the West
1994	Elected to Who's Who in Science and Engineering
1992	Elected to Who's Who in American Education
1992	Augmentation Award for Science and Engineering Research Training, Air Force Office of Scientific Research
1980	Rice Engineering Alumni Scholar in Materials Science, Rice University.

MEMBERSHIPS IN BOARDS OF REVIEW AND ADVISORY ROLES

Date	Description
1997	Chair of the Organizing Committee, Seventh International Conference on Creep and Fracture of Engineering Materials and Structures, Irvine, CA, August 10-16
1996	Chair of the Flow and Fracture Committee of the Structural Materials Division of ASM International
1995	Board of Review *Metallurgical and Materials Transactions*
1995	Member of the Board of Directors, Newport Coast Oral-Facial Institute

APPENDIX 3. PERSONNEL

SENIOR RESEARCH PERSONNEL:

E.J. Lavernia, Professor
J.C. Earthman, Associate Professor

GRADUATE STUDENTS:

B. Li, Ph. D Candidate
A. Chakraborty, Ph. D. Candidate

STAFF:

I. Sauer, Research Technician